UNIVERSITÀ DEGLI STUDI DI ROMA TOR VERGATA

MACROAREA DI SCIENZE MATEMATICHE, FISICHE E NATURALI

MASTER'S DEGREE IN PHYSICS

Curriculum in Astrophysics and Space Science

Investigating the Physical Properties of the Powerful Accretion Disk Wind in the Active Galaxy IRAS 13224−3809 with XMM−Newton

Supervisor
Prof. Francesco Tombesi

Candidate
Matricola: 0325648
Sreeparna Ganguly

Co-Supervisor
Prof. Luka Č. Popović

Collaborators
Dr. Marco Laurenti
Mr. Pierpaolo Condò

Academic Year 2023/2024

MASTER IN ASTROPHYSICS AND SPACE SCIENCE

Erasmus Mundus Master
in Astrophysics and Space Science

Master Thesis

Investigating the Physical Properties of the Powerful Accretion Disk Wind in the Active Galaxy IRAS 13224−3809 with XMM−Newton

Supervisors

Prof. Francesco Tombesi
Physics Dept., Tor Vergata University of Rome

Prof. Luka Č. Popović
Mathematics Dept., University of Belgrade

Collaborators

Dr. Marco Laurenti, Mr. Pierpaolo Condò
Physics Dept., Tor Vergata University of Rome

Author

Sreeparna Ganguly
Matricola: 0325648

Academic Year 2023/2024

Funded by the European Union

This Master thesis is submitted in partial fulfillment of the requirements for the degree FISICA - Curriculum Erasmus Mundus as part of a multiple degree awarded in the framework of the Erasmus Mundus Joint Master in Astrophysics and Space Science −− MASS jointly delivered by a Consortium of four Universities: Tor Vergata University of Rome, University of Belgrade, University of Bremen, and Université Cote d'Azur, regulated by the MASS Consortium Agreement and funded by the EU under the call ERASMUS-EDU-2021-PEX-EMJM-MOB.

To the experiences that shaped our journey,
and the unforeseen paths that led us to new horizons,
To friends and family who brightened the way.

Contents

Abstract

Among the most energetic sources in the Universe are the Active Galactic Nuclei (AGNs) which are powered by accretion onto the supermassive black holes (SMBHs) present at the center of almost every galaxy. One of the most fundamental feature of SMBHs is the presence of winds launched off their accretion disks. Black hole winds are high-velocity outflows made of gas and energy that emerge from the vicinity of black holes located at the center of the galaxies. The most extreme of these winds, called ultra-fast outflows (UFOs), are observed in X-rays and are believed to originate in the innermost regions of the accretion disk. These powerful winds play a crucial role in various astrophysical processes and are thought to have significant implications for the evolution of galaxies and the regulation of the growth of supermassive black holes. But there has yet been no conclusive picture of the physical properties of such winds from the observations obtained so far. X-ray and multi-wavelength observations are providing significant breakthroughs and insights in connecting physical scales ranging from the event horizon up to the galaxy's outskirts.

We perform a time-averaged X-ray spectral analysis of IRAS 13224-3809 by using XMM-Newton observations of 2016 using XSPEC. This is a low-redshift (z = 0.0658) Narrow Line Seyfert 1 (NLS1) galaxy and is one of the most variable AGNs in the X-ray band, with its magnitude in flux changing by a factor of 10 in 500 seconds in the energy range 0.3 to 10 keV. It is characterized by having a relatively low-mass, high accretion rate SMBH. X-ray spectral signatures of a highly ionized ultra-fast outflow driven at near relativistic speeds by the accretion flow has already been detected from this source.

Previous authors modeled the broad-band continuum (E = 0.3 - 10.5 keV) using a

physically motivated relativistic reflection model to take into account the reflection of the X-ray corona light from the accretion disk of the black hole. The presence of wind is almost always associated to absorption, but emission from the plasma can also be present and should be taken into account. To this end, we want to check if and how wind emission can contribute to the spectrum above 2 keV, without any prior on relativistic reflection. Our objective is to model these emission components using WINE table models in XSPEC. Wind in Ionized Nuclear Environment (WINE) is a photoionization code that allows the user to self-consistently calculate absorption and emission profiles for accretion disk winds. This will provide us with better constraints on the geometry and other physical properties of the wind.

Our analysis shows that we need to consider two layers of the wind or outflow to model the data. Each layer of the wind has a LOS velocity of the order of 20-30% the speed of light and the LOS inclination of ~ 50 degrees. The outflow energetics indicate it to be fairly significant with powerful feedback effects. The high power of the wind also suggests a possible magnetohydrodynamic (MHD) driving or at least a contribution of magnetic fields to radiative driving.

Chapter 1

Introduction to AGN

The term "active galactic nucleus" (AGN) refers to the extremely bright and energetic phenomena occurring in the central regions of galaxies that cannot be directly linked to stars. A galaxy hosting an AGN is called an active galaxy. AGNs are believed to be powered by accretion of infalling matter onto the supermassive black hole (SMBH) present at the center of the host galaxy. They are amongst the most energetic sources observed in universe, radiation from an AGN can outshine the entire host galaxy. Accretion is by far the most efficient energy conversion process, and actually represents one of the main channels for SMBHs to grow during the galaxy lifetime. As such, AGNs can be used as a means of discovering distant objects. They are also significant features in the study of galactic evolution and high-energy astrophysics. The observed characteristics of an AGN depend on mass of the central black hole (BH), the rate of gas accretion, the orientation of the accretion disk, the degree of obscuration of the nucleus by dust, and presence or absence of jets. The radiative output of AGN spans the entire electromagnetic spectrum, from the radio up to the gamma-ray band. All of them share some core characteristics: extremely high luminosity, small emitting regions in all bands, as suggested by the extreme observed variability, highly broadened and blueshifted absorption and emission features.

There are two main accretion mechanisms: radial accretion, in which matter radially flows onto the compact object, and disk accretion where matter spirals around

the mass before being engulfed. The simplest configuration is an approximately spherically symmetric accretion flow onto the BH referred to as Bondi accretion (Bondi (1952)). But this is an idealistic scenario because the efficiency of the conversion of gravitational potential energy into radiation is low. It is important to note that accretion onto a compact object can be limited by the effects of the radiation pressure experienced by the infalling plasma. This limit, first pointed out by Eddington in the 1920s, depends on the mass of the compact object and the mean opacity of the infalling material. Radiation pressure on the infalling gas can stop spherical accretion if the radiated luminosity reaches the Eddington Limit. This happens when the radial force due to radiation counterbalances the gravitational force. Eddington luminosity is given by:

$$L_{Edd} = \frac{4\pi G M m_p c}{\sigma_T} \approx 1.3 \times 10^{38} \frac{M}{M_\odot} ergs^{-1} \approx 1.3 \times 10^{46} \frac{M}{10^8 M_\odot} ergs^{-1} \tag{1.1}$$

where $\sigma_T \approx 6.65 \times 10^{-25}$ cm^2 is the Thomson cross-section, $M_\odot \approx 1.99 \times 10^{33}$ g is the solar mass, and $M_8 \equiv M/10^8 M_\odot$ is the typical mass of SMBHs in AGN. One can define the Eddington ratio in terms of the AGN bolometric luminosity L_{bol} and the Eddington luminosity L_{Edd} as:

$$\lambda_{Edd} = \frac{L_{bol}}{L_{Edd}} \tag{1.2}$$

The Eddington limit is reached when $\lambda_{Edd} = 1$. The mass accretion rate $\dot{M}$ can be estimated if we know the radiative efficiency η of the conversion of gravitational energy into luminosity from the following formula:

$$L = \eta \dot{M} c^2 \rightarrow \dot{M} = \frac{L}{\eta c^2} \tag{1.3}$$

Similarly,

$$\dot{M}_{Edd} = \frac{L_{Edd}}{\eta c^2} \tag{1.4}$$

where $\dot{M}_{Edd}$ is the Eddington accretion rate. The Eddington ratio can also be written

in terms of the accretion rate as:

$$\lambda_{Edd} = \frac{\dot{M}_{bol}}{\dot{M}_{Edd}} \tag{1.5}$$

where $\dot{M}_{bol}$ is the bolometric accretion rate.

1.1 Classification of AGN

AGNs emit across the entire electromagnetic spectrum, leading to their classification at different wavelengths as new parts of the spectrum were investigated with advancement of technology. This has resulted in a complex and sometimes confusing classification system. The most important criteria as suggested by Tadhunter (2008) are (Fig. 1.1):

- the presence or absence of broad emission lines in optical spectra (e.g. Sy1[1]/Sy2, BLRG/NLRG),
- optical morphology (e.g. Sy1/radio-loud quasar, BLRG/radio-loud quasar),
- radio morphology (FRI/FRII),
- variability (BL Lac, OVV),
- luminosity (e.g. Sy1/radio-quiet quasar, WLRG[2]/NLRG),
- spectral shape (e.g. SSRLQ, FSRLQ).

Each classification method highlights different aspects of AGN, contributing to a nuanced understanding of these powerful cosmic objects.

1.1.1 Seyfert Galaxies

Carl K. Seyfert identified a subset of galaxies with exceptionally bright nuclei that produce broad emission lines from atoms in various ionization states, their nuclei

[1]The explanation of the acronyms are described later in the text.

[2]Following the definition of Tadhunter et al. (1998), Weak line radio galaxy (WLRG) are objects with EW[OIII] $< 10\mathring{A}$. They are sometimes labelled as low excitation galaxies (LEGs).

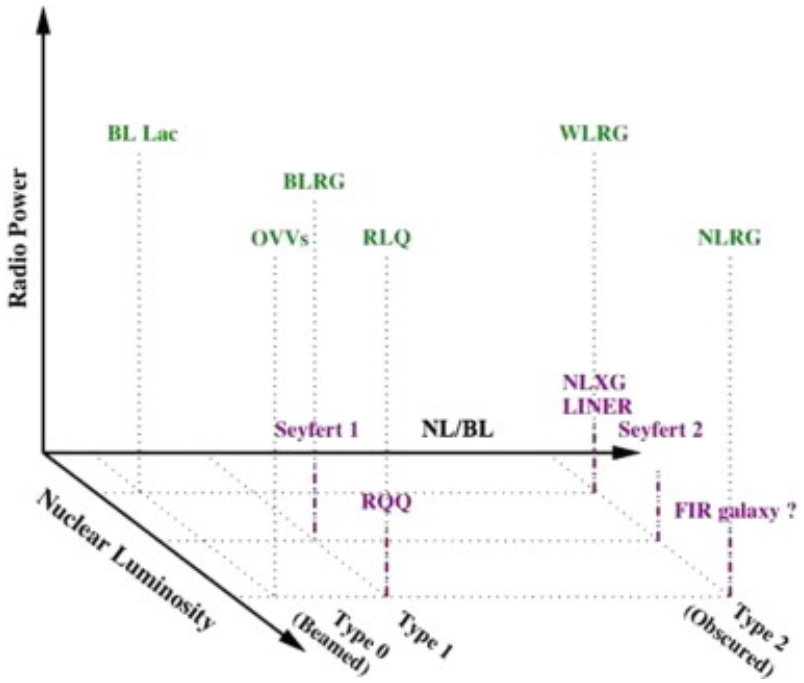

Figure 1.1: 3D classification for AGN, reflecting the major divisions amongst the various classes of AGN: the presence or absence of broad permitted lines, AGN luminosity, and radio loudness. Taken from Tadhunter (2008)

appearing almost stellar-like. These galaxies are now called Seyfert (Sy) galaxies. These galaxies are the most common class of AGNs in the local Universe ($z < 0.1$). Seyfert galaxies have typical luminosities of $L_{AGN} \sim 10^{42-44}$ erg/s, which is comparable to that of an entire galaxy. Because of their close proximity to us, we get the best spectra and images for them, allowing us to study in detail the physical processes at work. Their definition as a class originates from optical spectroscopy and Khachikian and Weedman (1974) categorized them into two types based on their relative widths of narrow (forbidden) and Balmer lines.

Optical Classification

Seyfert 1 (Sy1) galaxies (Fig. 1.2a,c) exhibit very broad emission lines that include both allowed Balmer lines (H I, He I, He II) and narrower forbidden lines (e.g., [O III], [O II], [N II], [Ne III], [Ne IV]). So both the narrow line region (NLR) and broad line region (BLR) are observed. The broadening of these lines, attributed to Doppler effects, suggests that the emitting sources are dense matter ($n_e > 10^9$ cm^{-3}) moving at speeds of 1000 to 5000 km/s for allowed lines (BLR) and low-density gas with

electron densities of $n_e \sim 10^3 - 10^6$ cm^{-3} moving around 500 km/s for forbidden lines (NLR). Seyfert 2 (Sy2) galaxies (Fig. 1.2b,c) have only narrow lines (both permitted and forbidden), with characteristic speeds of about 500 km/s. So, mostly, if not only, the NLR is observed. Some spectra display both broad and narrow permitted lines. They are classified as intermediate and borderline objects. These objects are sorted into the subclasses Sy1.2, Sy1.5, Sy1.8, and Sy1.9, according to their Balmer line characteristics, following the scheme introduced by Osterbrock (1977).

X-Ray Classification

Sy1 galaxies are the ones that emit the most X-ray energy which is highly variable and can change appreciably on timescales ranging from days to hours. On the other hand, X-rays are less frequently measured for Sy2 galaxies. This distinction among Seyferts in the X-ray band is based on the intrinsic absorption measurement in the soft X-rays (E $\leq$ 2 keV). The absorption is measured as the equivalent column density of hydrogen, N_H, along the line of sight. A neutral hydrogen column density of $N_H = 10^{22}$ cm^{-2} is typically used as a dividing line between type 1s and type 2s in the X-rays. Most Seyfert galaxies that have an intrinsic X- ray absorption of $N_H < 10^{22}$ cm^{-2} are spectroscopically classified in the optical as Seyfert 1 or 1.2. Conversely, most Seyfert galaxies with $N_H > 10^{22}$ cm^{-2} in the X-rays are optically classified as Seyfert 1.8, 1.9 or 2. Some objects exhibit variations in the intrinsic absorption of X-rays over time, leading to different classifications for the particular source depending on the observation. These sources, known as "changing look" AGNs (CL-AGNs) (Matt et al. (2003); LaMassa et al. (2014)), can transition from one type to another. The cause of this transition can be due to changes in the accretion disk, which impact the presence or absence of BLR lines. Some spectra may also display a mix of broad and narrow permitted lines.

Narrow-Line Seyfert 1 galaxies

Narrow-Line Seyfert 1s (NLSy1s) are a subset of the Seyfert 1 galaxies. They are strong X-ray emitters, having broad Hα lines but narrow Hβ lines (FWHM $<$ 2000 km/s), similar to a Seyfert 1.9 (Osterbrock and Pogge (1985)). NLSy1s have the

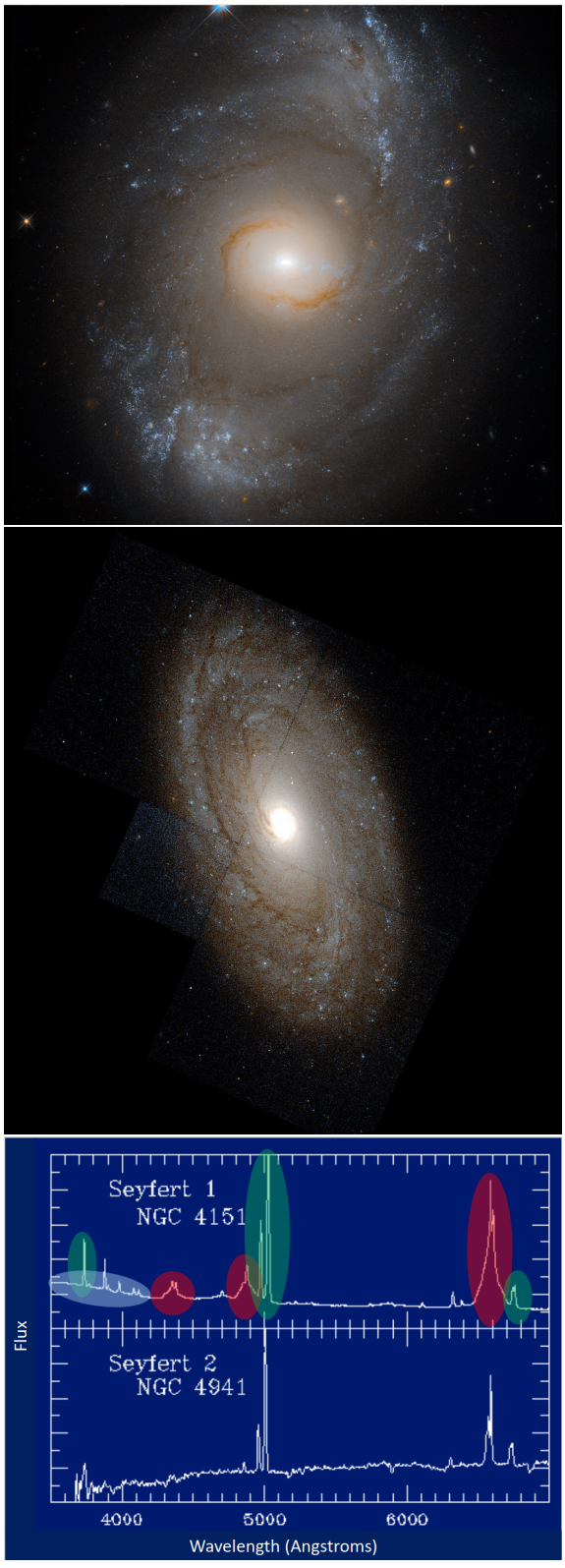

Figure 1.2: a) NGC 4151, a Sy1 galaxy, by HST (WFC3). b) NGC 4941, a Sy2 galaxy, by the Hubble Space Telescope. c) Spectra showing the difference between Sy1 and Sy2 (Courtesy: Bill Keel).

following properties:

- relatively small SMBH masses, $M_{BH}^{NLSy1} \sim 10^5 - 10^7 M_{\odot}$ than other Seyferts but comparable bolometric luminosities,
- often high accretion rates, closer to the Eddington limit (Collin and Kawagachi (2004)) and powerful disk winds,
- FWHM(Hβ) $<$ 2000 km/s,
- $[OIII]/H\beta_{tot} < 3$,
- FeII/H$\beta_{tot} > 0.5$,
- strong soft-X-ray emission,
- strong and rapid X-ray variability due to non-thermal beamed emission,
- weak optical/UV variability due to stable accretion disk,
- sometimes it can be radio-loud,
- some cases show clear radio jets (on $\sim$1-100 pc scales),
- sometimes detected as gamma-ray sources.

Optical studies using the Hubble Space Telescope suggest that the SMBHs in NLSy1s are still growing via secular processes (gas accretion) instead of mergers (Mathur et al. (2012)). Some of the peculiar properties of NLSy1s can be partially explained because of the low inclination with respect to the observer, i.e., by a near face-on view of the AGN (Peterson (2011)). Recently, some NLSy1s have even been detected in the gamma-rays by the Fermi satellite. This association with gamma-ray sources suggests that some NLSy1s might contain a misaligned jet, leading to strong non-thermal emission in the radio and gamma-rays (Foschini (2011)).

1.1.2 Radio Galaxies

A radio galaxy (RG) is a type of galaxy with massive radio-emitting regions that extend far beyond its visible structure. The powerful radio lobes are fueled by jets from its active galactic nucleus which is often hidden. They have large radio luminosities reaching up to 10^{39} W at radio wavelengths between 10 MHz and 100 GHz. The radio emissions are caused by the synchrotron process and their structure is determined by the interaction between twin jets and the surrounding medium, modified by relativistic beaming. Most radio galaxies are large elliptical galaxies. In the scheme developed by Fanaroff and Riley (1974), these RGs are classified based on their radio morphology into two subgroups (Fig. 1.3): the low-luminosity Faranoff-Riley class I (FR-I) galaxies, which have a compact emission arising from close to the core (edge darkened). The high-luminosity FR-II objects have structures dominated by the radio lobes and most of the emission appears to come from the far end of the extended emission (edge brightened). The dividing line between the two classes is given by the luminosity of $L_R = 10^{32}$ erg $s^{-1}Hz^{-1}sr^{-1}$ at 175 MHz. The physical origin of the FRI vs. FRII dichotomy is still debated. One possibility can be that jets in FRIs are not as collimated and/or powerful as in FRIIs.

The AGN cores in radio galaxies have some similarities with the cores of Seyfert galaxies. Similar to Seyfert galaxies, they can also be categorized into two main types: broad-line radio galaxies (BLRGs), which are analogous to Seyfert 1 galaxies, and narrow-line radio galaxies (NLRGs), corresponding to Seyfert 2 galaxies. BLRGs constitute of a bright, star-like nuclei surrounded by faint, hazy envelopes. In contrast, NLRGs are usually giant or supergiant elliptical galaxies, such as types cD, D, and E. Despite these similarities, Seyfert nuclei are relatively subdued in radio wavelengths compared to the more intense radio emissions of radio galaxies. Additionally, almost all Seyfert galaxies are spiral galaxies, whereas strong radio galaxies are not spirals.

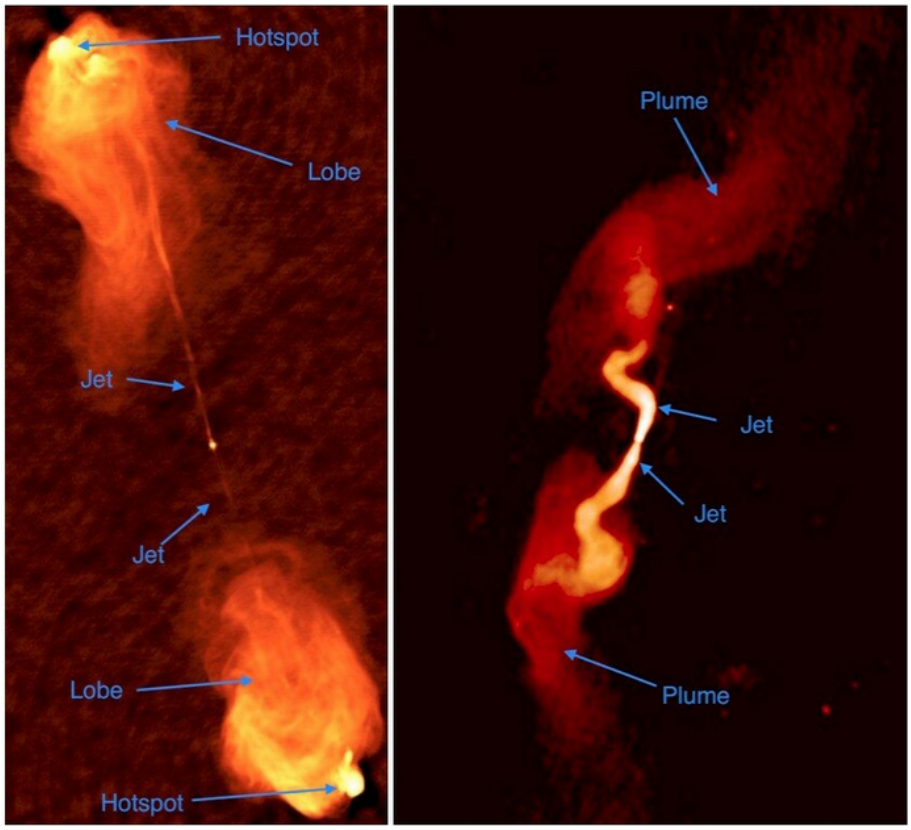

Figure 1.3: Powerful FR II radio jets in CygnusA (left) and the weak FRI jets in 3C 31 (right) from the VLA (Very Large Array) radio maps. Image credit: NRAO/AUI.

1.1.3 Quasars

While performing optical observations of the sources found from the large surveys of the sky using radio telescopes, a large number of radio galaxies and supernova remnants were discovered. However, many of the sources could not be easily identified as they appeared like blue stars in optical images. These sources were therefore called Quasi-Stellar Objects, or Quasars (QSOs). Optical spectroscopy revealed strong emission lines from one such source (3C 273), which were later realized to be Balmer lines but redshifted by 16% (Schmidt 1963). Therefore, the source was identified as extragalactic at very large redshift of z = 0.158 with an enormous luminosity. With the discovery of more number of quasars at large redshifts, researchers realized that these sources are the more distant equivalents of nearby Seyfert galaxies. An arbitrary dividing line was introduced to separate Seyferts and quasars; Seyfert galaxies with absolute magnitudes brighter than $M_B < 23$ mag are referred to as quasars (Schmidt and Green (1983)). QSOs have luminosities of $L_{AGN} > 10^{44}$ erg/s and can reach up to $\sim 10^{47}$ erg/s. QSOs can be further classified into radio-loud (RL) and radio-quiet (RQ) quasars (Fig. 1.4). Almost 90% of all quasars are RQ-QSOs and do not produce a powerful jet. By using the redshift-corrected monochromatic flux values at 5 GHz (radio) and 2500 $\mathring{A}$ (optical/UV), it is possible to set an observational boundary between them:

$$R^* \equiv \frac{f_{5GHz}}{f_{2500\mathring{A}}}$$

If $R^* > 10$, then it is RL-QSO and if $0.1 < R^* < 1$ then it is a RQ-QSO. Radio-loud quasars have high luminosity, a strong radio emission, and distinct spectroscopic features compared to radio-quiet objects. Their host galaxies tend to be more massive than those of radio-quiet AGNs (Dunlop et al. (2003)). The radio-loud quasars are also sub-divided on the basis of whether they are steep radio spectrum dominated (steep spectrum radio loud quasars: SSRLQ) or flat radio spectrum dominated (FSRLQ). The former is dominated by the radio lobe emission of the host galaxy. The latter have a compact radio structure and they are often referred

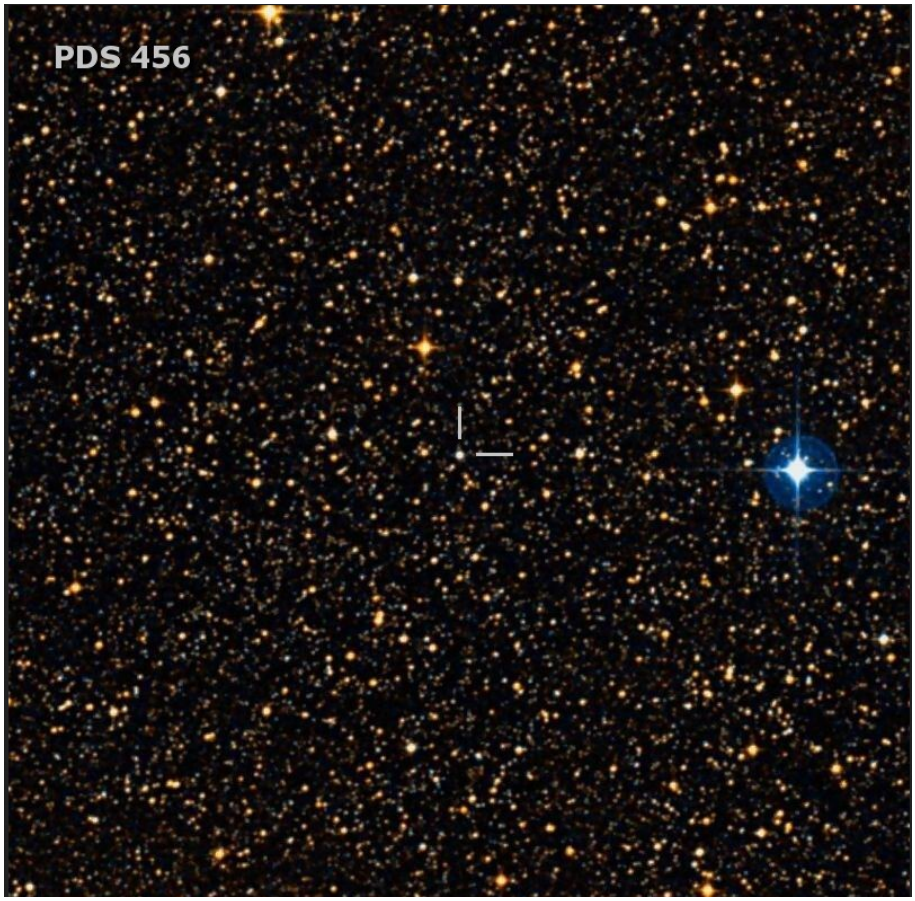

Figure 1.4: PDS 456 is a bright radio-quiet quasar in the south-western part of the constellation Serpens Cauda. Image Credit: DSS2

to as blazars. Another type of quasar, known as Broad Absorption Line Quasars (BAL QSOs), are radio quiet and X-ray weak. Their absorbtion lines are broad and blueshifted. They are associated with powerful quasar winds and represent ∼15-20% of radio-quiet QSOs.

1.1.4 Other Classes

Blazars

Blazars are a special subclass of quasars with rapid variability and high linear polarization at visible wavelengths. These sources are radio-loud quasars with a relativistic jet pointing directly at the observer, or very close to the observer's line of sight. They are prominent emitters from the radio frequencies up to Very High Energies (VHE) above 1 TeV. They are classified into BL Lac objects and Flat Spectrum Radio Quasars (FSRQs). BL Lac objects do not have prominent features in the optical spectrum, they are continuum dominated and almost featureless. FSRQs, on the other hand, show broad emission lines, but the lines can disappear if the continuum from the jet is too high.

Low-Luminosity AGNs (LL-AGNs)

According to Greene and Ho (2007), the central SMBHs in AGNs undergo accretion only for 1% of the time and spend 99% of their existence in a quiescent state. A quiescent AGN has a bolometric luminosity of less than $\sim 10^{37}$ erg/s, whereas AGNs with luminosities around $\sim 10^{40}$ erg/s do exist. A class of objects which seems to fill in this luminosity gap are the Low-Ionization Nuclear Emission-Line Regions (LINERs). LINERs have faint core luminosities and strong emission lines originating from lowly ionized gas. Their properties are very similar to Seyfert 2 galaxies, but with stronger forbidden lines. LINERs mark the low-luminosity end of the AGN phenomenon, accreting with low radiative efficiency (see Fig. 1.5). Because of their low luminosity, the X-ray spectra of LINERs are dominated by starburst emission from the host galaxy, rather than by the AGN core. They have more number of highly absorbed Compton-thick sources among them compared to

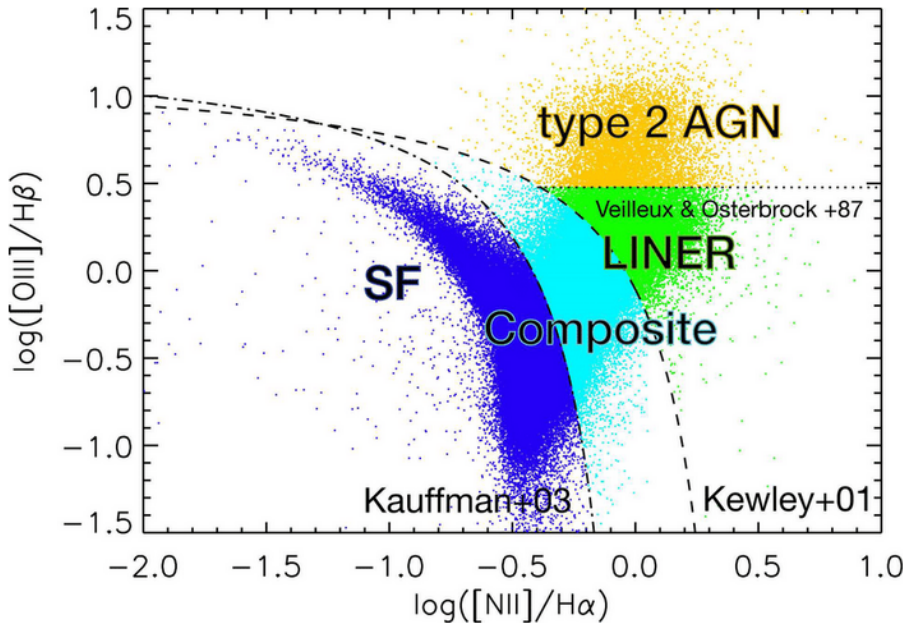

Figure 1.5: LINERs spectra can be distinguished from those of Seyfert 2s and HII regions by a diagnostic diagram which uses two line ratios, such as the one in the figure using [NII]/Hα vs. [OIII]/Hβ. The dashed-dotted line is the criterion given by Kauffmann et al. (2003), the dashed line is the criterion given by Kewley et al. (2001), and the dotted line is the traditional scheme (Veilleux & Osterbrock 1987). Taken from Toba et al. (2014).

Seyferts, so absorption plays a major role in them.

Ultraluminous Infrared Galaxies (ULIRGs)

Galaxies usually emit infrared (IR) radiation because of their stellar population and dust component. But there are a fraction of galaxies observed in IR that exceed the expected infrared emission significantly. These IR bright sources are called Luminous Infrared Galaxies (LIRGs) and are defined by a far IR luminosity exceeding $L_{IR} > 10^{11} L_{\odot}$. There is also a population of galaxies with $L_{IR} > 10^{12} L_{\odot}$ called Ultra-Luminous Infrared Galaxies (ULIRGs). Among the ULIRGs, 95% of the sources are galaxy mergers (Sanders and Mirabel (1996)). In the case of ULIRGs, an important contribution to the dust heating is from the AGN at the center of the galaxy. They are more prominent at higher cosmological redshifts (Goto et al. 2011).

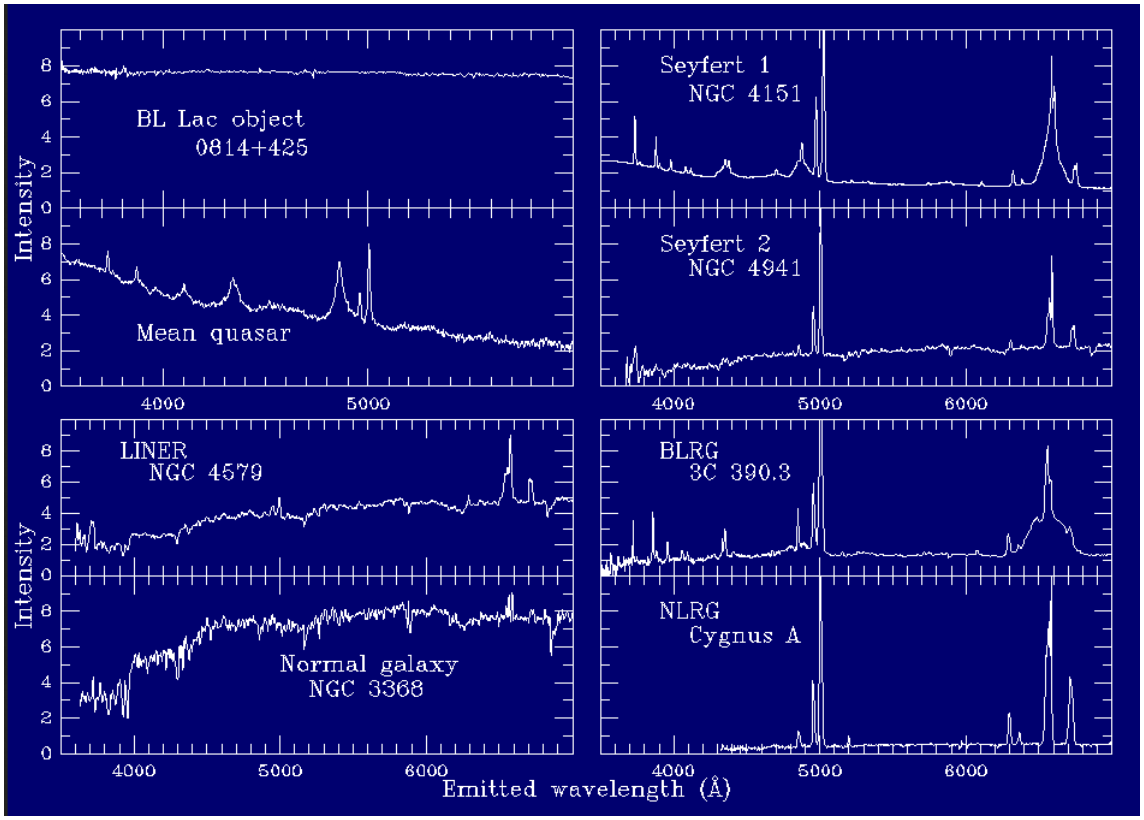

Figure 1.6: Optical spectra of various kinds of active galactic nuclei. Each active galaxy behaves peculiarly and in the bottom left panel the typical emission of a quiescent galaxy is reported. Taken from Peterson (1997).

Galaxy type	Active nuclei	Emission lines		X-rays	Excess of		Strong radio	Jets	Variable	Radio loud
		Narrow	Broad		UV	Far-IR				
Normal (non-AGN)	no	weak	no	weak	no	no	no	no	no	no
LINER	unknown	weak	weak	weak	no	no	no	no	no	no
Seyfert I	yes	yes	yes	some	some	yes	few	no	yes	no
Seyfert II	yes	yes	no	some	some	yes	few	no	yes	no
Quasar	yes	yes	yes	some	yes	yes	some	some	yes	some
Blazar	yes	no	some	yes	yes	no	yes	yes	yes	yes
BL Lac	yes	no	no/faint	yes	yes	no	yes	yes	yes	yes
OVV	yes	no	stronger than BL Lac	yes	yes	no	yes	yes	yes	yes
Radio galaxy	yes	some	some	some	some	yes	yes	yes	yes	yes

Figure 1.7: Features of different types of galaxies. Source: Wikipedia.

1.2 Unification of AGN

While classification of AGNs is concerned with recognizing the diversity in their properties, some of the key insights into the nature of AGN have been gained by considering what they have in common rather than how they differ. A fundamental question in AGN research is whether the various appearances of the AGN phenomenon can be explained by a unified model or if the different classes are intrinsically distinct. Unification theory propose that different observational classes of AGN are a single type of physical object observed under different conditions.

At the 1978 BL Lac conference, Blandford & Rees proposed the beaming unification model, suggesting that AGNs appear as blazars when their emission is beamed along the symmetry axis of AGN toward the observer. However, this model could not account for radio-quiet AGNs due to absence of powerful radio jets in them. This lead to the consideration of orientation and obscuration effects as the two key factors in explaining the different subclasses of an AGN.

According to the most simplified picture (Fig. 1.8), AGNs are of two types - radio-quiet and radio-loud. A range of luminosities is observed for each type, leading to the Faranoff-Riley classes as well as the distinction between Seyferts and quasars. All other differences would be explained by orientation effects. A comprehensive review of AGN unification was provided by Antonucci (1993) and Urry and Padovani (1995). According to them, the existence of an optically thick torus surrounding the central AGN would lead to the absence of broad emission lines in the case of Seyfert 2s, if they were observed edge-on, as their broad line region (BLR) would be hidden, compared to Seyfert 1 objects, which are mostly observed close to face-on. As the narrow line region (NLR) lies further away from the central SMBH, it would still be observable when the BLR is obscured by the torus. Below is a detailed discussion on the main components of an AGN. The AGN winds and outflows have been discussed in greater detail in Chapter 2.

1.2.1 Central Engine

The core of an active galaxy is powered by a supermassive black hole at its center. A SMBH is a very massive body with mass ranging from approximately $10^6 - 10^{10} M_\odot$. Yet, it is so small and compact that even electromagnetic radiation, such as visible light, cannot escape from it. Because of this combination of relatively small size and very strong gravitational field emitted while in its accretion phase, it acts as a key component of the central engine that powers an AGN. Indeed, the energy generated by the accretion process onto this black hole is the only mechanism capable of producing the observed output power. It efficiently converts the potential and kinetic energy to radiation which explains the persistent Eddington luminosities. However, since black holes themselves do not emit any radiation, they do not directly contribute to the observed spectrum of the active galactic nucleus. What we can observe is the activity just outside the event horizon where the gravitational field is not strong enough to prevent the escape of electromagnetic radiation. The radius of the event horizon is called the Schwarzschild radius (R_S). It is the distance at

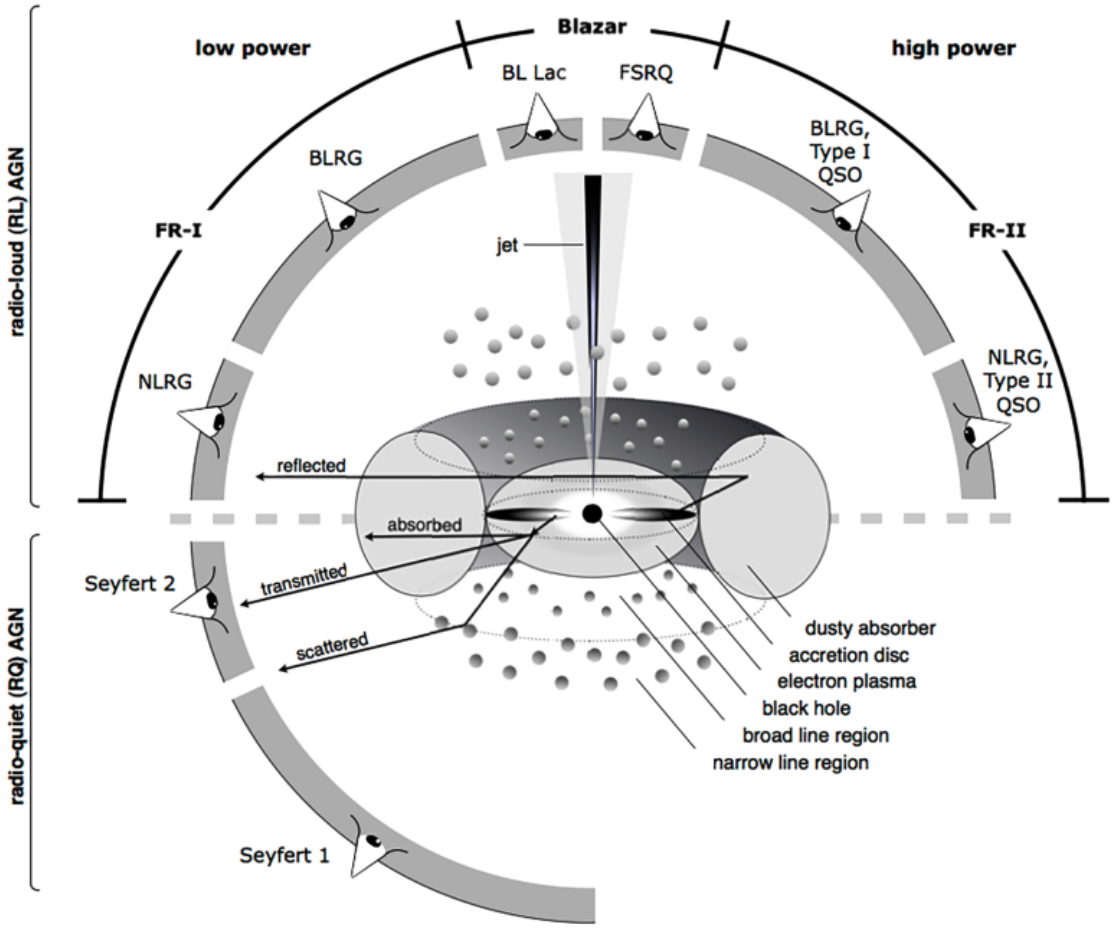

Figure 1.8: Conceptual view of an Active Galactic Nucleus. Bottom and top panel refer to radio- quiet and radio-loud objects, respectively. Different components and sight lines are indicated. Taken from Beckmann and Shrader (2012).

which the escape speed is just equal to the speed of light and is given by

$$R_S = \frac{2GM_{BH}}{c^2} \tag{1.6}$$

The sphere of influence is a region around the SMBH in which the gravitational potential of the black hole dominates over the gravitational potential of the host galaxy. It is expressed as:

$$R_{inf} = \frac{GM_{BH}}{\sigma^2} \tag{1.7}$$

where M_{BH} is the mass of the SMBH and σ is the velocity dispersion of stars in the host galaxy bulge.

The black holes can be described by using three parameters: mass M, angular momentum J, and electric charge Q. All other information on the matter and radiation that falls through the event horizon is lost for an external observer. This is called the "no-hair theorem" for black holes. The total net charge of a BH is expected to be zero because it is discharged on the surrounding plasma. Depending on the angular momentum, we go from Schwarschild (non-rotating, spherical symmetric horizon) up to Kerr (maximally spinning) black holes.

1.2.2 Accretion Disk

Matter spiraling inwards onto a black hole with a non-zero angular momentum settle into a flattened structure called an accretion disk. Due to the dissipative processes taking place in the accretion disk, matter is transported inwards and angular momentum outwards, causing the accretion disk to heat up. The total angular momentum of the system is conserved. The radiation from the accretion disk excites cold atomic material close to the black hole and this in turn radiates particular emission lines. The structure of the accretion disk is mainly determined by the ratio $\lambda_{Edd} = \dot{M}/\dot{M}_{Edd}$. The three main accretion disk regimes are (Fig. 1.9):

- At very low accretion rates, $\lambda_{Edd} << 1$, the disk becomes optically thin

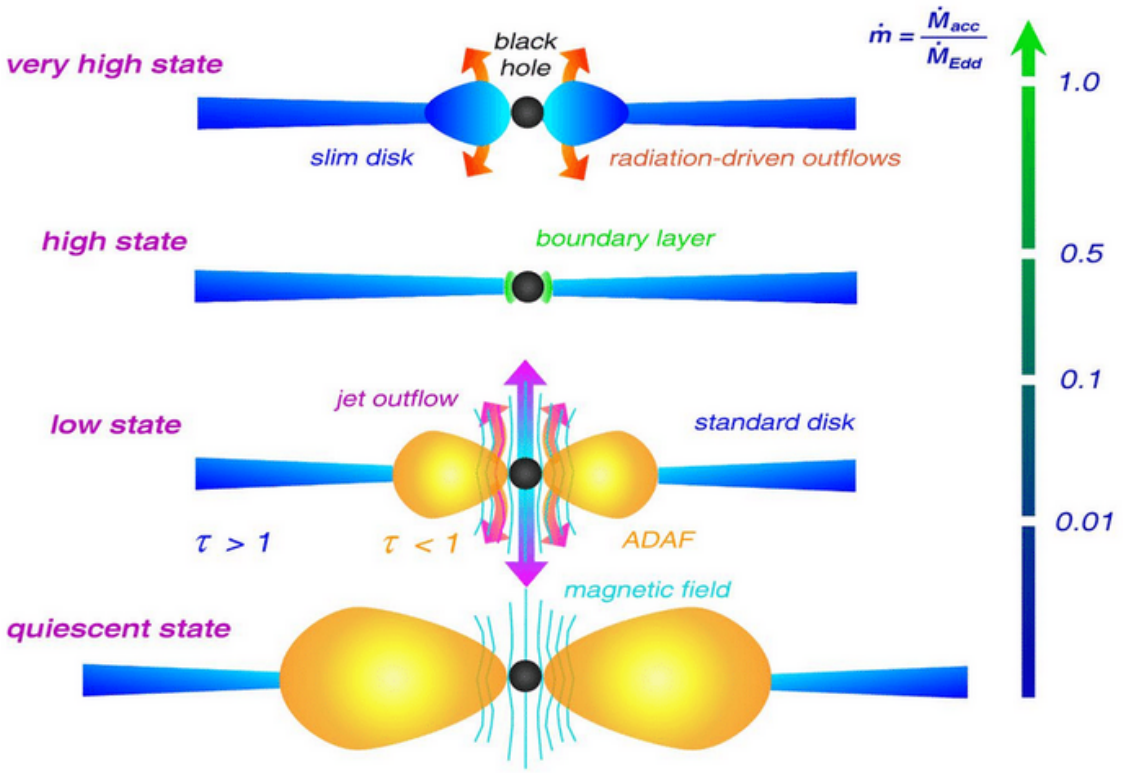

Figure 1.9: The schematic figure of the state of a black hole accretion disk (Müller (2004)). The label on the left of each model indicates the X-ray state.

($\tau << 1$). The inner regions can not cool efficiently. The energy is mainly advected inwards and the radiative efficiency is very low ($\eta << 1$), forming an Advection Dominated Accretion Flow (ADAF) (Narayan and Yi (1994)). Electrons and ions decouple, forming a two-temperature structure (ion torus), with ions reaching temperatures of T$\sim 10^{12}$ K. The ionized torus keeps a strong anchored magnetic field which is able to collimate an outflow of charged particles along rotation axis (e.g., jets and outflows/winds).

- At medium accretion rates, $\lambda_{Edd} < 1$, and high opacities ($\tau > 1$), the accretion disk is thin and the disk radiates efficiently ($\eta = 0.1$). The rate at which energy is transported inwards is negligible as compared to the rate at which energy is radiated vertically outwards. The emitted spectrum comprises of optically thick thermal spectra over the range of temperatures through the disk. This type of accretion disk is called standard disk, α-disk or Shakura & Sunyaev disk (Shakura and Sunyaev (1973)).

- At high accretion rates rates, $\lambda_{Edd} >> 1$, and high opacities ($\tau >> 1$), the radiation is partially trapped by the accreting material and the disk expands vertically into a "radiation torus" or geometrically thick disk, which radiates inefficiently approximately as $\lambda_{Edd}^{-1} << 1$. The spectrum is approximately given by a black-body at a single temperature T$\sim 10^4$ K. Such disks are known as super-Eddington or slim disks (Abramowicz et al. (1988); Ohsuga et al. (2009).

1.2.3 X-ray Corona

The central supermassive black hole is surrounded by a hot corona which is a region of relativistic electrons responsible for generating X-ray emissions via inverse Compton scattering of optical and UV photons from the accretion disk (Haardt and Maraschi (1991), Haardt and Maraschi (1993), Maraschi and Haardt (1997)). The two-phase model proposes that the optically thick "cool" accretion disk emits soft photons, which are then up-scattered by an optically thin cloud of hot electrons in the corona.

The corona is thought to form from the acceleration and confinement of energetic particles by magnetic fields anchored in the accretion disk (Galeev et al. (1979); Merloni and Fabian (2001)). Its geometry is still debated. It can be complex — either patchy or collimated — and extend over part of the inner disk (Wilkins and Fabian (2012)). It is often treated as a point-like source above the black hole's spin axis for modelling (the lamppost geometry Miniutti and Fabian (2004)). The actual shape of the corona is more likely to be extended or outflowing (Wilkins et al. (2016)), rather than being a point source. The first polarimetric results exclude a compact 'spherical' lamppost geometry for the corona, suggesting instead a slab-like geometry, possibly a wedge (Gianolli et al. (2023)).

1.2.4 Dusty Torus

AGN unification models propose a dusty toroidal structure that surrounds the central accretion disk, obscuring the view of the central AGN and the broad line region depending on the observer's angle. In Type 1 AGNs, the observer has a clear view of the inner AGN and broad line region, while in Type 2 AGNs, this view is obstructed by the torus, which absorbs much of the optical-UV emission. The torus is expected to be located within the sphere of influence of the SMBH, i.e., at r $<$ 1 parsec. From the statistics of Seyfert 1 and 2 galaxies, the torus height and radius are in the ratio H/R $\sim$ 1 (Schmitt et al. (2001)). Recent studies favor a clumpy torus structure rather than a uniform toroid (Elitzur and Shlosman (2006)). For a clumpy torus the distinction between Type 1 and 2 is due to orientation as well as the probability of the observer having direct view of the AGN nucleus through the clouds. The origin of the torus is not yet clearly understood. Some of the proposed theories to explain its formation are:

- the clouds may be due to matter coming off the relatively cool, outer regions, of the accretion disk,
- matter accreted from the ambient material within the host galaxy,
- outflowing clouds from the disk embedded in a disk wind.

The torus structure is dependent on luminosity. It is expected that the distance of the torus is larger in more luminous AGN, because dust will reach the sublimation temperature already at relatively larger distances. The dust sublimation radius is given as:

$$r = 1.3 L_{UV46}^{1/2} T_{1500}^{-2.8} pc \tag{1.8}$$

1.2.5 Broad and Narrow Line Regions

One of the earliest striking characteristics of AGN in the optical/UV spectrum is the presence of redshifted, time-varying emission lines with Doppler widths ranging from 1000 to 10000 km/s. The most prominent among these are the hydrogen Balmer series (Hα, Hβ, Hγ), Lyα, and lines like Mg II, C III, and C IV. The "broad-line

region" (BLR) was so named because of the broader lines originating closer to the BH. In contrast, the narrower and less variable lines originate from more distant regions, hence the name "narrow-line region" (NLR).

The large Doppler widths of the BLR ($\sigma \sim 10000$ km/s) is a strong indication that they reside deep inside the gravitational potential well of the SMBH ($R_{BLR} \sim 1 - 100$ light days), as largely demonstrated by reverberation mapping studies. Thus, the BLR provides important insights into the central engine and a method to estimate the SMBH mass. The suppression of forbidden lines indicates an electron density of $n_e > 10^9$ cm^{-3}. The volume of BLR is almost empty, with a filling factor of $10^{-6} - 10^{-7}$. The mass of BLR is not more than a few solar mass. The BLR is not spherically symmetric, it is likely to include disk and wind components.

In contrast, the narrow lines, originating farther away, have Doppler widths of around 500 km/s, indicating a more rarefied environment. Its variability suggests a size of $R_{NLR} \gtrsim 100$ pc. The presence of both forbidden and permitted lines indicates a low density $n_e \sim 10^3 - 10^4$ cm^{-3}. The mass of the NLR is a million times that of solar mass. The NLR dynamics can provide information on the way the AGN connects to the host galaxy. Observations suggest that the NLR may be an extended AGN outflow and/or it is influenced by the AGN jet in radio-loud sources.

1.2.6 Relativistic Jets

The jets are thought to be extremely energetic and highly collimated outflows of charged particles, originating from the innermost regions of the central SMBH. They are an important feature in certain subclasses of AGN. These structures, far exceeding the size of the active nucleus, are commonly observed in radio-loud AGN and are the dominant component of emission in blazars. They can extend upto hundreds of kpcs or Mpcs into the space while maintaining their collimation. Their apparent velocities can even be "superluminal", i.e., reaching up to 40 times the speed of

light. Distortion of magnetic fields within the innermost accretion flow are thought to collimate and acclerate these jets. The jets emit synchrotron radiation across optical, IR, and radio bands, while blazars produce intense γ-ray emissions. When the jet ram pressure matches with that of the interstellar medium, shock fronts form, creating radio lobes with bright hot spots.

The composition of AGN jets is still under debate. Several blazar studies show possible correlation between X-ray and TeV γ-ray flares, favoring leptonic jet models that efficiently accelerate relativistic electrons (Mastichiadis and Kirk (1997)). But models involving hadronic (e.g., protons) jets are not ruled out completely (Mücke and Protheroe (2001)). The current agreement is that the AGN jets are likely composed of a mixture of proton and lepton plasmas. The protons would comprise most of the kinetic energy, while the electrons would be responsible for the entire emission we observe (Sikora et al. (2009)).

1.3 The AGN Spectral Energy Distribution

AGNs emit powerful radiation throughout the entire electromagnetic (EM) spectrum. The Spectral Energy Distribution (SED) of an AGN provides a comprehensive view of the AGN's emitted radiation across different wavelengths. This wide wavelength coverage allows us to reflect on the physics of various processes occurring in the AGN, including accretion onto the SMBH, emission from the surrounding accretion disk, and interactions with the surrounding medium. The typical AGN SED is shown in Fig. 1.10. Each spectral component arises from a particular region of the AGN structure. Here is a breakdown of the components typically observed in an AGN SED:

1.3.1 Radio Emission

The compact and extended components in AGNs emit synchrotron radiation which falls in the radio band of the EM spectrum. It can be recognized in the SED by its smooth, broad-band character and strong polarization. The extended emission

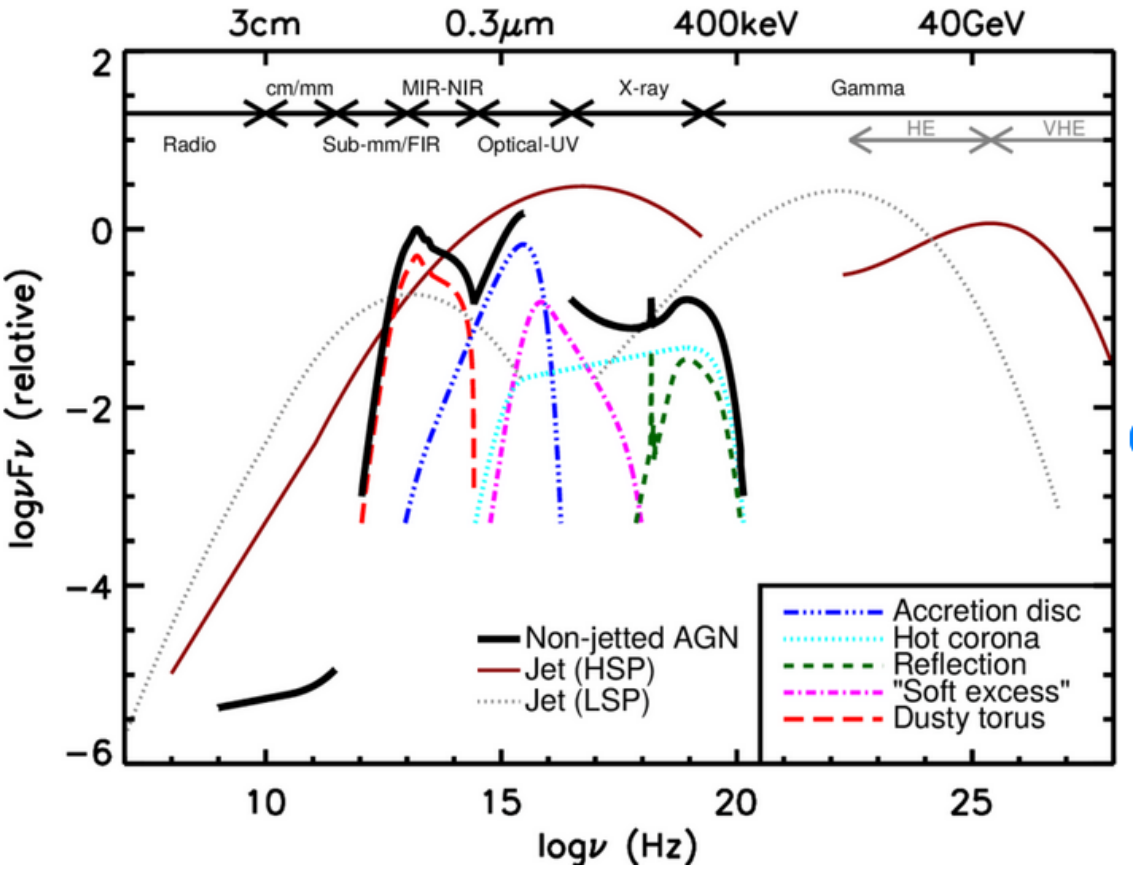

Figure 1.10: A schematic representation of an AGN spectral energy distribution (SED). The black solid curve represents the total emission and the various coloured curves (shifted down for clarity) represent the individual components. The intrinsic shape of the SED in the mm-far infrared (FIR) regime is uncertain; however, it is widely believed to have a minimal contribution (to an overall galaxy SED) compared to star formation (SF), except in the most intrinsically luminous quasars and powerful jetted AGN. The primary emission from the AGN accretion disk peaks in the UV region. The jet SED is also shown for a high synchrotron peaked blazar (HSP, based on the SED of Mrk 421) and a low synchrotron peaked blazar (LSP, based on the SED of 3C 454.3). Taken from Harrison et al. (2014). Image credit: C. M. Harrison.

arises from jets, particularly the jet lobes or hot spots formed by jet-environment interactions. The compact core emission, unresolved at less than arcsecond scales, is believed to be near the central SMBH where the jets become optically thin. The synchrotron nature of the radio emission indicates the presence of relativistic electrons (Lorentz factor of $\gamma \sim 10^4$) within the radio emitting plasma in a magnetic field environment. The electrons follow a power-law energy distribution as $n(E)dE = kE^{-p}dE$. The emission can be parametrized as $S_\nu \propto \nu^{-\alpha}$ where $\alpha = (p-1)/2$ is the spectral index of the corresponding synchrotron radiation spectrum.

1.3.2 IR Emission

A significant portion of the bolometric output of AGN originates from the infrared band, covering approximately 2.5 decades in the frequency range $10^{12} - 10^{14.5}$ Hz. However, only a small part of the IR spectrum is accessible from the ground due to atmospheric limitations, even with some windows available. The majority of IR observations are conducted using space-based observatories.

The IR emission is composed of mainly three spectral components:

- Thermal radiation from the dusty torus near the AGN.
- Thermal dust continuum associated with star formation or starburst activity in the host galaxy. This consist of line emissions from macro-molecules known as polycyclic aromatic hydrocarbons (PAHs) as well as continuum features from the heated dust.
- Other line emissions emerging from molecular, atomic, and ionic species in the AGN or host galaxy environments.

The IR spectral shape is characterized by a minimum at $\sim$ 1µm, a bump with the peak at $\sim$ 20µm and a steep power-law like decline at $\sim$ 100µm. The dusty torus absorbs and reprocesses the UV continuum from the AGN and radiates it in IR. It is assumed that we do not have an ideal blackbody, and the emitting matter has

only one temperature (i.e., isotermal). We can then write the emitted luminosity as (Soldi et al. (2008)):

$$L_\nu = 4\pi A_{Dust} B_\nu(T)(1 - e^{-\tau_\nu})$$

where A_{Dust} is the area of a projected surface seen by the observer, $B_\nu(T)$ is the Planck function of a blackbody of temperature T and τ_ν is the optical depth. We can approximate the frequency-dependent optical depth by a power-law in the form:

$$\tau_\nu = \left(\frac{\nu}{\nu_0}\right)^\beta$$

1.3.3 Optical/UV Emission

In AGNs where the nuclear continuum emission is directly visible, the optical band dominates, having an approximate power-law dependence with wavelength. Another important feature is the presence of broad optical emission lines, believed to originate from material close to the central SMBH in the BLR. These lines appear broadened due to the Doppler effect, as the emitting material is in gravitationally bound orbits around the SMBH.

The UV band is also very important because of the presence of rich atomic emission and absorption lines in the spectra. The largest contribution to AGN energy output is due to thermal emission from the accretion disk which results in the big blue bump (BBB) with its peak in UV/optical band.

1.3.4 X-ray Emission

With increasing photon frequency, we get closer to the central engine of AGNs. The X-ray emission extends between ∼100 eV and ∼100 keV. They do not effectively penetrate Earth's atmosphere, so we need to use space observatories. An average X-ray SED is shown in Fig. 1.11 and 1.12. The main properties of the X-ray spectra of type I AGN are:

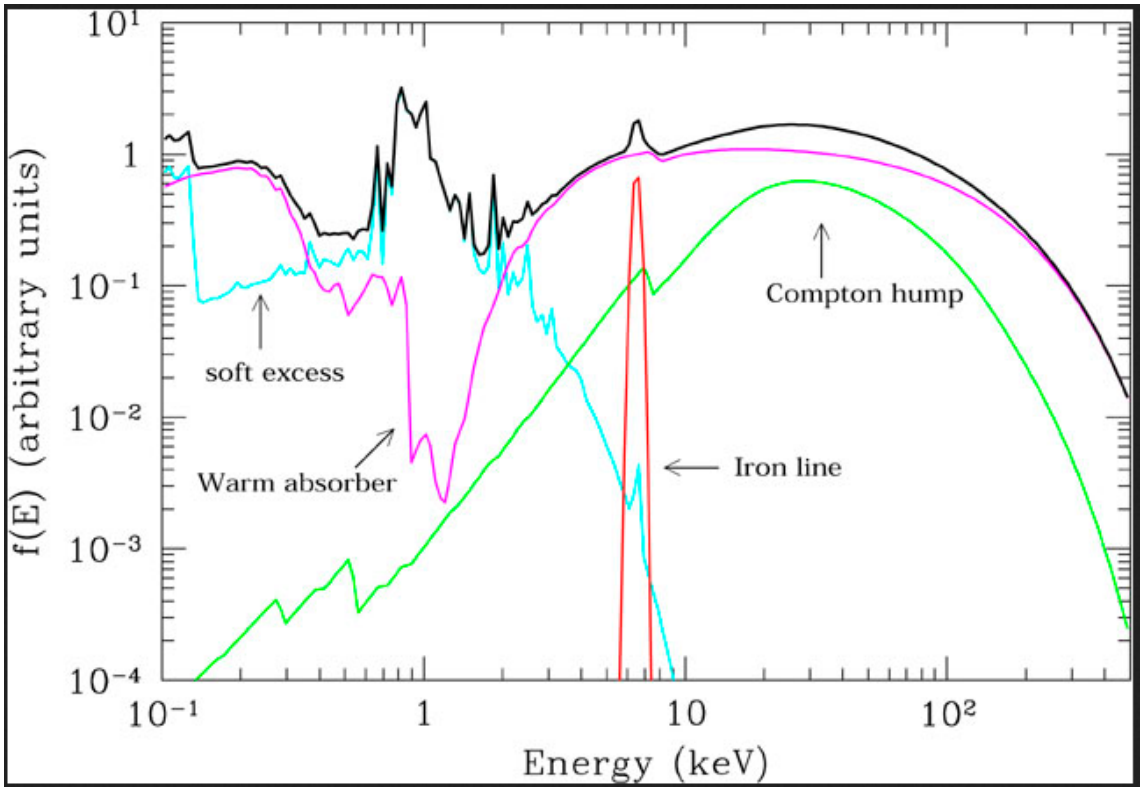

Figure 1.11: Average total spectrum (thick black line) and main components in the X-ray spectrum of a type I AGN. The main primary continuum component is a power law with an high energy cut-off at E $\sim$ 100 - 300 keV, absorbed at soft energies by warm gas with $N_H \sim 10^{21} - 10^{23}$ cm^{-2}. A cold reflection component is also shown. The most relevant narrow feature is the iron Kα emission line at 6.4 keV. Finally, a "soft excess" is shown, due to thermal emission of a Compton thin plasma with temperature kT $\sim$ 0.1 - 1 keV. Taken from Risaliti and Elvis (2004).

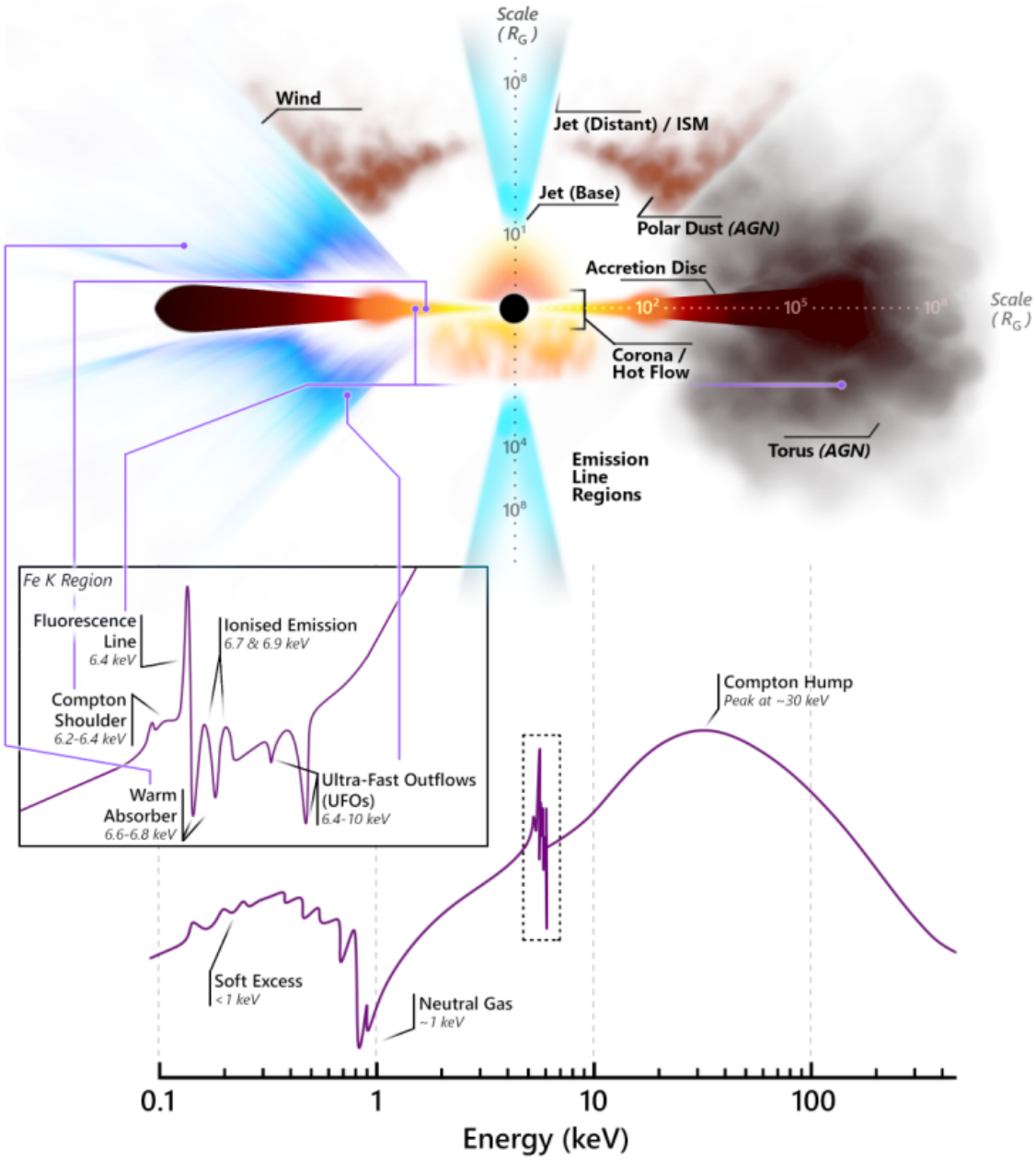

Figure 1.12: Schematic overview of the environments of accreting compact objects and their X-ray spectra. The left vs. right-hand side depict differing potential models of the outskirts that may be attributed to different physical conditions. Taken from Gandhi et al. (2022).

Primary Component

The low-energy photons in the accretion disk around a black hole, responsible for the thermal emission in the optical/UV band are scattered to X-ray energies by relativistic electrons, such as those in a corona above the disk, through inverse Compton scattering (Haardt and Maraschi (1993)). This results in a power-law continuum ($N(E) \propto E^{-\Gamma}$) with a photon index of $\Gamma \sim 2$, extending up to a few hundred keV and a high-energy cutoff at $E_{cut} \sim 100$ - 300 keV due to limited temperatures of the disk and the energy distribution of the electrons. The soft photons originate from the cool accretion disk (kT $<$ 50 eV), while the electron gas in the corona has a temperature of about kT$\sim$100 keV.

Reflection Component

The primary emission of AGN can be reprocessed through absorption and reflection, i.e., thomson scattered by ionized gas (Fig. 1.13). The main features of this reflection component are a continuum due to electron scattering (mainly direct Compton scattering) with a peak at $\sim$ 30 keV, and absorption and emission features typically below $\sim$ 10 keV (Risaliti and Elvis (2004)). The shape and strength of the hump depend on the geometry, chemical composition, and orientation with respect to the line of sight. The reflection efficiency is generally a few percent of the direct emission in the 2 - 10 keV range because of photoelectric absorption and rises to $\sim$ 30% at the 30 keV peak for a Compton-thick reflector (Ghisellini et al. (1994)). The efficiency drops if the reflecting medium is Compton thin. This material could be the outer accretion disk, the inner edge of the obscuring torus, or an outflowing wind.

Iron Line

Another important signature of the reflection process is the Fe Kα fluorescence emission line at E = 6.4 keV. It is the most prominent narrow feature in the 2 - 10 keV X-ray spectra of AGN corresponding to the Fe-K n = 2 - 1 transition of "cold" iron. It is observed in most Seyfert galaxies with a typical equivalent width (EW) of $\sim$50 eV (Shu et al. (2010)). Low-luminosity sources tend to show a

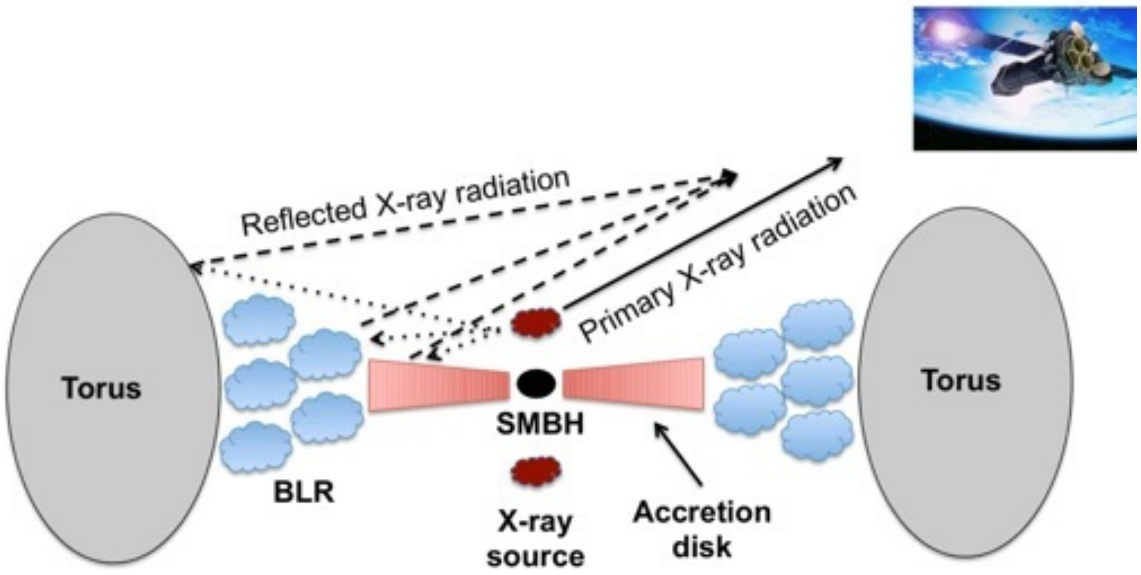

Figure 1.13: Reprocessing of X-ray radiation in AGN. Adapted from the PhD thesis work of Claudio Ricci.

stronger narrow Fe K line compared to more luminous AGNs. The line is usually ascribed to emission due to fluorescence in the inner part of the accretion disk. The Fe K line can be used to examine the movement of the material producing the line, and gravitational field at the location where the reflection takes place. A broad "red wing" extending to lower energies (Fig. 1.14) (Tanaka et al. (1995)) has been observed in this line profile. This is caused by the gravitational redshift and relativistic Doppler shift of an Fe-K line originating from the cool and dense matter in the vicinity of the central black hole. Such asymmetric broad lines are one of the best tools to search for general relativistic effects in strong gravity. From the observation of relativistically broadened Fe K emission lines we can measure the SMBH spin parameter. Also, the Fe Kβ line at E = 7.06 keV is often observable in many AGNs.

A second, narrow component of the Fe-K line is also observed in most AGNs from Fe XXV at E = 6.7 keV and Fe XXVI at E = 6.97 keV. The width of this narrow line is a few 1000 km/s (unresolved in CCD spectra from ASCA, Chandra ACIS, or XMM-Newton EPIC) which is similar to the width of optical and UV broad emission lines. This narrow component does not vary when the continuum

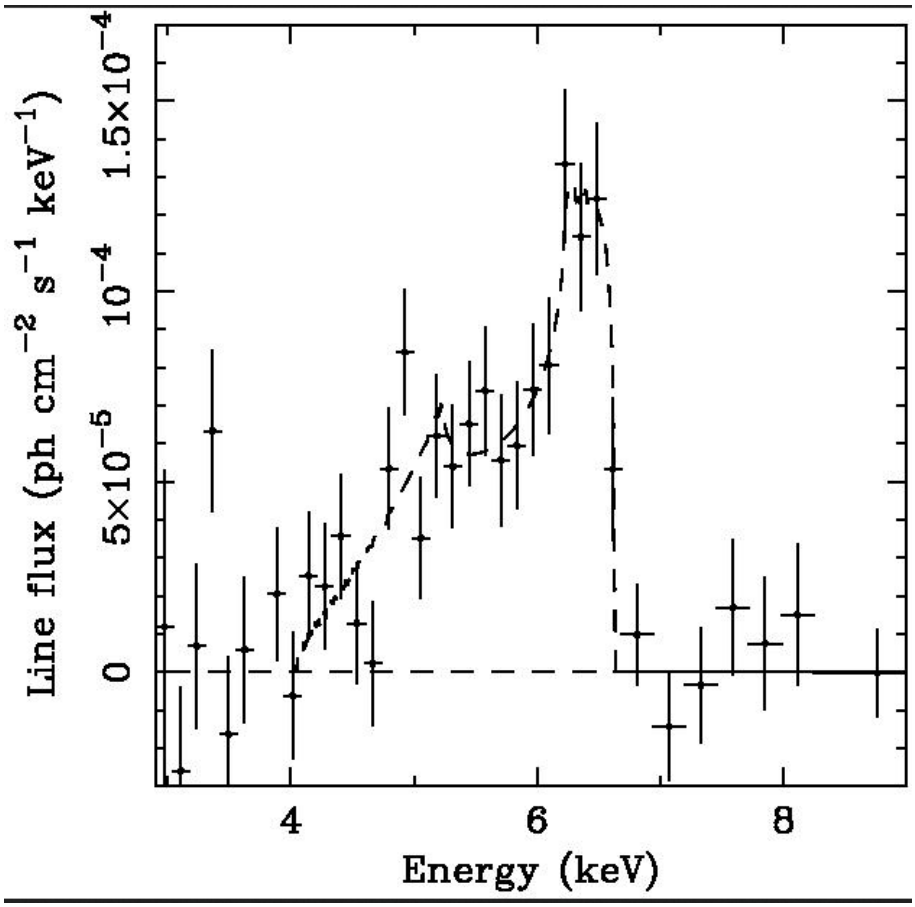

Figure 1.14: The line profile of iron K emission in the ASCA SIS spectrum of the Seyfert 1 galaxy MCG-6-30-15 (Tanaka et al. (1995)). The emission line is very broad, with full width at zero intensity of $\sim$ 100,000 km s^{-1}. The line shape is skewed toward energies lower than the rest-energy of the emission line (6.35 keV at the source redshift of 0.008). The dotted line shows the best-fit line profile from the model of Fabian et al. (1989), an externally-illuminated accretion disk around a Schwarzschild black hole.

varies which suggests an origin well beyond a few R_S, although a small radius can not be fully ruled out (Fabian et al. (2002)).

Warm Absorbers

Warm ionized absorber features are present in the soft X-ray spectra of half of the bright Type 1 AGNs. With the availability of high resolution soft X-ray spectra, obtained with the grating instruments onboard Chandra and XMM-Newton, it is seen that this component is formed by an outflowing gas with column densities up to $N_H \sim 10^{23}$ cm^{-2}, and often consists of several zones of ionized gas.

Soft Excess

Besides the primary power law continuum component, Type 1 AGNs frequently exhibit a strong, broad soft excess component below ∼2 keV. The precise origin of this component remains uncertain. Previously, the soft excess had often been associated with the high-energy tail of the thermal emission of the disk, potentially through Compton scattering within a hot accretion disk corona. Recently it was argued that the temperature of the disk should be nearly constant (kT $\sim$ 0.1-0.2 keV), regardless of the mass and luminosity of the AGN (Gierliński and Done (2004)). This means some other mechanism is at work here, as the temperature of the disk should depend on both the mass of the black hole and the accretion rate. Three different models have been suggested in order to explain the soft excess: (a) an additional Comptonization component (Dewangan et al. (2007)); (b) ionized reflection from the disk (Crummy et al. (2006)); (c) complex and/or ionized absorption (Gierliński and Done (2004)). In practice, a black body with a temperature between 0.1-0.2 keV is typically adopted to phenomenologically fit this component.

Chapter 2

Outflows

AGNs are primarily fueled by accretion processes onto SMBHs. This accretion typically results in the outflow of gas in various forms. At the galactic scale (d $\gtrsim$ kpc), molecular gas outflows are observed (Faucher-Giguère and Quataert (2012); Tombesi et al. (2015)). Closer to the AGN (d $\lesssim$ pc), UV outflows of weakly or moderately ionized gas occur (Crenshaw et al. (2003); Arav et al. (2015)). From the innermost circumnuclear region of AGNs, X-ray winds can originate.

Outflows have been detected in vast range of accreting astrophysical objects - from protostars to AGNs. Central SMBH interacts with its host galaxy via outflows from AGN. They have been detected in $\gtrsim$ 50% of nearby AGN, carrying kinetic energy which is a significant fraction of AGN power. This is evident from the blue-shifted absorption lines in the UV and X-ray spectra at different widths and velocities. To understand the evolution of these accreting objects and their interaction with local environment it is important to quantify the mass and energy flows involved in the process.

For AGNs, the the most powerful observed outflows can be divided into two classes: highly collimated, relativistic jets, and slower moving ($v \leq 0.2c$), more massive disk winds driven from the surface of the accretion disk surrounding the central supermassive black hole (SMBH). These disk winds are responsible for many observed AGN spectral features including the broad absorption lines seen in a sig-

nificant proportion of QSOs, known as BALQSOs.

Improvement in the X-ray spectroscopy observations after the launch of XMM-Newton and Chandra X-ray observatories revealed multiple absorption zones, covering a large ionization range, that are now routinely found in most bright AGNs. Absorption lines intrinsic to the source are systematically blue-shifted compared to the expected atomic transition levels, clearly indicating an AGN wind along our line-of-sight. Lines from several elements, such as Ne, Mg, Al, Si, S, Ar, Ca, and Fe, are typically present.

However, geometry of these winds and their launching mechanism are unknown. Several mechanisms have been suggested to produce the force required to accelerate these disk winds in AGN, such as the gas/thermal pressure, magnetocentrifugal forces and radiation pressure acting on spectral lines ("line driving"). All of these mechanisms can produce outflows in suitable conditions. X-ray outflows can be broadly divided in two main families: warm absorbers (WA) and Ultra-Fast Outflows (UFOs). They are discussed in the following sections.

2.1 Warm Absorbers

More than half of AGNs, mostly radio-quiet Seyfert 1s, exhibit X-ray winds with a series of blueshifted absorption features because of resonant transitions from various chemical elements at different charge states. These winds are known as warm absorbers (WAs) (Reynolds (1997); Crenshaw et al. (2003); Blustin et al. (2005); Tombesi et al. (2013); Fukumura et al. (2018a);Laha et al. (2021)). They are so named to denote the relatively low electron temperatures of the X-ray absorbing gas, typically below 10^5 K, which is significantly cooler than collisionally ionized thermal plasmas at similar ionization levels. These absorbers are thought to originate at distances of roughly 1-100 parsecs from the black hole, corresponding to regions like the outer disk, the torus, or the host galaxy environment. WA are primarily observed in the UV band through absorption lines associated with ions such

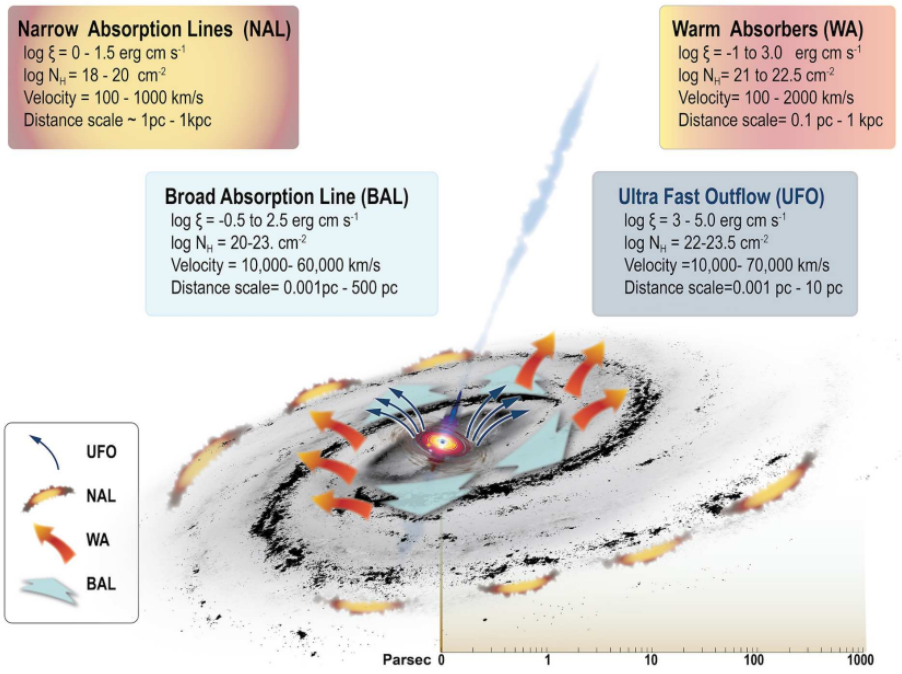

Figure 2.1: The different ionized outflows detected in AGN and their average physical parameters. Taken from Laha et al. (2021)

as O VII, O VIII, Ne IX, Ne X and Fe L. Their origin and geometrical structure are still not clearly understood (e.g., launching processes, nature of the outflows - either in a continuous or discrete patchy structure). Their physical properties are characterized by (Fukumura et al. (2022) and references therein):

- moderate hydrogen-equivalent column densities ($10^{20} \lesssim N_H[\mathrm{cm}^{-2}] \lesssim 10^{22}$),
- wide range of ionization parameters ($-1 \leq log\xi[\mathrm{erg\ cm\ s}^{-1}]) \leq 4$),
- slow to moderate LOS velocities ($v_{out}/c \lesssim 0.01$),
- turbulent velocities $v_{turb} \lesssim 1000$ km s^{-1},
- variability on timescales of months or years.

Studies on X-ray WAs reveal a global nature of the uniform column density profile as function of ionization parameter which can be observationally obtained from the absorption measure distribution (AMD) (Holczer et al. (2007); Behar (2009); Fukumura et al. (2018a)). This might indicate a well-organized, continuous outflow rather than a patchy, random distribution of discrete gas clouds.

2.2 Ultrafast Outflows

Ultra-fast outflows (UFOs) are observed in more than 40% of the local AGNs (Tombesi et al. (2010)). They are "extreme" type of X-ray absorbers, with mildly relativistic velocities, reaching up to ∼50% the speed of light. They are characterized by (Fukumura et al. (2022) and references therein):

- large column density($N_H \lesssim 10^{24}\mathrm{cm}^{-2}$),
- higher ionization parameter ($log\xi \sim 4-6$),
- near-relativistic velocity ($v_{out}/c \lesssim 0.1-0.7$),
- turbulent velocities $v_{turb} \lesssim 10000$ km s^{-1},
- variability on timescales of days.

The most distinguished UFO signature in the X-ray spectrum is the highly blue-shifted and ionized Fe K absorption lines attributed to Fe XXV/Fe XXVI ions (Tombesi et al. (2010), Tombesi et al. (2015); Nardini et al. (2015); Parker et al. (2017)). They have been detected in very luminous AGNs and also in sub-Eddington AGNs, such as radio-quiet Seyfert 1s (Tombesi et al. (2010)). They even seem to be present in fainter sources, such as Seyfert 2s, when the accretion rate is as low as $\sim$ 2% of the Eddington rate (Marinucci et al. (2018), for NGC 2992). Studies have also shown existence of UV/soft X-ray UFOs (e.g., C IV, O VIII, Ne IX/Ne X, Si XIV, S XVI, and Mg XII) in addition to the canonical Fe K UFOs (e.g., Gupta et al. (2013); Reeves et al. (2020)).

UFOs are expected to be produced well within the sphere of influence of the BH; they are most likely launched from a nearby gas reservoir in AGNs, such as an accretion disk in the deepest part of their gravitational potential. In general, when the AGN luminosity increases and/or the ionization parameter increases, the UFO velocity increases. They are considered one of the most important mechanisms of AGN feedback because of their mildly relativistic speeds and powerful kinetic energy.

2.3 Winds and Feedback

In addition to X-ray outflows, galactic-scale winds have been found in ionized and molecular phases, and are observed across optical to infrared band (Fiore et al. (2017)). These winds have lower velocities than UFOs, with maximum speeds around $\sim 10^3$ km/s, but exhibit much higher mass outflow rates, reaching up to $\sim 10^4 M_{\odot}\mathrm{yr}^{-1}$. These rates often exceed the star formation rate, implying that such outflows are primarily driven by the AGN rather than stellar activity. For cases where the host galaxy is observationally resolvable (also thanks to radio/IR interferometric measurements), the outflow morphology appears to be spherical or elliptical/biconical, consistent with an AGN origin (e.g. Cicone et al. (2014); Feruglio et al. (2015); Cresci et al. (2015) and Menci et al. (2019)).

Recent research suggests that galaxy-scale winds may be related to UFOs. Their interaction with surrounding interstellar medium (ISM) reduces their velocity and increases matter in outflows (Tombesi et al. (2015)). This hypothesis is supported by the properties of BAL winds, exhibiting properties between UFOs and galaxy-scale winds. Approximately 15% of optically-selected AGNs show BAL winds through blueshifted optical/UV lines (C IV, Si IV, N V), with $\dot{M}_{out} \sim 100 - 10^3 M_{\odot}\mathrm{yr}^{-1}$ and $v_{out} \sim 10^3 - 10^4$ km/s. Some of the fastest BAL winds reach speeds of 0.15 - 0.3c (Hamann et al. (2018); Bruni et al. (2019)). Their location is estimated at nuclear scales, about 1-100 pc from the center (Bruni et al. (2019)). Interestingly, some sources display both UFO and BAL absorption features, suggesting a common origin for X-ray and UV gas phases (e.g. PG1211+143 (Danehkar et al. (2018); Kriss et al. (2018)) and PDS456 (Hamann et al. (2018)). BLR winds may also represent an intermediate phase between nuclear, UFO-like winds and galaxy-scale outflows (Vietri et al. (2018), Vietri et al. (2020)). A composite view of the outflows at the different scales is shown in Fig. 2.2 (from Cicone et al. (2018)).

To explore this scenario quantitatively, we compare the energy liberated by the

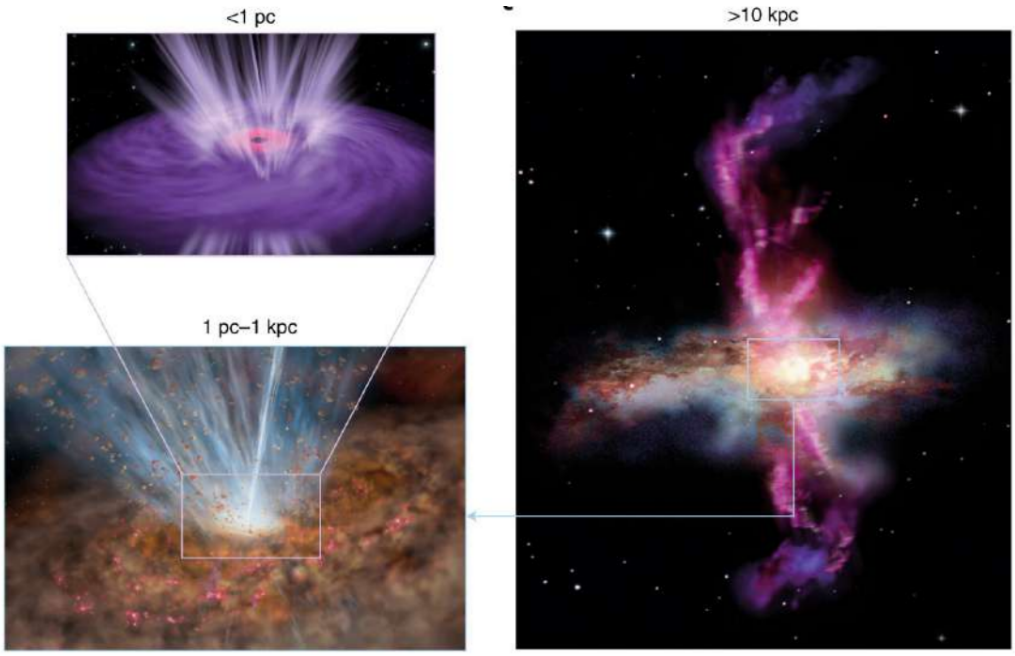

Figure 2.2: A schematic representation of the different outflow scales, from accretion disc to the surrounding ISM and to the boundaries of the galaxy. Taken from Cicone et al. (2018)

accretion process during the AGN lifetime with that of the host galaxy bulge:

$$E_{out} = \eta M_{BH} c^2 \approx 0.1 M_{BH} c^2 \tag{2.1}$$

Here, it is assumed that most of the SMBH mass comes directly from accretion (Soltan (1982); Pezzulli et al. (2016)) and the efficiency η is fixed at 0.1 for a Shakura and Sunyaev (1973) standard thin disk powered by a Schwarzschild black hole. Note that this is a conservative choice since $\eta_{Kerr} \sim 0.5$. The galaxy bulge binding energy is shaped by its stellar velocity dispersion σ_* and can be written as:

$$|E_{bulge}| \approx M_{bulge} \sigma_*^2 \tag{2.2}$$

where the modulus is used because the bulge is a bound system. Using the Magorrian relation (Magorrian et al. (1998)) we have:

$$M_{BH} \approx 0.006 M_{bulge} \sim 10^{-3} M_{bulge} \tag{2.3}$$

Rewriting E_{bulge} as a function of M_{BH} and using a typical value for $\sigma_* \sim 300$ km/s $\sim 10^{-3}$ c:

$$|E_{bulge}| \sim 10^{-3} M_{BH} c^2 \left(\frac{\sigma_*}{300 km/s} \right)^2 \tag{2.4}$$

Comparing Eqn. 2.1 and Eqn. 2.4 we get (King and Pounds (2015)):

$$E_{out} \approx 100 |E_{bulge}| \tag{2.5}$$

This suggests that the energy generated during the accretion could, theoretically, "unbind" the host galaxy bulge, assuming there is an efficient feedback mechanism to transfer this energy to the surrounding environment. However, it's more likely that the evolution of the AGN and its host galaxy is correlated — a process commonly referred to as co-evolution.

Various observational signs suggest a co-evolution between AGNs and their host galaxies (Fig. 2.3) (Kormendy and Ho (2013) and Fiore et al. (2017) and references therein). One of the most important evidence is the correlation between the mass of the SMBH and several properties of the host galaxy bulge, such as its mass, luminosity, and stellar velocity dispersion (σ_*). Among these, the M–σ is considered the driving relation (Ferrarese and Merritt (2000), Gebhardt et al. (2000)).

$$\frac{M_{BH}}{10^8 M_\odot} = \alpha \left(\frac{\sigma_*}{200 km/s} \right)^\beta \tag{2.6}$$

with measured values of the constants $\alpha \sim 1$, $\beta \sim 4$.

The discovery of the Magorrian and M–σ relations questioned the influence that SMBHs and the stars in the host galaxy bulges have on each other. One theory suggests some kind of "feedback" mechanism that regulates the correlation between black hole mass and stellar velocity dispersion. Silk and Rees (1998) suggested a feedback mechanism where they proposed that a SMBH forms first from a collapsing gas cloud on rapid timescales before significant star formation occurs in the bulge. The SMBH then accretes nearby matter, emitting radiation that can drive winds,

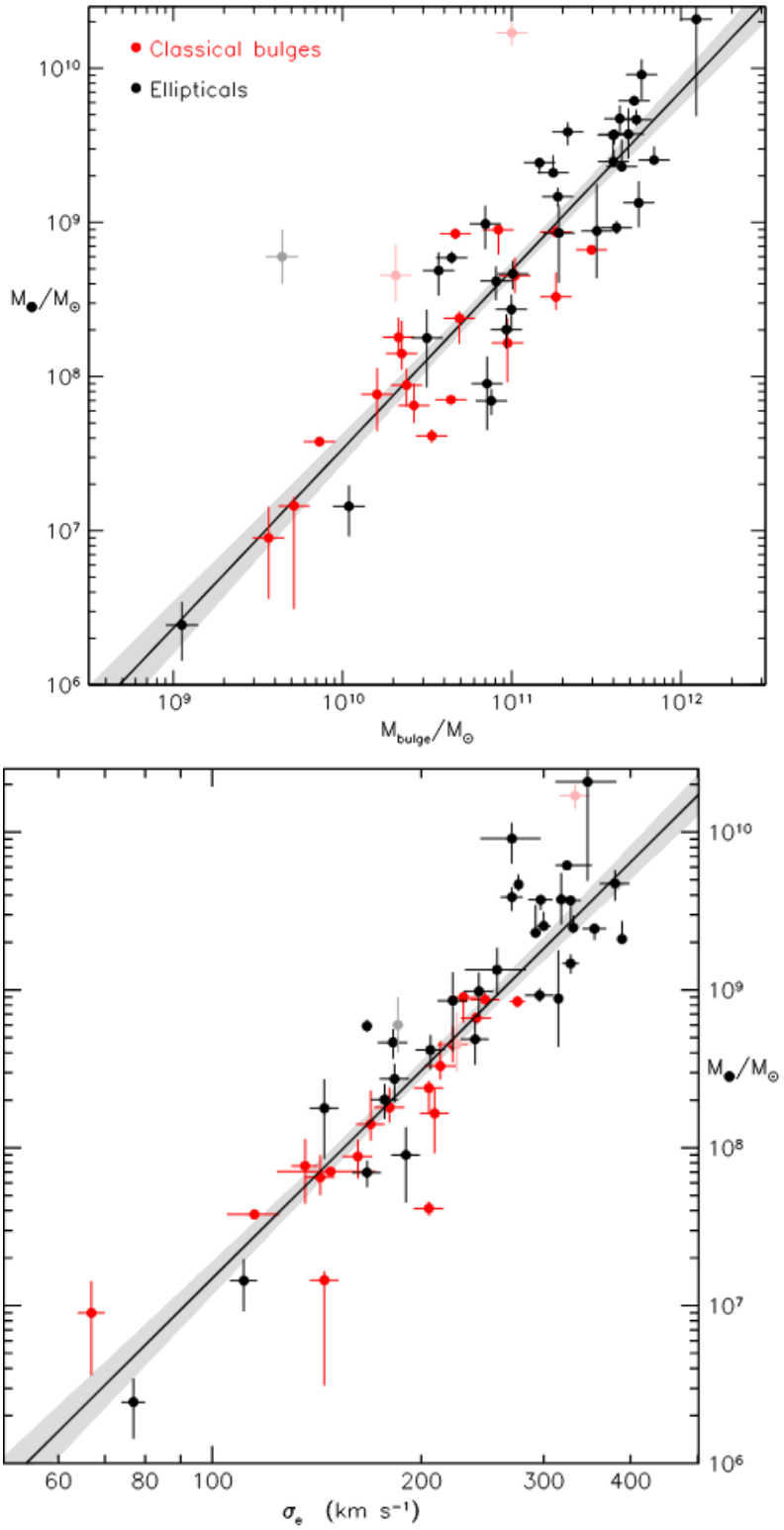

Figure 2.3: Top: Correlations between BH mass M_{BH} (y-axis) and bulge mass M_{bulge} (x-axis). Bottom: Correlation BH mass M_{BH} (y-axis) and the bulge velocity dispersion σ (x-axis). Solid line and shaded region represent the least-squares fit and the associated 1σ uncertainty respectively. Taken from Kormendy and Ho (2013).

which can regulate further accretion. This accretion flow will continue until rate of deposition of mechanical energy into the infalling gas becomes large. This model from Silk & Rees predicts a slope of $\beta = 5$ considering pure energy-driven feedback, which is slightly higher than the observed one. Other models predicted a slope $\beta = 4$ considering momentum-driven feedback.

The relation, at its first order, can be understood by assuming that the AGN core is accreting close to the Eddington limit (King and Pounds (2015)). The radiation pressure will drive out a fraction f of the gas mass $\mathrm{M_{bulge}}$, which is assumed to be spherical with radius R. In steady mode, the force (or momentum rate) from the time-average luminosity $\dot{P}_{rad} = L_{Edd}/c$, will be equal to the gravitational force that keeps the mass fM_{bulge} just outside the bulge at radius R:

$$\frac{L_{Edd}}{c} = \frac{GM_{bulge}fM_{bulge}}{R^2} \tag{2.7}$$

Substituting $L_{Edd} = 4\pi Gcm_pM_{BH}/\sigma_T$ and assuming that the bulge is an isothermal sphere, i.e., $\rho(R) = \sigma_*^2/2\pi GR^2$ (Schneider (2006)), the mass inside R is a function of the velocity dispersion of the gas: $M(< R) \sim 2R\sigma_*^2/G$. Thus:

$$\frac{M_{bulge}}{R} = \frac{2\sigma_*^2}{G} \tag{2.8}$$

Substituting in eqn. 2.7 we get:

$$\frac{4\pi GM_{BH}m_p}{\sigma_T} = Gf\left(\frac{2\sigma_*^2}{G}\right)^2 \tag{2.9}$$

Rearranging eqn. 2.9, we can use the velocity dispersion to measure the mass of the central engine:

$$M_{BH} = f\left(\frac{\sigma_T}{\pi G^2 m_p}\right)\sigma_*^4 \tag{2.10}$$

Thus, it is expected that $M_{BH} \propto \sigma_*^4$, where a fraction $f \sim 0.1$ closely matches the measured values. This suggests a nearly spherical geometry, with the AGN affecting the bulge uniformly in all directions. Faber and Jackson (1976) found a

similar relationship between the total luminosities and stellar velocity dispersions in elliptical galaxies. Their luminosities also exhibit a σ_*^4 dependence, known as the Faber-Jackson relation.

Murray et al. (2005) pointed out that it would be remarkable if this similarity in the M–σ and L–σ relations were a pure coincidence. They determined the limiting luminosity above which the central AGN would drive away a significant amount of gas from the galaxy and stop the accretion (and star formation) on the bulge. From Eq. 2.7 and Eq. 2.8, without substituting the Eddington luminosity, we get:

$$L \sim \left(\frac{4c}{G}\right) f\sigma_*^4 \tag{2.11}$$

Also in the Faber-Jackson relation, a value of $f \sim 0.1$ seems to apply.

UFOs are the prime candidates to transfer the AGN energy outward and explain the observed relations between the AGN and the host galaxy because of their kinetic outflow rates which is of the order of 0.01-1 times the AGN luminosity. Theoretical models suggest an initial phase of inefficient energy transfer which later evolves into a highly efficient one (King and Pounds (2015)). When the inner disk wind (like a UFO) interacts with the ISM of the host galaxy, it creates a shock. The shock-heated gas reaches extremely high temperatures (up to $10^{10} - 10^{11}$ K) and cools down mainly through inverse Compton scattering with the AGN's radiation because of its high ionization state. This happens if the shock is very close to the core and/or if the AGN luminosity is high. For the resultant momentum-driven galaxy-scale outflow, only the momentum rate of the inner disk wind is conserved ("momentum-conserving phase" Fig. 2.4):

$$\dot{P}_{shock} = \dot{M}_{shock}\ v_S = \dot{M}_{UFO}\ v_{UFO} = \dot{P}_{UFO} \tag{2.12}$$

where v_S is the velocity of the shock. The observed velocity of the shocked outflow decreases than the inner UFO ones (about $\sim$ 50 times smaller) as we move away from the nucleus. As a result, the mass outflow rate should increase in order to

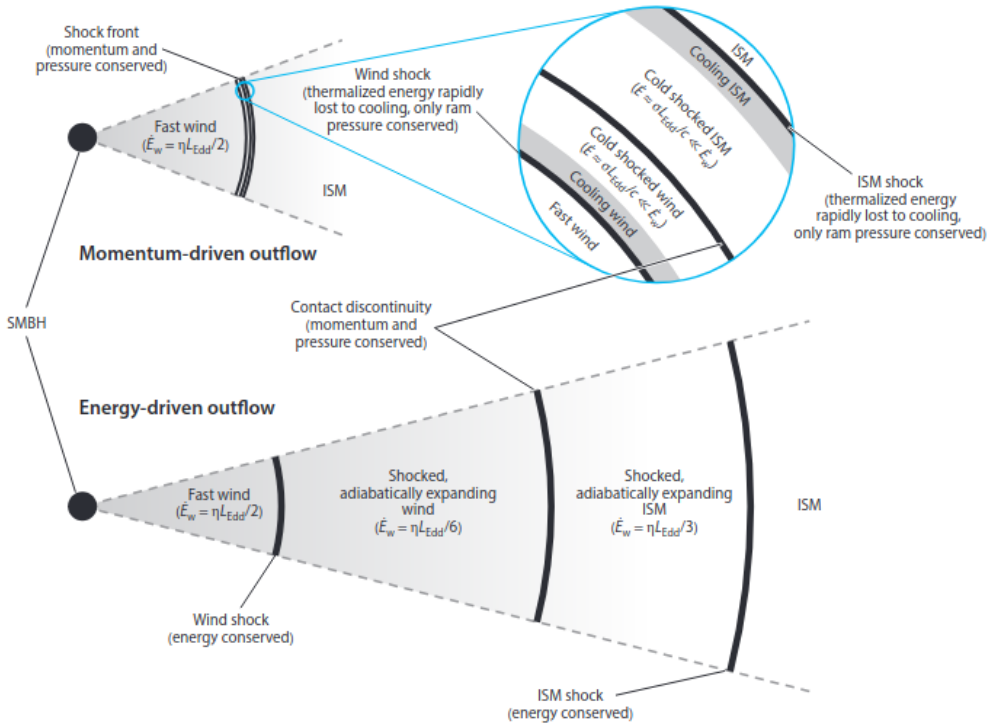

Figure 2.4: Shock regions in the momentum and energy-conserving cases (top and bottom cartoons, respectively). Taken from King and Pounds (2015).

conserve momentum:

$$\dot{M}_{shock} = \frac{\dot{M}_{UFO}\ v_{UFO}}{v_S} \approx 50 \dot{M}_{UFO}. \tag{2.13}$$

As the shock propagates away from the AGN's radiation field, cooling becomes less effective, and the shocked gas conserves its energy and expands adiabatically during an "energy-conserving phase" (Fig. 2.4). In this phase, the coupling with the ISM becomes highly efficient, enabling the outflowing gas to expand to galactic scales. The post-shock region then sweeps away the surrounding gas, and the outflow is observed in ionized and molecular phases on galactic scales. During this phase, the post-shock energy rate must be equal to the pre-shock one:

$$\dot{E}_{shock} = \frac{1}{2}\dot{M}_{shock}\ v_S^2 = \frac{1}{2}\dot{M}_{UFO}\ v_{UFO}^2 = \dot{E}_{UFO}. \tag{2.14}$$

Considering the same velocities as before, the post-shock momentum rate $\dot{M}_{shock}$

must be far higher than the UFO $\dot{M}_{UFO}$:

$$\dot{M}_{shock} = \dot{M}_{UFO} \left(\frac{v_{UFO}}{v_S}\right)^2 \approx 2500\dot{M}_{UFO}. \tag{2.15}$$

Due to this "momentum boost", galaxy-scale winds are massive enough to exert significant feedback on the host galaxy and alter the equilibrium of its reservoir gas. These winds drive the swept-up ISM out of the galaxy bulge leaving it red and dead. Therefore, it is able to quench the star formation in the host galaxy and regulate its evolution (Zubovas and King (2012)).

It is important to notice that the correlations between SMBH and host galaxy are affected by their complex evolutionary history, including mergers, secular instabilities and the influence of the galaxy cluster. Several results suggested that similar M_{BH}-bulge relations can also be obtained if SMBH and bulges formed simultaneously, without a direct interaction between them (Menci et al. (2003)). A more promising approach is to look at "derivative" quantities, such as the cosmological evolution of SMBH and the luminosity density of galaxies. A correspondence has been found between AGN and galactic activity as a function of redshift (Brandt and Alexander (2015)), possibily driven by the AGN feedback toward its host galaxy.

2.4 Detection and Analysis of X-ray Winds

X-ray winds are primarily identified through the resonant transitions of highly ionized elements whose absorption lines get blue-shifted by Doppler motions. This blueshift of absorption features from their rest frame energy occurs when a part of the continuum is absorbed by the layers of the wind. This happens when the wind is positioned between the emitting source and the observer. This corresponds to the motion of the gas outward from the nucleus of the source towards the observer, indicating an outflow. By convention, a negative velocity indicates a blueshift of atomic feature. On the contrary, a redshift of the atomic features indicates an inflowing gas and is denoted by positive velocity. The properties of these winds can

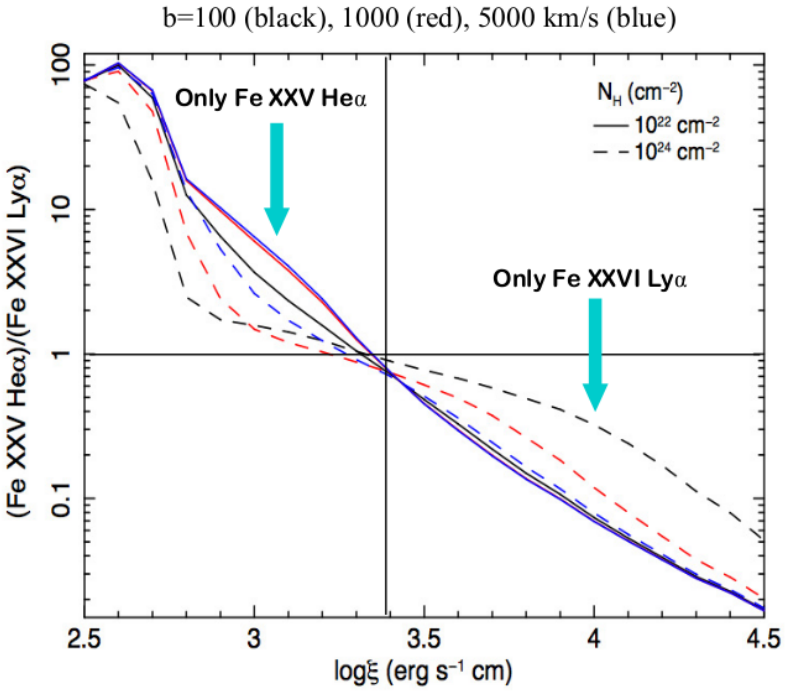

Figure 2.5: The abundance of each ion and the relative intensity of the spectral lines depend on the ionization parameter of the plasma, logξ. For example, here we can see Fe XXV dominates below log$\xi \sim 3.5$, beyond which Fe XXVI dominates. Taken from Tombesi et al. (2011).

be studied by analyzing these lines. The most important line tracers to characterise the observational appearance of winds or outflows are:

- Line identification is an indicator of both metallicity and the degree of ionization. The ionization level of the plasma directly influences the ion abundances (Fig. 2.5). The ionization status is quantified by the ionization parameter ξ, defined by Tarter et al. (1969) as the ratio between the ionizing photon flux and the gas surface density:

$$\xi = \frac{L_{ion}}{nr^2} \tag{2.16}$$

  where L_{ion} is the ionizing luminosity at energies between 13.6 eV to 13.6 keV, r is the distance of the wind from the SMBH and n is its number density.

- Blueshifts relative to the rest-frame energy of absorption lines are proportional to the outflow velocity along the line of sight (v_{wind}). For motion occurring

entirely in the LOS direction, the following relationship holds:

$$1 + z = \sqrt{\frac{1+\beta}{1-\beta}} \tag{2.17}$$

where $\beta = v_{wind}/c$ is the outflow velocity in units of speed of light c and z is the redshift.

$$\text{z} \approx \beta \text{ for } v_{wind} \ll c \quad .$$

- The broadening of spectral lines provides information about the turbulent velocity within the absorbing gas. Higher turbulent velocities result in broader lines. The velocity broadening parameter b is given by:

$$b = \sqrt{v_{th}^2 + v_{turb}^2} \tag{2.18}$$

where v_{th} is the thermal velocity and v_{turb} is the turbulent velocity (velocity dispersion along the LOS). The temperature of the gas can be further inferred from the thermal velocity:

$$v_{th} = \sqrt{\frac{2k_BT}{m}} \tag{2.19}$$

Typically, the contribution of thermal velocity to line broadening is very small ($v_{th} \sim$ 50 km/s for T$\sim 10^7$K for iron nuclei) compared to the observed turbulent velocities ($v_{turb} \sim$ 1000-10000 km/s). Thus, line broadening is often influenced by other factors like kinematics and turbulence.

- The depth of absorption lines is quantified by the neutral hydrogen column density:

$$N_H = \int_{r_{initial}}^{r_{final}} n(r)dr \approx n\Delta r \tag{2.20}$$

Here, it is assumed that the density is approximately constant within the wind layer. N_H is related to the amount of absorbing gas present in the wind.

- The equivalent width (EW) of a spectral line is a measure of the strength of that line relative to the surrounding continuum emission. It gives the area of the line on a plot of intensity versus wavelength or frequency. It is found by

forming a rectangle whose height equals that of the continuum emission and the width is such that the area of the rectangle is equal to the area under the spectral line. Mathematically, it can be expressed as:

$$EW = \int \frac{F_l(\lambda) - F_c(\lambda)}{F_c(\lambda)} d\lambda \tag{2.21}$$

where F_l is the line flux at a given wavelength λ and F_c is the continuum flux at the same wavelength. For an emission line, EW is considered to be positive, while for an absorption line, it is negative. The integral is taken over the entire line profile.

- The curve of growth (CoG) analysis of absorption lines illustrates the relationship between the equivalent width (EW) and the opacity (τ) or column density (N_H) of the absorbing material (Fig. 2.6). By estimating the EW from spectral observations, we can determine N_H.

- For a given turbulent velocity, the EW increases linearly with N_H until the Gaussian line profile saturates, with saturation occurring sooner for lower v_{turb}. In the absence of turbulence, only photons that precisely match the energy of the transition are absorbed. However, in a turbulent gas, the absorption capability increases due to light being slightly blue-shifted and red-shifted, allowing the gas to absorb a broader range of photon energies.

- When a spectral line is saturated, it becomes challenging to accurately estimate N_H from the EW, and only a lower limit can be established. This is because the gas density is too high relative to the incident light, preventing reprocessed radiation from emerging, which impedes accurate column density estimation. In the initial linear regime, the relationship is:

$$EW \propto \tau \propto N_H. \tag{2.22}$$

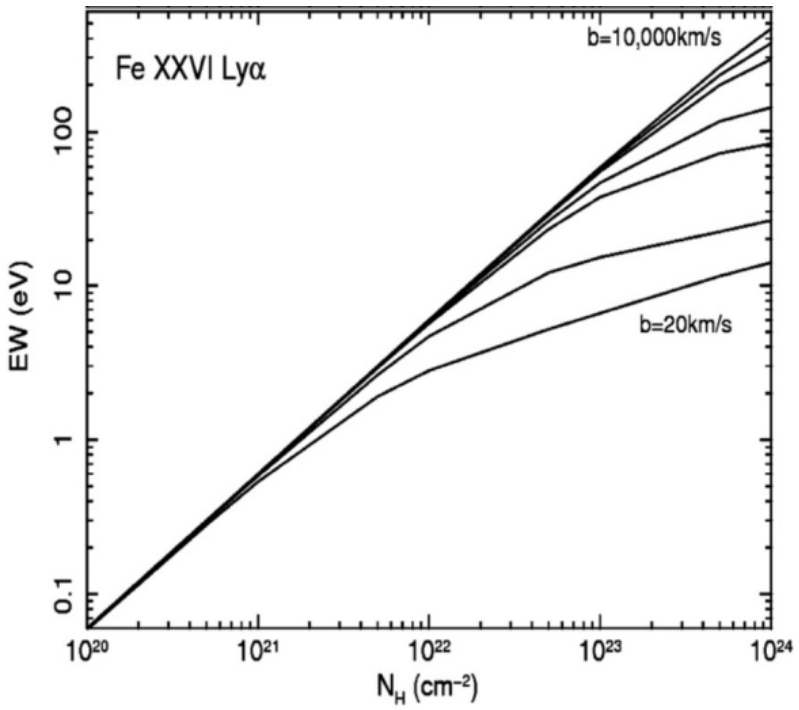

Figure 2.6: CoG of Fe XXVI Lyα for different broadening (turbulent) velocities b. It can be seen that when b increases, the linear region becomes wider. From Tombesi et al. (2011)

2.5 Photoionization modelling of Winds

Spectroscopic observations of X-ray outflows are typically analyzed using templates from photoionization codes like Cloudy (Ferland et al. (1998), Ferland et al. (2017)), XSTAR (Kallman and Bautista (2001)) and PION in SPEX (Kaastra et al. (1996)). Information about the gas dynamics can be inferred by assuming that the winds or outflows are in photoionization equilibrium with the central UV and X-ray continuum luminosity. The ionization state of the gas is primarily determined by radiation rather than collisions, indicating that the gas is in an equilibrium configuration influenced by the central radiation source. Therefore, these codes assume radiation as the primary ionization source and local thermodynamic equilibrium (LTE) to model the physical conditions of X-ray outflows. The codes are a function of:

- the luminosity and spectral energy distribution (SED) of the incident continuum,
- the distance of the wind from the BH,

- thermodynamic and geometric stratification of the clouds,
- elemental abundances and atomic transitions,
- radiative transfer,
- gas kinematics and turbulence.

2.5.1 XSTAR

XSTAR[1] is a photoionization code developed by NASA and included in the Heasoft package. We use XSTAR for our analysis because of its widespread adoption in UFO fitting. It is also incorporated in WINE which we will discuss later. The general working scheme of XSTAR is analogous to that of Cloudy and other similar codes.

The XSTAR code runs in two steps: determining the ionization status of the gas based on incident luminosity and gas properties, such as its number and column densities and its distance from the source, and calculating equilibrium which is obtained by balancing the radiative heating sources (ionization and Compton) and cooling mechanisms (recombination, bremsstrahlung, radiative deexcitation of bound levels). Once the gas ionic population is known, radiative transfer calculations examine the photon-matter interaction, considering all photon-related physical processes (free-free, bound-free, free-bound, radiative recombination continua). The details of every interaction, such as energy levels, transition probabilities, and cross sections, are found in the atomic database (Bautista and Kallman (2001) and Mendoza et al. (2021)).

The input quantities in XSTAR are:

- The incident spectrum profile and its integrated luminosity in the 1-1000 Ry energy range, i.e. the ionising luminosity L_{ion} entering in the definition of the ionisation parameter ξ;

[1]XSTAR is available at the following link.

- ξ_0, n_0, where the subscript 0 indicates that they must be specified at the inner radius of the gas. From these quantities and L_{ion}, the radius r_0 is derived;

- α, the coefficient regulating the radial dependence of the density n: $n = n_0(\frac{r_0}{r})^{\alpha}$;

- $N_H = \int_{r_0}^{r_1} n(r)dr$, the gas column density. The ending radius r_1 can be calculated from N_H, n_0, r_0, α;

- v_{turb} the gas velocity dispersion regulating the broadening of the absorption features.

After a simulation has converged to a solution, several key outputs are generated. The most important ones are the transmitted spectrum, which is the incident spectrum absorbed by the gas, and the spectrum emitted by the gas itself. These two spectra are conceptually symmetrical since the same gas produces absorption in the transmitted spectrum and emission in the emitted spectrum, despite differences in individual radiative processes. Additionally, a list of the atomic transition emissivities is generated as well, in units of erg s^{-1} cm^{-3} (luminosity density).

Even though its widespread use in astrophysics, the main physical assumptions of XSTAR need to be addressed while dealing with the relativistically-broadened profiles of UFOs and with fast disk winds in general. The most important assumptions are as follows:

- The gas is assumed to be a spherically symmetric shell centered around the luminosity source, which is treated as a point-like object. This configuration allows for the calculation of absorption profiles under the assumption that the radiation field strikes the gas shell perpendicularly.

- The gas is assumed to be at rest. Atomic line absorptions are represented by Gaussian features, whose 1 σ amplitude is given by the maximum between the local thermal velocity v_{th} and the turbulent velocity v_{turb}.

- As a result, the emission spectrum is simply given by the atomic transitions, with energies corresponding to the rest frame ones and the luminosity calculated from the emissivities multiplied by the shell volume, i.e., $\frac{3}{4}\pi(r_1^3 - r_0^3)$.

Spherical symmetry is not supported by the observations, which instead suggest a more structured medium with some degree of clumpiness and a covering factor (i.e., the fraction of solid angle covered by the outflow) smaller than one. Moreover, it is also expected that the hemisphere beyond the accretion disk (with respect to the line of sight) is covered by the disk itself and hence unobservable. Finally, the theory of wind driving suggests a strong degree of spatial anisotropy for the outflow, regardless of the driving mechanism.

The standard method to account for an outflowing velocity (v_{out}) is by blueshifting the computed model spectra during data fitting. The best-fit blueshift, after being adjusted for the host galaxy's systemic redshift, gives v_{out}. However, there are two key limitations: first, the real outflow velocities may be better represented by a velocity distribution (i.e., a velocity profile) rather than a single (average) value due to complex acceleration patterns. Second, special relativity effects significantly alter gas opacity and the equivalent width of both absorption and emission features in the spectrum (Marzi et al. (2023)).

When creating photo-ionization grids for data fitting, it is common practice to enhance the ionizing luminosity normalization to simulate reprocessing by a thin gas layer (i.e., $\Delta r/r \ll 1$). Although we start with initial parameters ξ_0 and n_0 in the first layer, deeper into a thick shell, physical conditions change, and the whole absorber experiences a wide range of densities and ionizations. Thus, the final output must consider a large number of ion species and transitions, resulting in significant computational time. Given

$$L_{ion} = \xi n r^2 \approx \xi \frac{N_H}{\Delta r} r^2 \tag{2.23}$$

and $L_{ion} \propto r^2$, if $L_{ion} \to \infty$, then $r \approx r_0$ increases and $\Delta r/r \to 0$. Hence, we are

modeling the photoionization from a thin layer of gas.

2.5.2 WINE

To overcome the limitations of XSTAR, a new model called Wind in the Ionized Nuclear Environment (WINE[2]) was developed by Luminari et al. (Luminari et al. (2018), Luminari et al. (2020), Luminari et al. (2021), Luminari (2024)). This model integrates the XSTAR photoionization code with two new components: a Monte Carlo approach to simulate the emitting region, which convolves line emissivities with realistic emission templates based on the outflow geometry, and a special relativity treatment of radiative transfer to accurately represent the gas motion. The WINE program is written in bash language, with the absorption and emission routines in Python. The program allows to explore a whole range of physical and geometrical parameters given by the user. This is useful for analysing the parameter space and to minimise the fit of spectral wind features. The synthetic spectra obtained with WINE can be submitted to spectral fitting programs, such as XSPEC for the X-ray band. A schematic flowchart of WINE is presented in Fig. 2.7.

In this model, the wind is described as a biconical region, centred on the SMBH. The model is based on the assumption that the cone symmetry axis coincides with the rotation axis of the accretion disc. It also retains the XSTAR approximation of a point source luminosity located at the vertex of the cone, i.e. the centre of the accretion disk. The rear cone is considered to be obscured by the disk (in yellow, see Fig. 2.8). The wind is enclosed by an initial and final radius, r_0, r_1, and has an inner and outer opening angle, θ_{in} and θ_{out}, respectively (shown in red and green in Fig. 2.8). This geometry agrees with most of the simulations on accretion disk wind in the literature and is in analogy with galactic scale outflows.

The input parameters for WINE are (the top green box in Fig. 2.7):

- L_{ion}, the incident ionizing luminosity in the 1-1000 Ry (13.6 eV - 13.6 keV)

[2]This section has been adapted from Luminari (2024).

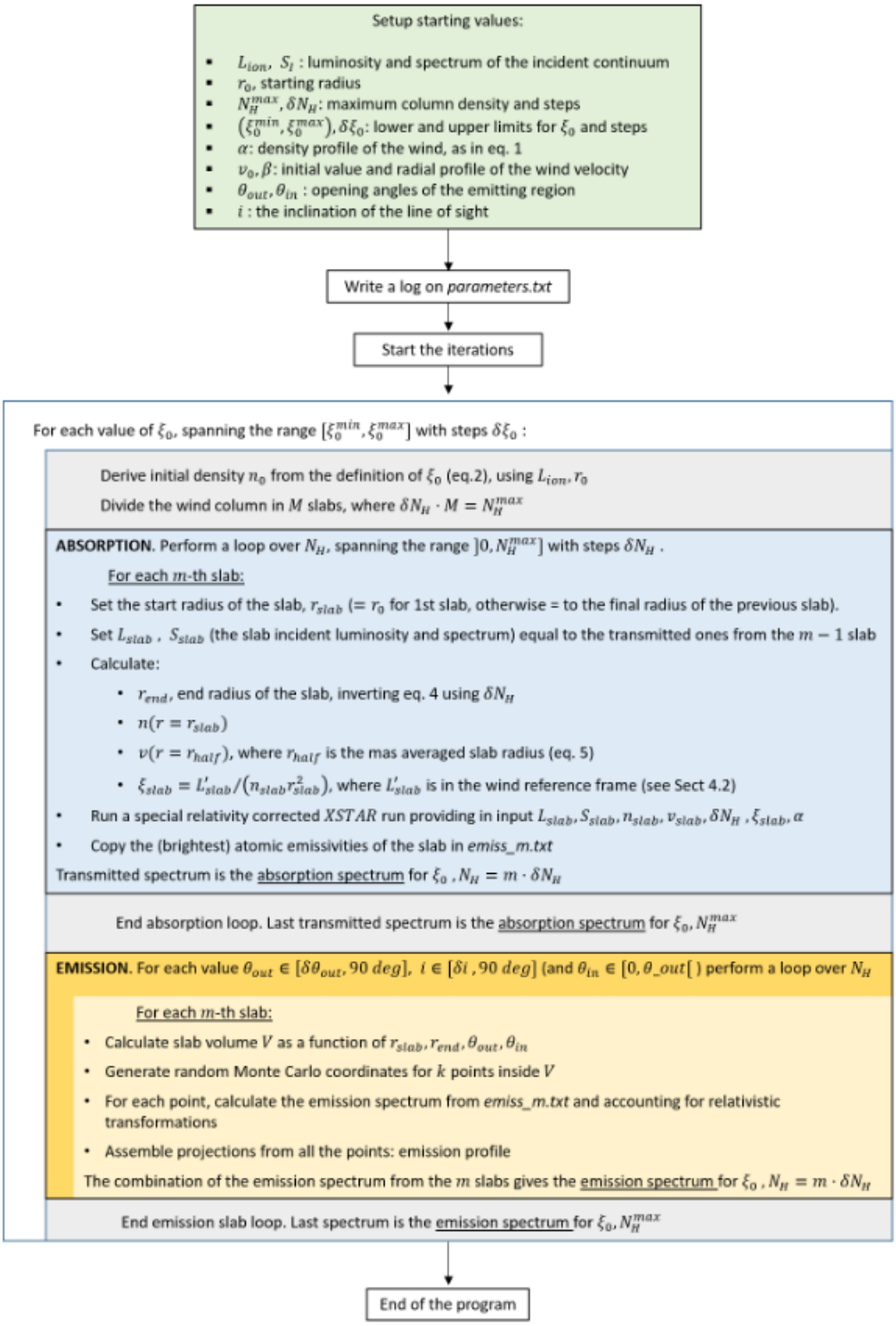

Figure 2.7: Flowchart of the main steps of the WINE model. Taken from Luminari (2024).

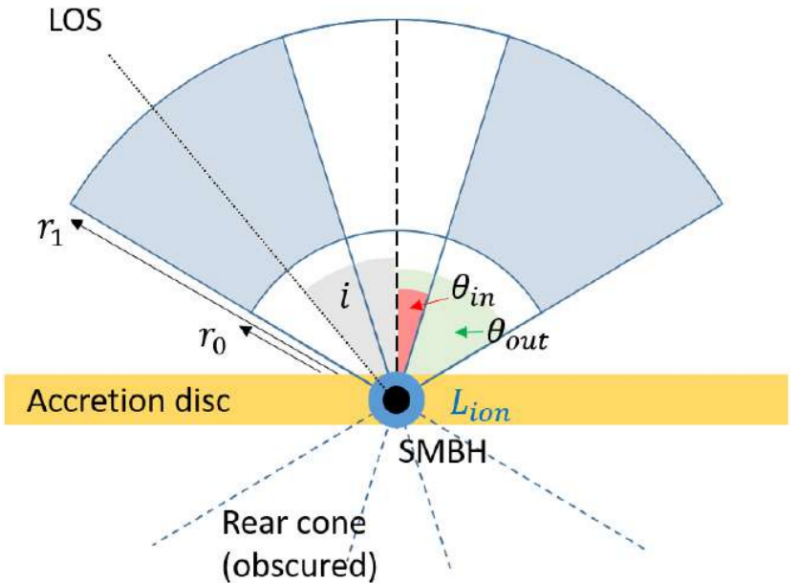

Figure 2.8: Geometry of the WINE model. Gray shaded area indicate the wind volume. θ_{in}, θ_{out} represents the wind inner and outer opening angle with respect to the symmetry axis (vertical dotted line). The line of sight (LOS) has an inclination angle i with respect to the axis. Accretion disc is represented with a yellow bar, and the black and blue dots indicate respectively the supermassive black hole and the ionising and X-ray luminosity sources, which are assumed as point like. Finally, r_0, r_1 indicate the wind initial and final radius, respectively. Taken from Luminari (2024).

interval or, equivalently, in the 2 - 10 keV interval.

- The spectrum shape S_I, which can have one of the following forms:
  - A power-law with spectral index Γ
  - A black-body with temperature kT (in eV)
  - A custom spectrum uploaded by the user

- r_0, the initial radius of the cone. It can be expressed in cm or in gravitational radius r_G. In the second case, the black hole mass M_{BH} must also be provided. n_0, in turn, can be derived from r_0, ξ_0, L_{ion}.

- N_H^{max}, δN_H, the maximum column density of the wind and the sampling step

- ξ_0^{min}, ξ_0^{max}, $\delta\xi_0$, the minimum and maximum ionization parameter at the base of the wind and the sampling step

- α, the index of the density profile given by:

$$n(r) = n_0 \left(\frac{r}{r_0}\right)^{-\alpha} \tag{2.24}$$

- v_0, β, the starting velocity and the index of the velocity profile:

$$v(r) = v_0 \left(\frac{r}{r_0}\right)^{-\beta} \tag{2.25}$$

  β can also be linked to α using the relations (Faucher-Giguère and Quataert (2012)):

$$\beta = \frac{\alpha - 2}{2} \tag{2.26}$$

  for momentum conserving flows, and

$$\beta = \frac{\alpha - 2}{3} \tag{2.27}$$

  for energy conserving flows.

- $\delta\theta_{out}$, the sampling step for the opening angle θ_{out}, which spans the interval]0, 90] deg

- δi, the sampling step of the inclination of the LOS i, which spans the interval [0, 90] deg

- Q, the number of steps for the inner cavity θ_{in}, which spans the interval [0, θ_{out}[

A multilayer approach is used to model the scaling of the wind density n(r) and velocity profiles v(r) along the radial distance r from the luminosity source. During the simulation, the outer (first level) iteration is performed over the ionization parameter (light grey box in Fig. 2.7) in the range [ξ_0^{min}, ξ_0^{max}] with steps $\delta\xi_0$. For each value of ξ_0, the initial density of the wind n_0 is determined by inverting the definition of ξ_0:

$$\xi_0 \equiv \xi(r = r_0) = \frac{L_{ion}}{n_0(r_0)^2} \tag{2.28}$$

and the final radius of the wind r_1 is found by inverting the definition of N_H:

$$N_H^{max} = \int_{r_0}^{r_1} n(r)dr \tag{2.29}$$

The wind column is divided into M shells with constant column density $\delta N_H = N_H^{max}/M$. An inner iteration (second level, blue box in Fig. 2.7) is performed over the slabs, with m ranging from 1 to M. Starting from the innermost shell, photoionization and radiative transfer is performed using XSTAR. The resulting transmitted spectrum and luminosity serve as inputs for the subsequent shells, iterating this process across all M shells until the total column density N_H is reached. The value of δN_H is carefully chosen to balance computational efficiency with accuracy. It has been observed that for a typical UFO and WA parameter space, a value of $\delta N_H = 10^{22}$ cm^{-2} ensures smooth transitions between the shells so that the multilayer approximation accurately reproduces a continuous radiative transfer within the wind. The code also updates the shell velocity to account for special relativity effects during radiative transfer. This way, the wind absorption spectrum is obtained. The iterative procedure allows to accurately model the wind features as a function of the density and velocity profiles, thus overcoming the XSTAR assumption of a layer of gas at rest.

The emission spectrum is derived similarly. For each slab, random Monte Carlo coordinates are assigned to a large number of points to evenly fill the slab volume, which depends on the starting and ending radii of the slab, as well as θ_{in} and θ_{out}. The projection along the line of sight for each point's luminosity and energy (i.e., relativistic beaming and Doppler effects) is then calculated. The combined response of all points yields the total slab emission profile. Slab spectrum is obtained by the convolution of the atomic emissivities with the emission profile. The wind emission spectrum is finally obtained from the sum of all slab emission spectra. The Monte Carlo procedure allows to overcome the XSTAR assumption of spherical symmetry, thus enabling to directly probe the source geometry and its covering factor.

The WINE structure was designed to minimise the number of physical assumptions and to directly probe the most important outflow parameters. Its numerical accuracy matches the spectral resolution of present day X-ray gratings and CCDs and also next-generation microcalorimeters, such as those onboard XRISM and Athena. Due to the modular structure of WINE, additional features, such as an angular dependence of the wind properties or different velocity and density scalings, can easily be added to the program.

2.6 Estimation of Wind Properties

Spectral fitting using a photoionization code typically provides outputs such as the ionization parameter ξ, column density N_H, and the wind's projected velocity along the line-of-sight v_{out}. From these parameters, we can derive various physical properties like location and energetics of the wind or outflows.

The distance between the wind and the illuminating central source can be estimated in two ways. The first method is by comparing the observed outflow velocity along the line of sight to the escape velocity, i.e, $v_{esc} = \sqrt{\frac{2GM_{BH}}{r}}$ for a Keplerian

disk. The radius at which this happens gives an estimate for the minimum radius r_{min} from the source from which the outflow may have been launched. This is equal to (in the Newtonian limit):

$$r_{min} = \frac{2GM_{BH}}{v_{out}^2} = R_s \left(\frac{c}{v_{out}}\right)^2 \tag{2.30}$$

where R_s is the Schwarzschild radius. The second method to obtain the radial distance is from the definition of the ionization parameter, $\xi = \frac{L_{ion}}{N_H r^2}$, and by approximating the outflow as geometrically thin ($\Delta r/r \ll 1$), i.e., the size of the absorber does not exceed its distance to the BH, so that $N_H \approx n_0(r_1 - r_0) \approx n_0 r_0$ (Behar et al. (2003); Crenshaw and Kraemer (2012)). This gives the maximum radius r_{max} from which the outflow may have been ejected as:

$$r_{max} = \frac{L_{ion}}{\xi N_H} \tag{2.31}$$

where $r_0 < r_{max}$ (Tombesi et al. (2013)). It is also possible to constrain r from the time lag with which the UFO ionization status responds to changes in the illuminating ionising continuum (e.g. Parker et al. (2017)).

From the estimates of r, the wind energetics can be derived. The mass outflow rate $\dot{M}_{out}$ is usually expressed in solar masses per year, and represents the amount of mass transported by the wind. It is computed using the following expression derived by Krongold et al. (2007):

$$\dot{M}_{out} = f(\delta, \phi)\pi\mu r m_p N_H v_{out}, \tag{2.32}$$

where $f(\delta, \phi)$ is a geometric factor of the order of unity and depends on the angles δ and ϕ between the line of sight and the wind direction with the accretion disk plane respectively. A first-order formula for $\dot{M}_{out}$ widely adopted in the literature is given in Crenshaw and Kraemer (2012):

$$\dot{M}_{out} = 4\pi\mu r m_p N_H C_F v_{out}, \tag{2.33}$$

where C_F is the covering fraction (fraction of solid angle Ω; it ranges between $0 \leq C_F \equiv \frac{\Omega}{4\pi} \leq 1$) of the wind, m_p the proton mass, and μ is the mean atomic mass per proton ($\mu \approx 1.2$ (Gofford et al. (2015)) for fully ionized gas and solar abundances).

By considering the velocity of the outflow to be constant, any acceleration is neglected, and the mechanical or kinetic power can be derived as:

$$\dot{E}_{out} = \frac{1}{2}\dot{M}_{out}v_{out}^2, \tag{2.34}$$

and the outflow momentum rate (or force):

$$\dot{P}_{out} = \dot{M}_{out}v_{out}. \tag{2.35}$$

Another useful quantity to compare with $\dot{P}_{out}$ is the AGN radiation force or momentum rate $\dot{P}_{rad}$:

$$\dot{P}_{rad} = \frac{L_{bol}}{c}, \tag{2.36}$$

If $\dot{P}_{rad} \gtrsim \dot{P}_{out}$, then the AGN radiation alone is powerful enough to drive the observed outflow.

2.7 Launching Mechanisms for Accretion Disk Winds in AGN

The accretion disk wind dynamics can be expressed by the momentum equation for fluid (Ho and Wang (2007)) which is given as:

$$\rho\frac{D\vec{v}}{Dt} + \rho\nabla\phi = -\nabla P + \frac{1}{4\pi}(\nabla \times \vec{B}) \times \vec{B} + \rho\vec{F}^{rad} \tag{2.37}$$

$\rho, v, P, B, \phi, F^{rad}$ are respectively the wind density, velocity, pressure, magnetic field, gravitational potential and the radiation force determined by the AGN environment. For successful launch of an outflow, one or combination of the right-hand terms

should overcome gravity. Depending on the dominant term we have thermally, magnetically or radiatively-driven outflows. For both WA and UFOs, the main launching mechanism is yet to be well constrained observationally.

2.7.1 Thermal driven winds

If the accretion disk is in hydrostatic equilibrium, mass loss can occur if the upper atmosphere is subjected to heating. Significant heating can occur due to irradiation of the outer, cooler regions of the disk by intense radiation from the inner, hotter regions. Theoretical models suggest that such heating, especially from X-rays, can significantly impact the gas dynamics within the disk. X-rays can heat low density gas via Compton heating, raising the temperature to around 10^7 K (known as the Compton temperature). At such a high temperature, the upper atmosphere of the disk can either expand and form a static corona or produce a thermal wind (gas-pressure-driven wind), depending on whether the thermal velocity exceeds the local escape velocity (e.g., Begelman et al. (1983); Ostriker et al. (1991); Woods et al. (1996); Proga and Kallman (2002)).

To launch a thermal-driven wind, the gas pressure must overcome gravity, i.e., particle's speed must exceed the escape velocity

$$v_e \equiv \sqrt{\frac{2GM_{BH}}{r}} \tag{2.38}$$

where r is the radius where heating is taking place. Since escape velocity varies with radius, the impact of thermal driving also depends on the radius. Generally, thermal driving is more effective at larger radii where escape velocity is lower, such winds are expected to be responsible for the low-velocity X-ray absorption features observed in AGN spectra (Chelouche and Netzer (2005)).

Equating the thermal velocity $v_{th} \sim \sqrt{\frac{k_B T_X}{m}}$ with the escape velocity v_e, it is

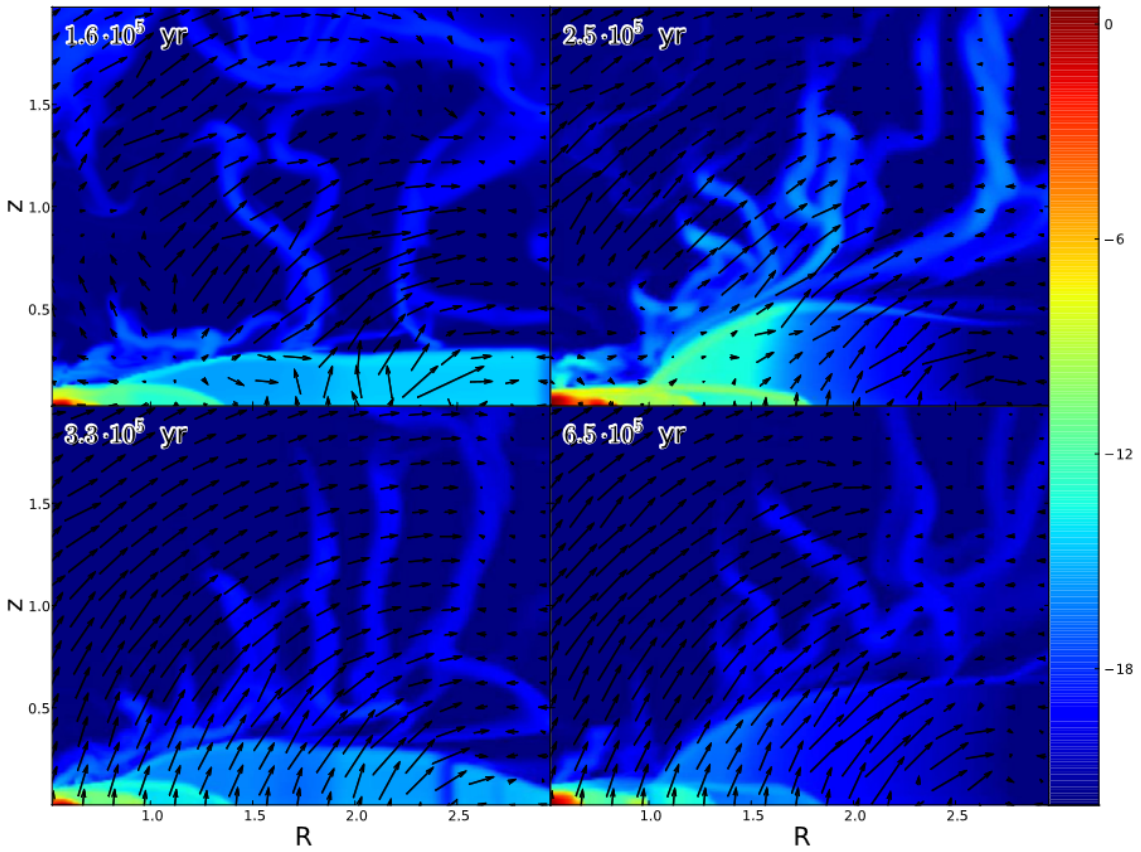

Figure 2.9: This is a 2D simulation of the evolution of a thermal wind at parsec scales performed by Dorodnitsyn and Kallman (2012). It shows a colour plot of the density log ρ in (g cm^{-3}) for a model with L = 0.5 L_{Edd}, shown at different times given in years. Axes: z: distance from the equatorial plane in parsecs; R: distance from the BH in parsecs.

possible to estimate the typical thermal launching radius:

$$R_{th} \approx \frac{GM_{BH}m}{K_B T_X} \tag{2.39}$$

where m is the average mass of particles in the gas, $k_B = 1.38 \times 10^{-16}$ erg/K is the Boltzmann constant, and T_X is the temperature of the X-ray heated gas (Ohsuga and Mineshige (2015)).

The efficiency of thermal launching of winds is primarily influenced by two factors: the temperature of the X-ray heated gas and the escape velocity of the system. Since systems with lower M_{BH} tend to have higher disk temperatures, thermal driving is generally more effective in stellar-mass systems, such as X-ray binaries ULXs (Tomaru et al. (2018); Pinto et al. (2020) and refs therein), where temperature ranges around $10^6 - 10^7$ keV. Therefore, thermal pressure can accelerate relatively slow outflows in AGN (Done et al. (2018)). But this mechanism is not enough to launch outflows in the inner accretion disk. According to this, using typical values for AGN, we get:

$$R_{th} \approx 3 \times 10^5 \left(\frac{T_X}{10^7 K}\right) R_S \tag{2.40}$$

This indicates that this process is expected to be efficient at radii approximately between the Broad Line Region and the dusty torus. The higher ionization WA component seems to be well described by a thermal wind model. According to this model, the wind is expelled from the supermassive black hole at a distance of approximately 1 pc, with an outflow velocity of about 1000 km/s (Chelouche and Netzer (2005)). For temperatures below 10^7 K, thermal driving is less significant as other forces may dominate. In particular, radiation forces can become important for gas temperatures $< 10^5$ K.

2.7.2 Radiation driven winds

Radiation pressure due to UV and X-ray absorption lines plays a crucial role in driving outflows by pushing the outer layers of the disk when the opacity of the cloud is sufficiently high (Proga and Kallman (2004)). However, for highly ionized

clouds, UV and X-ray line opacities may not be sufficient in driving the outflows. In such cases, Compton scattering can supply the additional momentum required, especially for AGN accreting close to or at the Eddington limit (King and Pounds (2003); King (2010)).

Given the immense luminosity output of AGNs, which can sometimes surpass the Eddington limit in quasars, it is the most expected mechanism for powering outflows. Thomson scattering can counteract gravity when the source is at or above the Eddington limit. However, radiation driving can be effective even at lower luminosities due to the gas opacity to resonant lines and ionization edges, a process known as "line driving." The relative strength of line-driving is quantified by the ratio between the line opacity to the electron scattering, i.e. the force multiplier M_{rad} (Castor et al. (1975)). If a gas is illuminated by UV radiation, M_{rad} can be very high, but it quickly drops to zero in presence of a strong X-ray flux, since it ionizes most of the gas elements, leading to a small number of lines available. So, the outcome of radiative driving depends on a delicate balance between the UV and X-ray luminosities.

The hydrodynamical simulations (results in Fig. 2.10) investigating radiation launching from an AGN accretion disc show that a successful wind develops in the equatorial region, where the gas is denser, colder and less photoionized (Proga et al. (2000), Proga and Kallman (2004)). M_{rad} is, therefore, high here and the outflows can reach upto velocities of 0.05c. At a distance of $\approx 300R_S$ from the axes origin, the X-ray flux is very intense. As a result, the gas is easily overionized and radiation driving alone can not accelerate the wind, leading to a stalling outflow called the "failed wind" (FW). This FW can act as a shield because of its high covering factor and density. It absorbs a significant fraction of the X-ray flux and prevents the overionization of the equatorial gas, and thereby, allowing powerful ejections in the innermost regions with velocities reaching upto 0.2c. This mechanism can successfully reproduce the velocity, distance and ionisation status of UV outflows, such as BALs and BLR outflows (Nomura et al. (2016); Giustini and Proga (2019)).

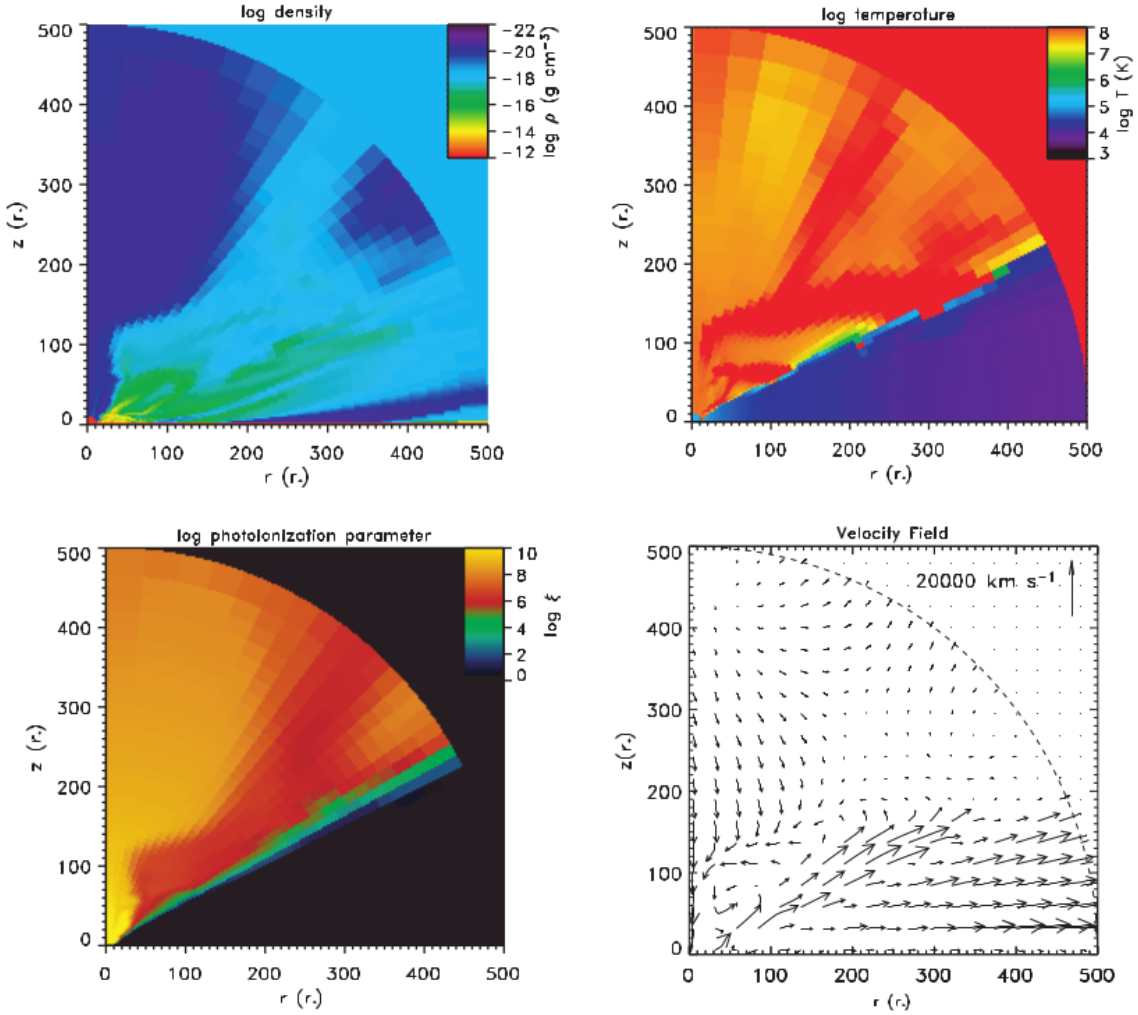

Figure 2.10: Physical structure of the Proga and Kallman (2004) accretion disc wind model. The four panels from top left to bottom right indicate the color-coded maps of the gas density, temperature, photoionization parameter and velocity field (poloidal component only). In all panels the rotation axis of the disk is along the left-hand vertical frame and the midplane of the disk is along the lower horizontal frame.

However, the introduction of compton scattering poses a significant challenge to the FW shielding because scattered photons can "circumvent" the FW region and ionize gas at higher radii by their "random walk" effect, as demonstrated in Higginbottom et al. (2014). This indicates that radiative driving is effective only at sufficiently large distances from the X-ray corona, such as at BLR-like distances. These are farther than the typical UFO launching sites ($\sim 100R_S$).

A study on thermal stability of radiation-pressure-driven winds in ultra-luminous X- ray sources (ULXs) (Pinto et al. (2020)) found that at super-Eddington luminosity, the radiation pressure might inflate the accretion disk and drive fast winds at a fraction of the speed of light. These winds remain in stable thermal equilibrium. The research confirms that radiation pressure is indeed effective in driving high-velocity winds.

2.7.3 Magnetically driven winds

Magnetic driving is most likely a predominant mechanism for launching of winds or outflows. No special conditions are required for the occurrence of this type of wind, only the presence of magnetic fields. Given the presence of high-ionization and high-temperature plasma in AGN, magnetic fields are probably ubiquitous in the innermost part of accretion discs. The magnetorotational instability (MRI) (Balbus and Hawley (1991)) is a very robust and universal mechanism to produce turbulence and transport angular momentum in disks at all radii (Balbus and Hawley (1998); Ji et al. (2006)). So, there is a possibility that magnetic fields control mass accretion inside the disk and play a key role in producing a mass outflow from the disk.

There are two types of magnetically driven winds: (a) magnetocentrifugal winds where the dominant contribution to the Lorentz force is the magnetic tension, and (b) magnetic pressure driven winds where the dominant contribution to the Lorentz force is the magnetic pressure.

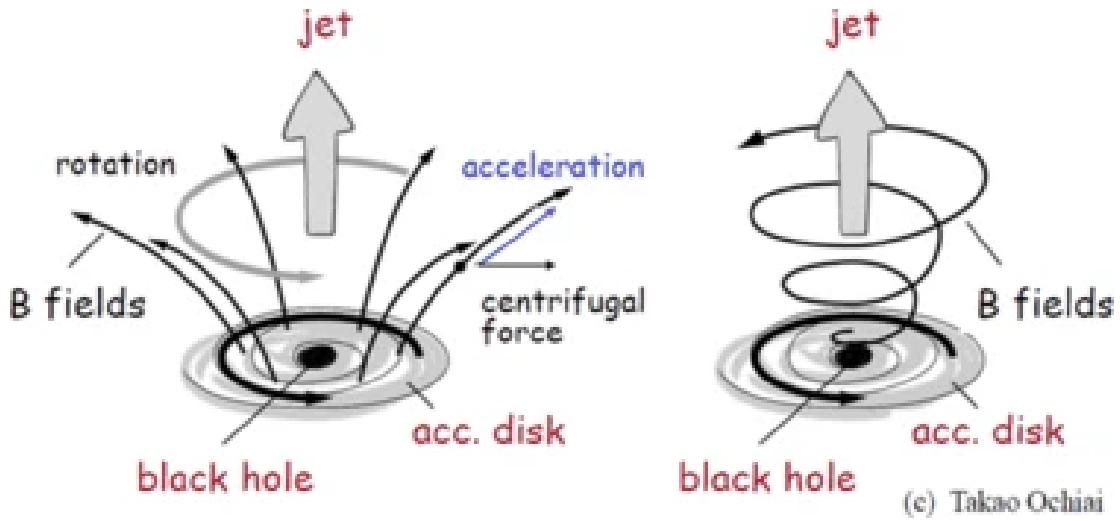

Figure 2.11: Left panel: poloidal component B_p. Right panel: toroidal component B_ϕ (Ohsuga and Mineshige (2015)).

A large-scale, ordered magnetic field that is anchored to and co-rotates with the accretion disk can effectively channel a mass outflow from the disk. Usually the rotational velocity of the disk is proportional to the Keplerian velocity, $v_{rot} \propto v_{kep} = \sqrt{\frac{1}{R_0}}$, where $\mathrm{v_{rot}}$ and $\mathrm{R_0}$ are in units of the speed of light and gravitational radii, respectively. As a result, a co-moving magnetic field can easily reach relativistic velocities, and the gas carried along with it is protected from overionization or inadequate radiation drag. The magnetic field is generally assumed to be axisymmetric, with both poloidal and toroidal components, Bp and B_ϕ (Fig. 2.11).

Blandford and Payne (1982) were the first to introduce the concept of magneto-hydrodynamical (MHD) outflows. They suggested that a centrifugally driven wind could emerge from a Keplerian accretion disk if the poloidal component of magnetic field lines make an angle of less than 60 degrees with the disk surface (refer to Fig. 2.11). At larger angles, centrifugal forces become insufficient to drive outflows. Due to the field co-rotation with the disk, the fluid conserves its specific angular velocity. The constraint on the line inclination ensures they provide enough centrifugal acceleration to the fluid, driving it at higher radii, where the corresponding rotational velocity is now smaller than the angular velocity. Consequently, the fluid is pushed outward, giving rise to an outflow. In this case, the gas acceleration is due to the

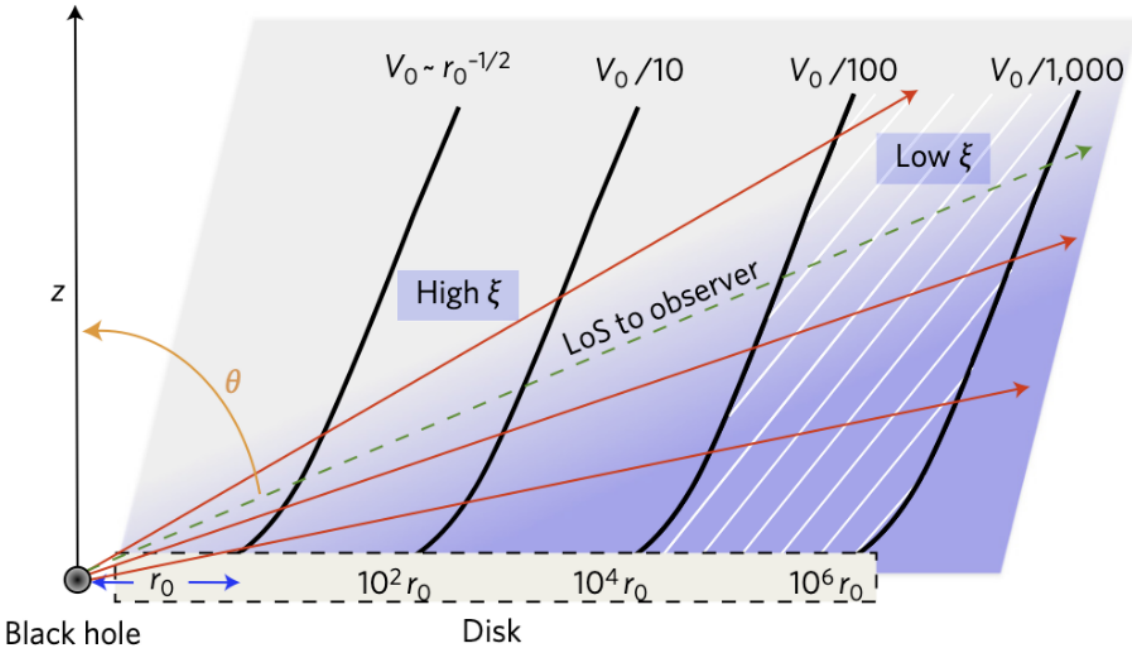

Figure 2.12: Schematic of MHD accretion disk wind. Poloidal 2D wind streamlines (thick solid grey lines), the decreasing velocity ($V_0 \sim c$) and ionization (ξ) with radius is illustrated ($r_0 \sim R_S$). The hatched region represents the absorbing region wind with velocity $v_{wind} \sim 100 - 1000$ km/s. Taken from Fukumura et al. (2017).

magnetic tension. An alternate theory was explored by Uchida and Shibata (1985), who used MHD simulations to demonstrate magnetic-pressure driven jets. Recent simulations, such as those by Kato et al. (2004), have confirmed these ideas, showing the formation of magnetic-tower structures resulting in jets and outflows driven by magnetic pressure force.

Magnetic wind models are built by solving the Grad-Shafranov equation, from which the wind density, momentum and energy can be derived (Fig. 2.13) (Fukumura et al. (2010), Fukumura et al. (2013); Kazanas et al. (2012)) by considering some initial conditions and assumptions, such as perfect MHD, axis-symmetry and self-similarity. These models have been successfully applied to UFOs in powerful quasars (Fukumura et al. (2015), Fukumura et al. (2018a)). Magnetic field strength increases with decrease in r, therefore, the fastest outflows must be accelerated in the innermost regions, with velocities reaching upto $v_{out} \sim 0.2$ - 0.3c. UFOs are, therefore, identified by the innermost layers of gas, launched at small radii from the SMBH as required by their fast velocities. Another interesting feature of MHD

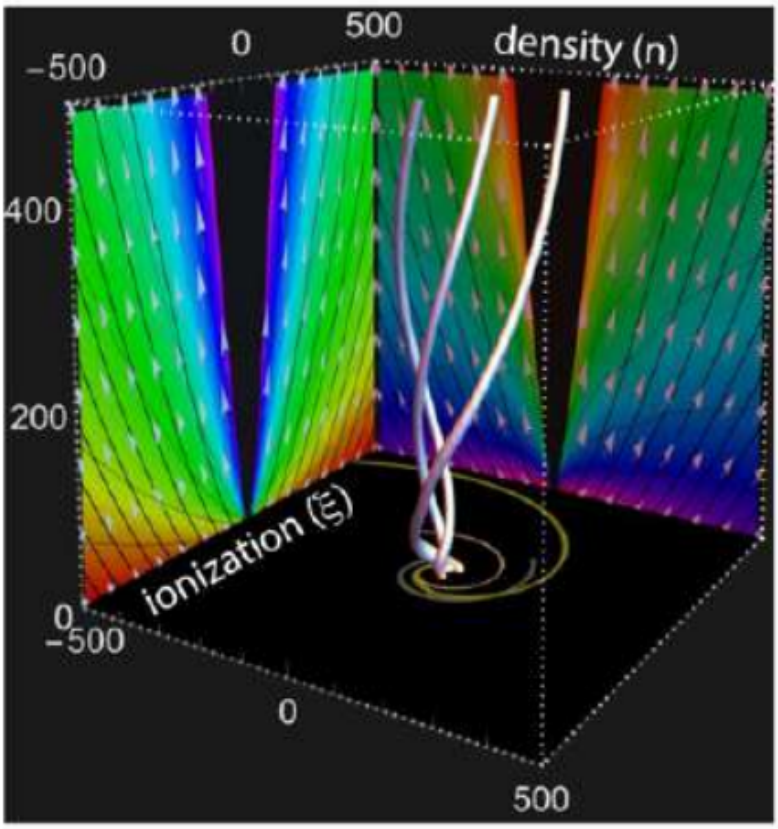

Figure 2.13: Magnetic wind structure in 3D (white lines). The left and right walls show the ionization parameter and the density of the wind, respectively. Blue(red) corresponds to higher(lower) values. Taken from Fukumura et al. (2018a)

models is that WAs can also fit in this picture as UFO's high-distance, low-density and low-velocity counterparts. Furthermore, an MHD wind is insensitive to the ionization level.

Chapter 3

The XMM-Newton Observatory

The X-ray Multi-Mirror Mission (XMM-Newton), also known as the High Throughput X-ray Spectroscopy Mission, is an X-ray space observatory that was launched by the European Space Agency in December 1999 on an Ariane 5 rocket. The main objective of this mission was to investigate X-ray sources, perform narrow and broad range spectroscopy, and carry out the first simultaneous imaging of objects in both X-ray and optical (visible and ultraviolet) wavelengths. A schematic picture of XMM-Newton is given in Fig. 3.1. The satellite is equipped with three co-aligned telescopes focusing the photons to three independent instruments. The mechanism of collecting and focusing of X-rays is based on the principle of grazing incidence.

3.1 Instruments

3.1.1 European Photon Imaging Cameras

The European Photon Imaging Camera (EPIC) consists of three imaging spectrometers, two Metal Oxide Semiconductor (MOS) CCD arrays and one pn CCD array, each positioned at the focus of one of the three coaligned X-ray telescopes. Two of the cameras utilize an array of seven EPIC-MOS type Charge-Coupled Devices (CCDs) (Turner et al. 2001) and share their optical paths with the RGS (Den Herder et al. (2001)). This arrangement allows about 44% of the original incident flux to reach the EPIC-MOS cameras. The third camera employs a monolithic pn-CCD

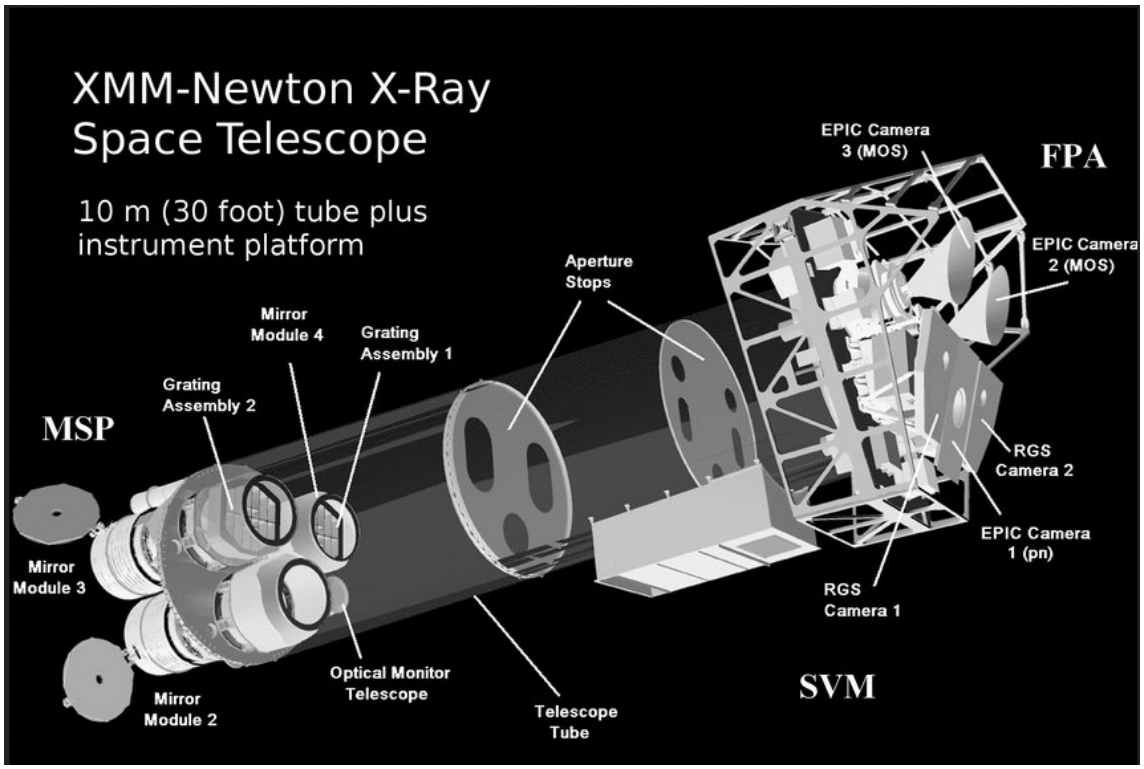

Figure 3.1: View of the XMM-Newton spacecraft subsystems (Credit: ESA/XMM-Newton). It has four main components: (a) the Mirror Support Platform (MSP) which supports the telescope assemblies along with the grating systems and the OM; (b) the Service Module (SVM) carrying spacecraft support systems; (c) the Focal Plane Assembly (FPA) which supports the platform carrying focal plane instruments; (d) the Telescope Tube which is a hollow carbon fibre that maintains the FPA and the MSP separation. From Lumb et al. (2012).

array (Strüder et al. (2001)) and is located at the focus of an unobstructed X-ray telescope. Each EPIC instrument includes an identical filter wheel with various X-ray transmissive but optical light blocking filters. It also contains the Radiation Monitoring System to detect the ambient electron and proton fluxes. It is used as part of the warning system to protect the cameras from harmful radiation levels.

The EPIC enables highly sensitive imaging observations across a circular field of view (FOV) of 30 arcminutes in diameter in the energy range of 0.15 - 15 keV. It has a moderate spectral resolution of $E/\Delta E \sim 20 - 50$ and angular resolution of 6" FWHM point spread function (PSF). Each camera can operate with a time resolution as fast as 7 µs.

The two MOS-CCD cameras are used for detecting low-energy X-rays. Each EPIC-MOS camera features seven front-illuminated CCDs as illustrated in Fig. 3.2. These are three-phase frame transfer devices made of high resistivity epitaxial silicon with an open-electrode structure. The central CCD is at the telescope focus and the six outer CCDs are stepped towards the mirror to approximate the focal plane curvature for better off-axis focus. The CCD imaging area is 2.5×2.5 cm with 600×600, 40 micron square pixels. Each pixel covers 1.1×1.1 arcseconds of the FOV, with 15 pixels covering the mirror PSF half-energy width of 15". The seven CCDs cover a focal plane of 62 mm, which is equivalent to 28.4' in diameter. The two EPIC-MOS cameras are arranged orthogonally on the spacecraft to ensure that the gaps in sky coverage between the outer CCDs of one unit are covered by the other. The EPIC cameras allow several data acquisition modes to accommodate a range of source fluxes and to allow for fast-timing measurements. The modes can be applied to the central CCD of EPIC-MOS as described in Table 3.1.

The EPIC-pn detector was designed specifically for the XMM-Newton X-ray telescope, optimizing angular resolution, field of view (FOV), and energy pass band. The pn-CCD camera is used for detecting high-energy X-rays. The camera array comprises of 12 independently operated 3×1 cm back-illuminated pn-CCDs, mono-

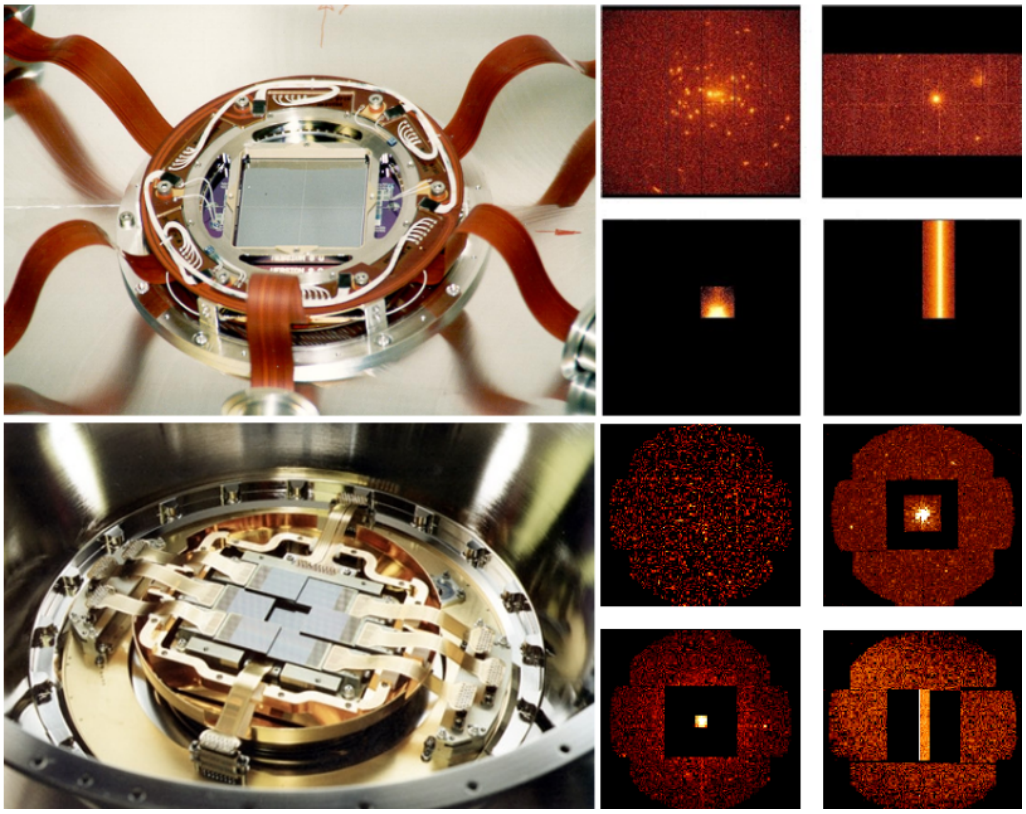

Figure 3.2: Images of the CCD detectors EPIC-pn (top) and EPIC-MOS (bottom) as well as examples of the FOVs using the different observation modes - Full Frame, Large Window, Small Window, and Timing. From Schartel et al. (2024).

Central CCD Mode	**Imaging Area (Pixels)**	**Time Resolution (s)**	**Max. Point Source Count Rate (flux) (s^{-1})**
FULL FRAME	600×600	2.6	0.5
LARGE WINDOW	300×300	0.9	1.5
SMALL WINDOW	100×100	0.3	4.5
TIMING	100×600	$\sim 10^{-3}$	100

Table 3.1: Summary of the basic characteristics of the EPIC-MOS CCDs science modes (Schartel et al. (2024), Lumb et al. (2012)).

Central CCD Mode	**Imaging Area (Pixels)**	**Time Resolution (ms)**	**Max. Point Source Count Rate (flux) (s^{-1})**
FULL FRAME	376×384	73.4	2
EXTENDED FULL FRAME	376×384	199.1	0.7
LARGE WINDOW	198×384	47.7	3
SMALL WINDOW	63×64	5.7	25
TIMING	64×200	0.03	800
BURST	64×180	7 µs	60,000

Table 3.2: Summary of the basic characteristics of the EPIC-pn CCDs science modes (Schartel et al. (2024), Lumb et al. (2012)).

lithically implanted on a single wafer (Fig. 3.2). The instrument is divided into four quadrants, each with three pn-CCD subunits of 200×64 pixels operated in parallel. The 6×6 cm imaging area covers about 97% of the telescope's FOV, with around 6 cm^2 outside the FOV for background studies. The CCD pixel size is 150×150 microns (4.1"), providing a position resolution of 120 microns and an equivalent angular resolving capability for a single photon of 3.3". The focal point of the X-ray telescope is located on CCD 0 of quadrant 1. A summary of the basic characteristics of the science modes is given in Table 3.2.

3.1.2 Reflection Grating Spectrometers

There are two identical Reflection Grating Spectrometers (RGS) present in XMM-Newton, located behind two of its three nested sets of Wolter I type mirrors. RGS are made of two Focal Plane Cameras along with their associated Reflection Grating

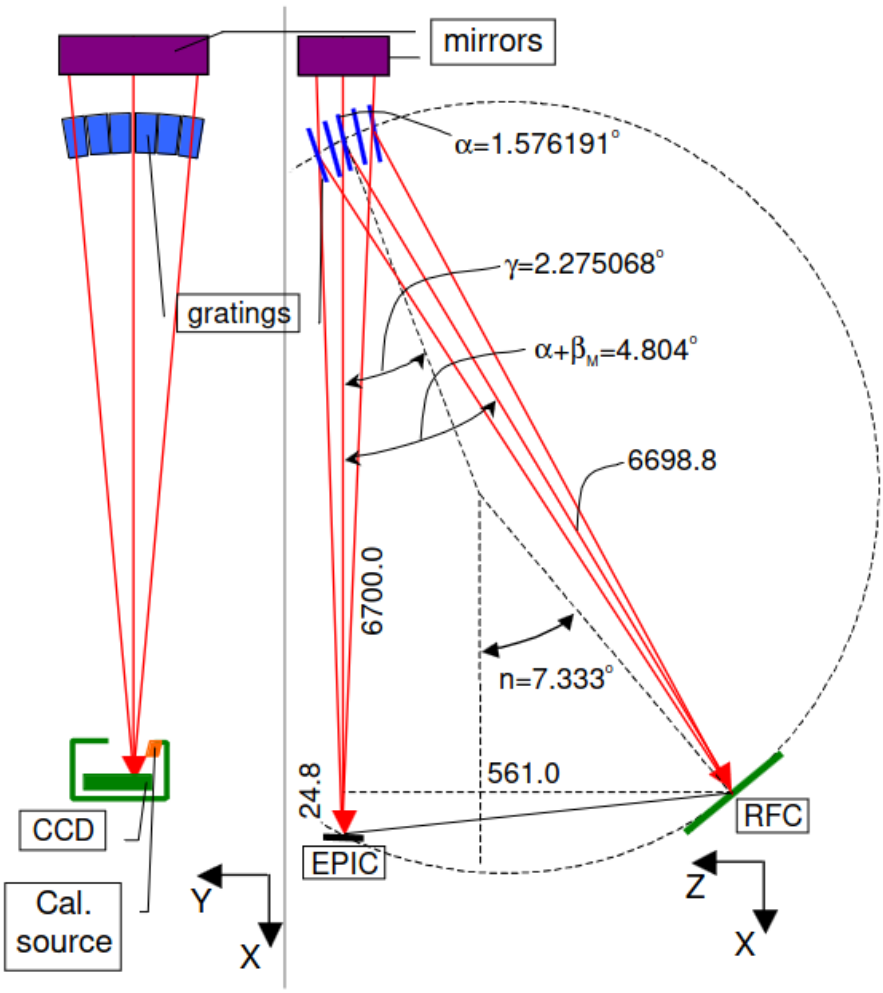

Figure 3.3: Optical design of the RGS (not to scale). X-rays, indicated by red arrows, enter from the top. Numerical values for a few key dimensions and angles are indicated (linear dimensions in mm, angles in degrees) (Den Herder et al. (2001)).

Arrays (RGA). This system is used to generate X-ray spectral data. It can identify the elements present in the target source, as well as determine their temperature, quantity, and other characteristics. It operates in the 2.5 to 0.35 keV range, allowing high resolution (E/ΔE = 100 to 500) measurements in the soft X-ray range. This permits detection of the K-shell transitions of carbon, nitrogen, oxygen, neon, magnesium, silicon and the L shell transitions of iron (Den Herder et al. (2001), Brinkman et al. (1996)). It has a maximum effective area of about 140 cm^2 at 15$\mathring{A}$. The RGS design is illustrated in Fig. 3.3.

Each Focal Plane Cameras consist of nine MOS-CCD devices that are mounted

in a row and follow a curve called the Rowland circle. Each CCD contains 384×1024 pixels, with a total resolution of more than 3.5 megapixels. The total length and width of the CCD array is dictated by the wavelength range and the size of the RGS spectrum respectively. Each array is surrounded by a massive wall to provide heat conduction and radiation shielding.

The RGAs are mounted on two of the primary telescopes. They allow approximately 50% of the incoming X-rays to pass directly to the EPIC system and redirects the rest 50% onto the Focal Plane Cameras. RGA1 contains 182 identical gratings, while RGA2 has 181 gratings since it lost one due to fabrication error. The telescope mirrors focus the X-rays at the focal point, giving each grating the same angle of incidence, and conforming to a Rowland circle to minimize focal aberrations. Each grating, measuring 10×20 cm, is made of 1 mm thick silicon carbide substrate. This is covered with a 2000 $\mathring{A}$ gold film, and is supported by five beryllium stiffeners. The gratings have an average of 646 grooves per millimeter for X-ray deflection.

3.1.3 Optical Monitor

The Optical Monitor (OM) is a 2 m long, 30 cm diameter Ritchey-Chrétien optical/ultraviolet telescope. It offers simultaneous optical/UV coverage of sources in the EPIC field of view. This extended the mission's wavelength range and increased its scientific return. The OM is sensitive in the wavelength range 170 to 650 nanometres in a 17×17 arcminute square FOV, co-aligned with the centre of the X-ray telescope's FOV. It's focal length is 3.8 m and a focal ratio of $f/12.7$ (Mason et al. (2001)). Its photon-counting capability and low in-space background make it highly sensitive for detecting faint sources, reaching about magnitude 22 (5σ detection) in the B filter with a 5 ks exposure. The UV and optical grisms allow low-resolution spectroscopic analysis, and the fast mode timing options permit detailed studies of temporal variability.

The instrument consists of the Telescope Module, composed of the optics, detectors, processing equipment, and power supply (Fig. 3.4). The Digital Electronics

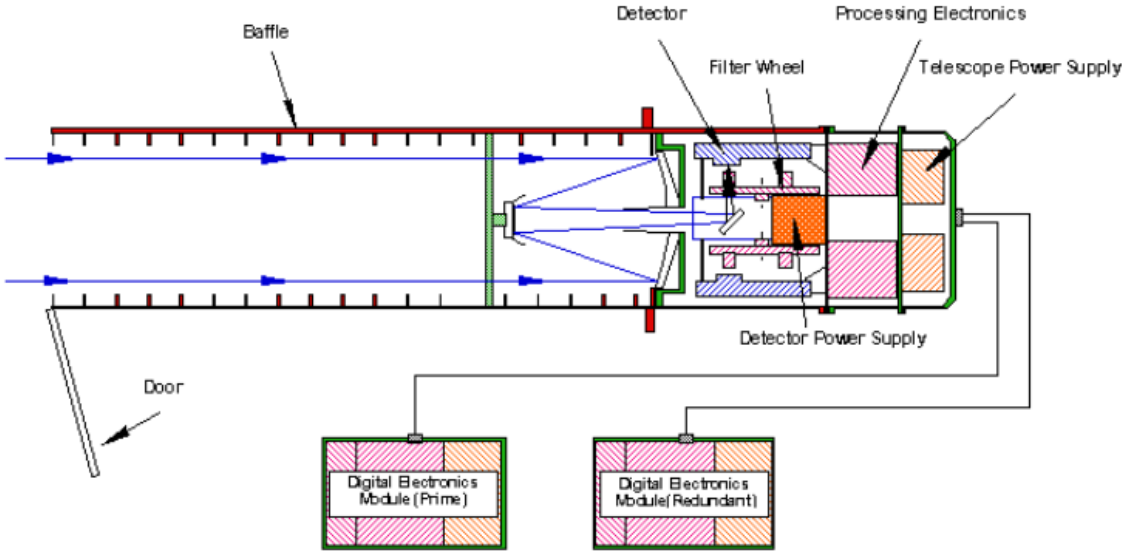

Figure 3.4: Schematic of the Optical Monitor. From Schartel et al. (2024).

Module contains the instrument's control unit and data processing units. The incoming light is focused on one of two detector systems. This light first passes through an 11-position filter wheel which consists of one opaque filter to block light, six broad band filters, one white light filter, one magnifier, and two grisms. It then goes through an intensifier which amplifies the light by one million times, then falls onto the CCD sensor. The CCD is of 384×288 pixels, of which 256×256 pixels are used for observations. Each pixel is further subdivided into 8×8 pixels, resulting in a final product that is 2048×2048 pixels in size.

3.2 Telescopes

There are three telescopes feeding the EPIC and RGS systems. They were designed to direct the X-rays into the spacecraft's primary instruments. Each of them consist of the following elements (Lumb et al. (2012)) as shown in Fig. 3.5:

- Mirror Assembly Door - protects the X-ray optics and interior of the telescope against contamination until operation begins.

- Entrance Baffle - ensures effective suppression of visible stray light.

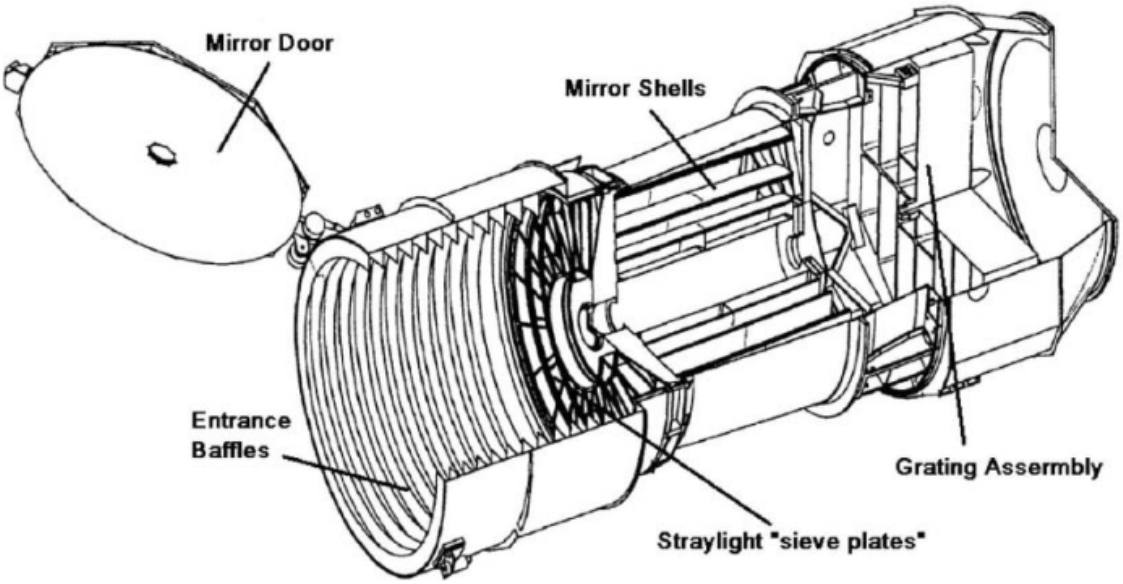

Figure 3.5: XMM-Newton Telescope configuration (Lumb et al. (2012)).

- X-ray Baffle (XRB) - blocks X-rays coming from outside the nominal field of view.

- Mirror Module (MM) - includes the X-ray optics.

- Electron Deflector - produces a toroidal magnetic field to divert soft electrons, located behind the mirrors in the shadow of the MM spider.

- Reflection Grating Assembly (RGA) - deflects half of the X-ray light to a strip of CCD detectors (RGS), offset from the focal plane. It has a mass of 60 kg and is present on the backside of two of the three MMs.

- Exit Baffle - provides a thermal environment for the gratings.

Each of the telescope assemblies have a diameter of 90 cm, are 250 cm in length, with a base weight of 425 kg. The two telescopes with RGA has an additional weight of 20 kg. Each individual telescope is made of 58 cylindrical, nested Wolter Type-1 mirrors. Each of these mirrors are 600 mm long with a diameter ranging from 306 to 700 mm, which gives a total collecting area of 4425 cm^2 at 1.5 keV and 1740 cm^2 at 8 keV. The MM have a focal length of 7.5 metres and with a resolution of $\sim$ 15 arcsec (on-axis Half Energy Width). The mirrors were built by vapour-depositing a

250 nm layer of gold reflecting surface onto a highly polished aluminium mandrel. This was followed by electroforming a monolithic nickel support layer onto the gold.

Chapter 4

Data Analysis of IRAS 13224-3809

4.1 The source: IRAS 13224-3809

IRAS 13224-3809 is a bright narrow line Seyfert-1 (NLSy1) galaxy located about 1 billion light-years away from Earth at a cosmological redshift z = 0.0658 (Allen et al. (1991)). It is present in the Centaurus constellation and hosts a relatively low mass supermassive black hole of mass M = $10^6 - 10^7 M_\odot$ (Zhou and Wang (2004)). It is a radio-quiet source (Boiler et al. (1997)), with no evident jet emission observed yet.

IRAS 13224-3809 has been studied in multiple bands (for e.g., radio (Boiler et al. (1997)), UV (Rodriguez-Pascual et al. (1997)), optical (Young et al. (1999)), X-ray (Gallo et al. (2004), Fabian et al. (2013))) previously. It has been observed during 16 observations (∼130 ks per observation) with the XMM-Newton of ESA, totaling to 2 mega-seconds of exposure between 2002 and 2016. It has an apparent optical magnitude of $m_B \sim 16.6$ in Johnson B band and a X-ray flux value of $F_X \sim 6 \times 10^{-13}$ erg cm^{-2} s^{-1} in the photon energy range E = 2 - 10 keV. This active galactic nucleus (AGN) exhibits remarkable X-ray variability, fluctuating by up to a factor of 10 within just 500 seconds across the energy range E = 0.3 - 10 keV (Alston et al. (2019)). It is known to be the most variable AGN in the X-ray band (Ponti et al. (2012)) with the flux changing by up to two orders of magnitude in only a few hours (see Fig. 4.1). Due to its rapid and extreme X-ray variability,

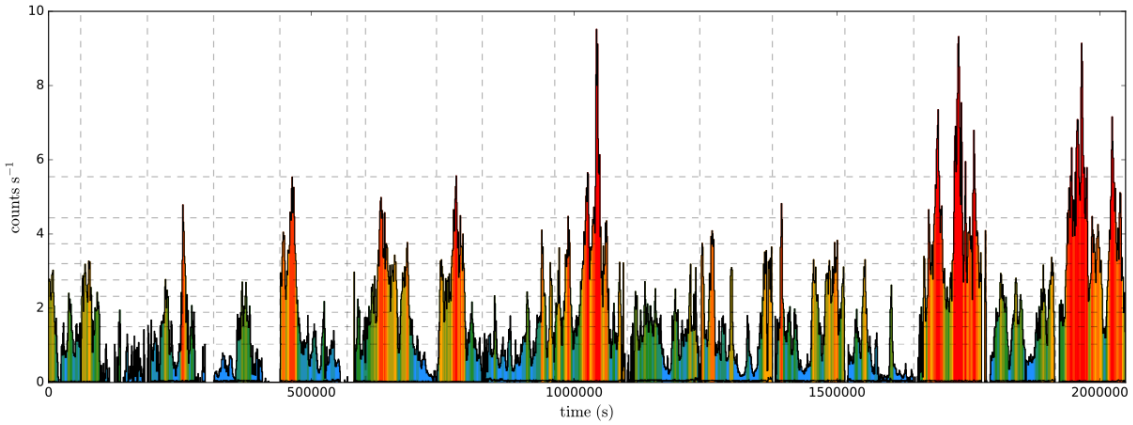

Figure 4.1: EPIC-pn light curve of all the observations in the 0.3-10.0 keV energy range. The vertical lines indicate the start and the end of each observation. The horizontal lines and the colours show the thresholds of the flux intervals. Flux thresholds for 10 flux regimes were chosen in order have comparable statistics. Time gaps between the observations are not shown. Taken from Pinto et al. (2018).

the X-rays are thought to emerge from a region within a few tens of gravitational radii. Variability in the optical band is not significantly rapid; a variability of 24% in 3 years has been reported in the UV continuum (Rodriguez-Pascual et al. (1997)).

Being a NLSy1 AGN, the mass accretion rate of the black hole is very high - of the order of Eddington accretion rate:

$$\dot{M} \sim \dot{M}_{Edd}$$

As a result of these extreme accretion rates, highly ionized winds at nearly relativistic speeds have been detected from this source that are driven by the accretion flow (Parker et al. (2017), Pinto et al. (2018), Chartas and Canas (2018), and Midooka et al. (2023)).

IRAS 13224-3809 was observed by the XMM-Newton satellite in 2002 and 2011, revealing a steep X-ray spectrum with Γ = 2.5 - 2.7 (Fabian et al. (2013)) and a significant soft excess below 1.5 keV and a sharp drop around 8 keV. Strong Fe K and Fe L emission lines in the spectrum suggested relativistic reflection off the inner accretion disk around a rapidly rotating black hole ($a^* = 0.988 \pm 0.001$; Fabian et al. (2013)). Fitting with this relativistic reflection model required an iron overabundance by a factor of 3–20 (Fabian et al. (2013); Chiang et al. (2015)) to account for

the energy spectra of various objects. Analysis of the 2011 data indicates the corona is located within a few gravitational radii. Chiang et al. (2015) fitted the soft excess in the EPIC spectra with a combination of the reflection model `reflionx` (Ross and Fabian (2005)) and a blackbody. Recently, Jiang et al. (2022) found the iron abundance to be $Z_{Fe} = 3.2 \pm 0.5$ on assuming a high-density disk reflection of 10^{20} cm^{-3}. The relativistic reflection model and the partial absorption model can not often be distinguished in shape in the X-ray spectra of AGNs (Parker et al. (2022)). Yamasaki et al. (2016) successfully explained the spectral variability of this source with the 2002–2011 XMM-Newton data using the partial absorption model without the above mentioned extreme conditions.

IRAS 13224-3809 was also recently observed with a XMM-Newton quasi-simultaneous 1.5 Ms and NuSTAR (Nuclear Spectroscopic Telescope Array) observing campaign in 2016. Parker et al. (2017) discovered a series of strongly blueshifted (v = 0.236 ± 0.006 c) absorption lines from O, Ne, and Fe in the EPIC-pn and RGS spectra that indicates the presence of an ultra-fast outflow. They found that these features were strongly dependent on the source flux, varying on time-scales as short as a few kilo-seconds. They also reported the presence of the Mg XII, Si XIV, S XVI, Ar XVIII, and Ca XX Ly α lines in the variability spectra. They reported an anti-correlation between the equivalent width of the UFO absorption lines and the X-ray luminosity. The weakening of the iron lines with increasing X-ray luminosity indicates over-ionization of the gas. Pinto et al. (2018)) found the line-of-sight velocity of the UFO to be correlated with the X-ray luminosity. It is often assumed that winds in high accretion systems are mainly radiation-driven, but this is highly debated.

4.2 XSPEC

The XSPEC (X-ray Spectral Fitting Package) software was used here to carry out the fitting procedure. It is a software tool used for analyzing the spectra of astronomical X-ray sources like black holes, active galactic nuclei, etc. XSPEC is a

command-driven, interactive, spectral-fitting program and is independent of the detector or instrument used to obtain the spectral data. It can, therefore, be used for any spectrometer. It was developed by NASA and included in the `Heasoft` package. XSPEC allows researchers to fit theoretical models to observed data, thereby enabling the interpretation of the physical properties and processes occurring in various astrophysical objects. It supports a variety of models, including thermal and non-thermal emission, absorption, and reflection, and provides tools for complex statistical analysis and parameter estimation, making it essential for high-energy astrophysics research. In this work we used the XSPEC version `XSPECv12.14.0b`. The details about different models and their parameters are given in XSPEC MANUAL.

4.3 Data Reduction

The reduction of the raw data (P. Condò et al. in preparation) was done with the SAS pipeline to extract and generate an event file. SAS is the ESA's software for the XMM-Newton data reduction and product extraction. The data was examined for the presence of soft-proton flares as that might affect the observation, and those spikes were removed by selecting intervals devoid of flares in each observation. It was then checked for pile-up using the provided SAS tools and no significant pile-up was found for the observations. Subsequent steps included source and background selection, extraction of spectra and light curves for both the source and the background, and the combination of cleaned spectra to obtain the average spectrum utilized in this analysis.

4.4 Data Analysis

We performed here a time averaged X-ray spectral analysis of IRAS 13224-3809 by using XMM-Newton observations of 2016 using XSPEC. We started the analysis by trying to model the continuum in EPIC-pn exposures. Since, the X-ray spectrum of the IRAS 13224-3809 is very complex, along with the NuSTAR data being of low quality and the UV data not being well-sampled (only one photometric point), we

used the stacked data of the EPIC-pn CCD to study the average behaviour of this source.

The energy axes shown in the plots are not corrected for redshift since the cosmological redshift value (z = 0.0658) is very small, so the energy of the X-rays emitted at the source (rest-frame) does not change much from the observer's frame. To see the redshift-corrected spectra we need to multiply the energy axis by $(1 + z)$:

$$E_{emit} = (1 + z)E_{obs}. \tag{4.1}$$

Since our source is at redshift z=0.0658, it is closer to us and lies in our local universe. So, we anticipate minimal absorption within its host galaxy. Consequently, the primary contribution to the neutral hydrogen column density is due to local absorption in our own galaxy. So we used the `TBabs` model to account for the Galactic extinction of X-rays. `TBabs` is the Tuebingen-Boulder ISM absorption model. It is a multiplicative model in XSPEC. This model computes the cross section for X-ray absorption by the ISM as the sum of the cross sections for X-ray absorption due to the gas-phase ISM, the grain-phase ISM, and the molecules in the ISM. The value for the hydrogen column density N_H is taken from the HI4PI CollaborationHI4PI Collaboration: et al. (2016). Along the line of sight of the source, its value is:

$$N_H = 4.76 \times 10^{20} \text{ cm}^{-2}$$

.

4.4.1 Absorbed power law model

We start the analysis by applying a simple absorbed power-law model to the spectrum in the energy range E = 0.3 − 10.0 keV. We use the `zpowerlw` command which is a additive model component in XSPEC. It is a simple photon power law that takes into account the redshit of the galaxy and follows the expression $A(E) = K[E(1 + z)]^{-\Gamma}$ where z is the redshift, Γ is the photon index indicating the slope of the power-law and K is the normalization constant. The power-law model is

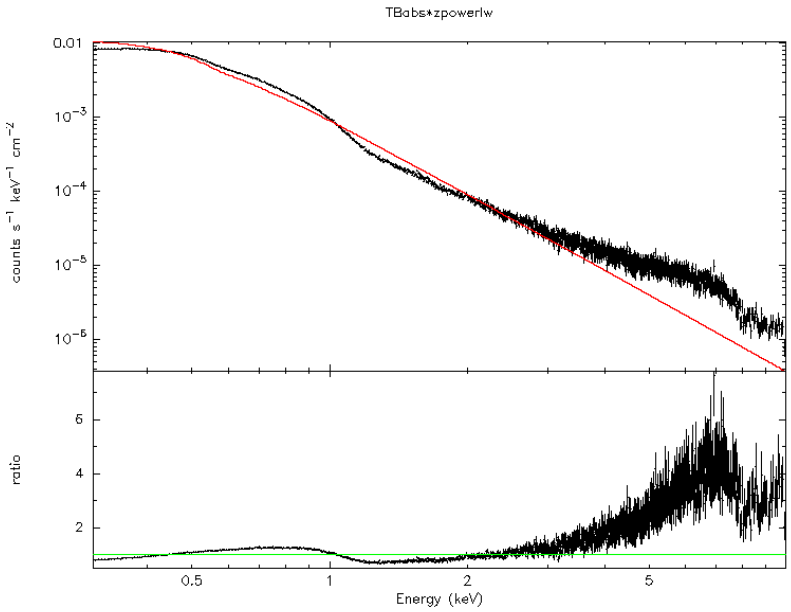

Figure 4.2: Best-fit with the model `TBabs(zpowerlw)` (χ^2/d.o.f = 66203/1295).

a mathematical tool to model the X-ray "primary continuum" resulting from high-energy processes near the SMBH, like the inverse Compton scattering occuring in the corona of the AGN. Fitting the data with this model gives a very high value for the photon index $\Gamma \sim 3.5$. We can also see from the plot (Fig. 4.2) and the fit statistic (χ^2/d.o.f = 66203/1295) that a simple power law is not enough to model both the soft ($E \approx 0.3 - 2$ keV) and the hard ($E \approx 2 - 10$ keV) spectra. We can see the presence of soft-excess below $E < 1$ keV in the spectrum.

Next we tried to model the soft excess feature of the spectrum by adding a black body component `zbbody` to the absorbed power law. It is also an additive model component in XSPEC and follows the expression:

$$A(E) = \frac{K \times 8.0525[E(1+z)]^2 dE}{(1+z)(kT)^4[exp[E(1+z)/kT] - 1]}$$

where kT is the temperature, z is the redshift and K is the normalization constant. This total model can be described in XSPEC as:

$$\texttt{TBabs} * (\texttt{zbbody} + \texttt{zpowerlw})$$

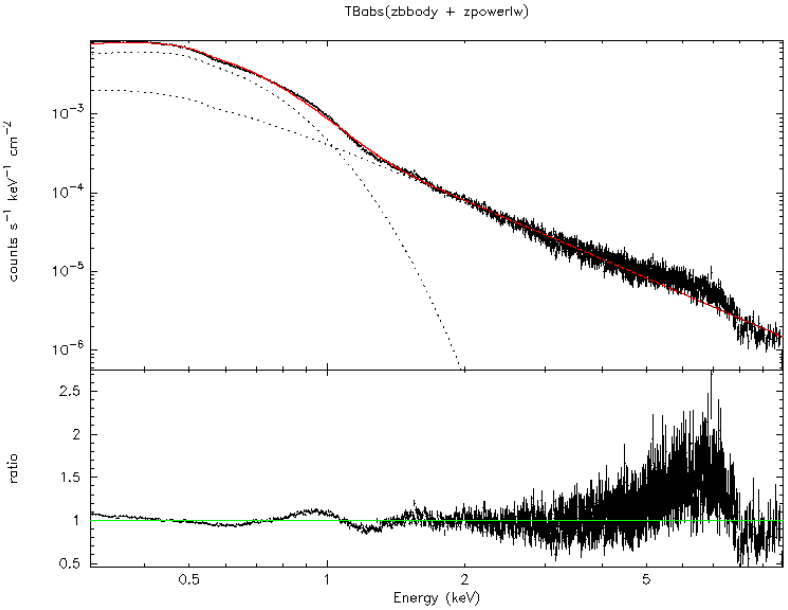

Figure 4.3: Best-fit with the model `TBabs(zbbody + zpowerlw)` (χ^2/d.o.f = 6243/1293).

. But, this model also proves to be inadequate for fitting the average data. Fitting the data with this model results in the blackbody temperature to be around kT$\sim$ 0.126 keV and the photon index of the power law model $\Gamma \sim 2.52$. The best fit gives a fit statistic of χ^2/d.o.f = 6243/1293 $\sim$ 4.8 (Fig. 4.3) which is very high.

Since one black body component could not adequately model the soft excess, we introduced a second black-body component. This adjustment significantly improved the fit, but we still did not achieve a satisfactory continuum model (χ^2/d.o.f = 4099/1291 $\sim$ 3.2).

From the residuals of this test (Fig. 4.4) a Gaussian-like feature is visible around E $\sim$ 1 keV. This is followed by a dip at slightly higher energies. We added a broad Gaussian emission component `zgauss` to model this feature. This represents a simple Gaussian line profile and is also treated as an additive model component in XSPEC, following the expression:

$$A(E) = K \frac{1}{(1+z)\sigma\sqrt{2\pi}(1 - erf(-E_l/(\sqrt{2}\sigma)))} \exp\left(\frac{-(E(1+z) - E_l)^2}{2\sigma^2}\right)$$

Component	Parameter	Value	Description (Unit)
`zbbody`	`kT`	0.054	Blackbody temperature (keV)
`zbbody`	`norm`	5.97×10^{-5}	Blackbody normalization
`zbbody`	`kT`	0.1332	Blackbody temperature (keV)
`zbbody`	`norm`	6.86×10^{-5}	Blackbody normalization
`zpowerlw`	`PhoIndex`	2.354	Photon index
`zpowerlw`	`norm`	4.68×10^{-4}	Power law normalization

Table 4.1: Best-fit parameters for the `TBabs(zbbody + zbbody + zpowerlw)` model tested on the averaged EPIC-pn data in the energy range E = $0.3 - 10.0$ keV with fit statistic χ^2/d.o.f = 4099/1291 $\sim$ 3.2. This value is greater than the maximum value of reduced chi-squared supported by XSPEC for calculating errors.

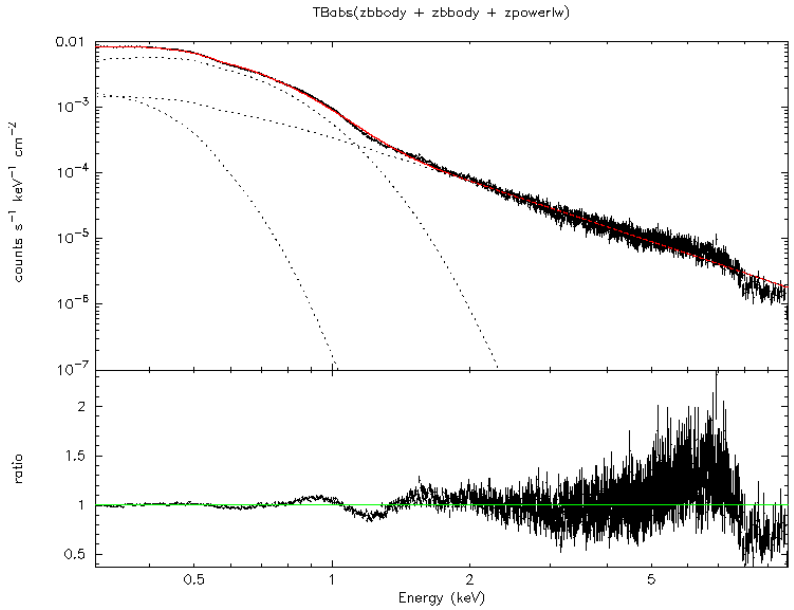

Figure 4.4: Best-fit with the model `TBabs(zbbody + zbbody + zpowerlw)` (χ^2/d.o.f = 4099/1291).

Component	Parameter	Value	Description (Unit)
zbbody	kT	0.1151 ± 0.0005	Blackbody temperature (keV)
zbbody	norm	$(6.46 \pm 0.06) \times 10^{-5}$	Blackbody normalization
zbbody	kT	1.71 ± 0.03	Blackbody temperature (keV)
zbbody	norm	$(2.94 \pm 0.11) \times 10^{-6}$	Blackbody normalization
zgauss	LineE	0.864 ± 0.006	Gaussian emission line energy (keV)
zgauss	Sigma	0.150 ± 0.004	Gaussian emission line width (keV)
zgauss	norm	$(2.07 \pm 0.12) \times 10^{-4}$	Gaussian normalization
zpowerlw	PhoIndex	2.84 ± 0.01	Photon index
zpowerlw	norm	$(6.62 \pm 0.05) \times 10^{-4}$	Power law normalization

Table 4.2: Best-fit parameters for the TBabs(zbbody + zbbody + zgauss + zpowerlw) model tested on the averaged EPIC-pn data in the energy range E $= 0.3 - 10.0$ keV with fit statistic χ^2/d.o.f $= 1980/1288$.

where E_l is the source frame line energy, σ is the source frame line width, z is the redshift and K is the normalization constant. The total model is now represented as:

$$\texttt{TBabs} * (\texttt{zbbody} + \texttt{zbbody} + \texttt{zgauss} + \texttt{zpowerlw}).$$

This improves the fit of the soft band with a fit statistic of χ^2/d.o.f $= 1980/1288 \sim 1.5$.

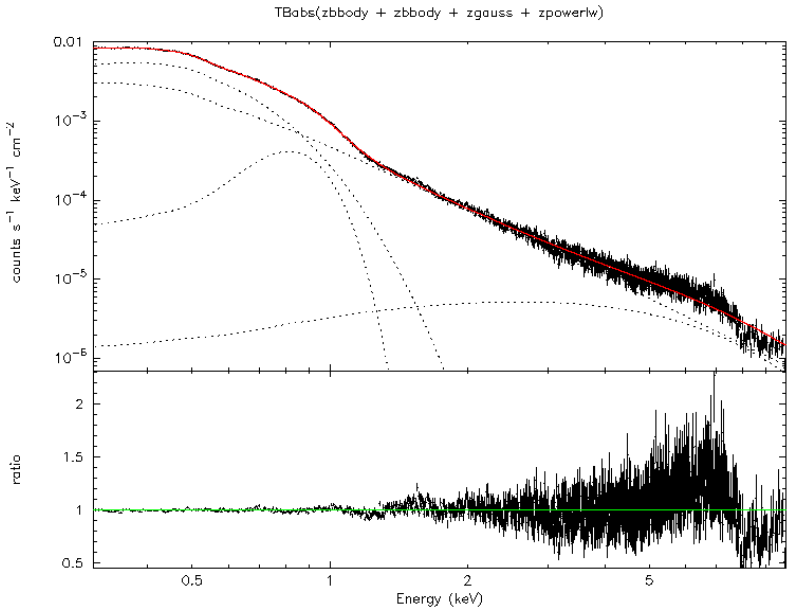

Figure 4.5: Best-fit with the model `TBabs(zbbody + zbbody + zgauss + zpowerlw)` (χ^2/d.o.f = 1980/1288).

4.4.2 XSTAR Modelling

The absorbed powerlaw model together with the phenomenological black body and Gaussian emission component fits well in the soft band. But it fails to satisfactorily represent the hard spectrum. Residuals (Fig. 4.5) show presence of strong spectral features, particularly some absorbtion features above E = 8 keV that indicates the presence of an UFO. To better characterize these additional features above the continuum, we use pre-computed photoionization simulations (see Sec. 2.5) to load them on the spectrum and then attempt to fit them. The output of these simulations is highly influenced by the spectral energy distribution of the incoming radiation that illuminates the photo-ionized gas.

The ionizing luminosity of the source used for computing the XSTAR (see Sec. 2.5.1) photoionization simulation in E = 2 - 10 keV range was computed to be

$$L_{1\text{-}1000\ \mathrm{Ry}} \sim 1.3 \times 10^{44}\ \mathrm{erg/s}$$

which is of the order of the Eddington limit for a black hole of mass $M_{BH} \sim 6 \times 10^6 M_\odot$Alston et al. (2019), where $L_{Edd} \sim 8 \times 10^{44}$ erg/s. Using `xstar2xspec`, a 5×5 grid of XSTAR simulations was computed by varying the ionization param-

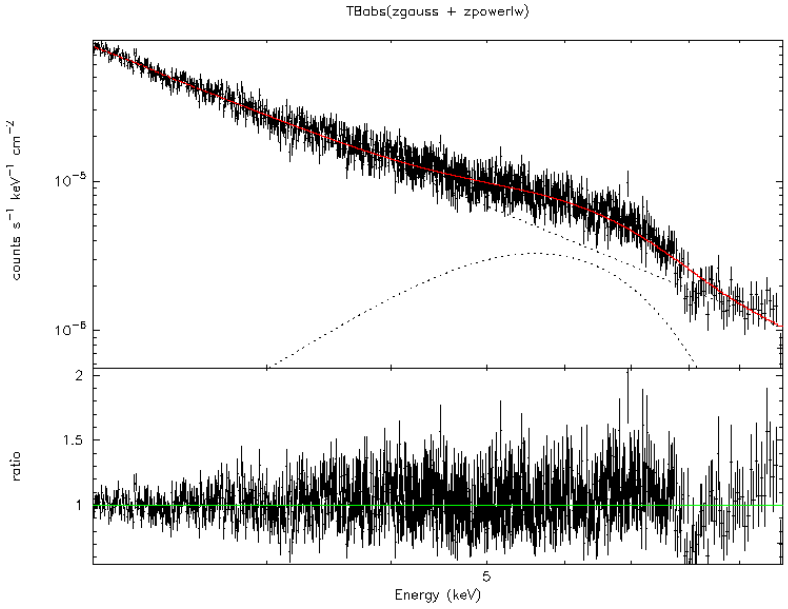

Figure 4.6: Best-fit with the model `TBabs(zgauss + zpowerlw)` in the energy range E = 2 - 10 keV (χ^2/d.o.f = 983/949).

eter logξ between 4 - 7 erg cm/s and column density N_H between $10^{21} - 10^{25}$ cm^{-2}. The turbulent velocity was fixed at 10000 km/s and the absorber was assumed to have solar abundances for every metal considered in XSTAR.

Initially, we focused on the hard energy spectrum (E > 2 keV) and started the fitting process by considering the absorbed powerlaw model for the continuum and a Gaussian component to model the broad emission features around E $\sim$ 6.0 keV. From the residuals (Fig. 4.6) we can see some absorption features around 8 keV.

We then loaded the XSTAR absorption table in XSPEC to perform fitting in the following way:

$$\texttt{TBabs} * \texttt{XSTAR} * (\texttt{zpowerlw} + \texttt{zgauss})$$

. We achieved a satisfactory fit statistic of χ^2/d.o.f = 914/946 from this analysis (Fig. 4.7). Subsequently, we extended the energy range of the spectrum to E = 0.3 - 10 keV to incorporate the soft X-ray band as well. We obtained the best fit by including two black body components and a Gaussian emission component to model

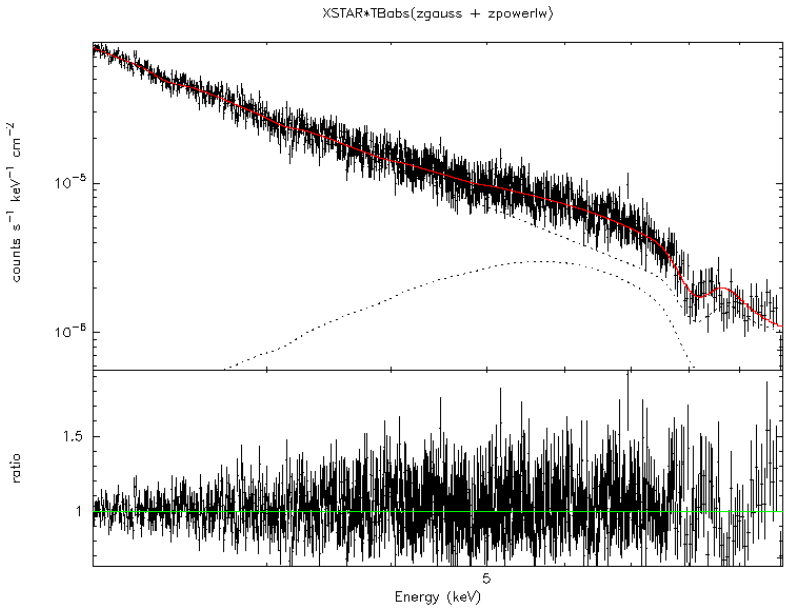

Figure 4.7: Best-fit with the model `TBabs*XSTAR*(zgauss + zpowerlw)` in the energy range E = 2 - 10 keV (χ^2/d.o.f = 914/946).

the soft spectrum. The final best fit model is:

$$\texttt{TBabs} * \texttt{XSTAR} * (\texttt{zbbody} + \texttt{zgauss} + \texttt{zbbody} + \texttt{zgauss} + \texttt{zpowerlw})$$

. With this model we obtained a good fit statistic of χ^2/d.o.f = 1548/1282 $\sim$ 1.21 (Fig. 4.8). The best fit parameters are presented in table 4.3.

4.4.3 WINE Modelling

Here, we reanalysed the X-ray spectrum with WINE (Luminari et al. (2018), Luminari et al. (2020), Luminari et al. (2021), Luminari (2024)) (see Sec. 2.5.2) for a detailed study of the outflow signatures. Our initial focus is on the hard X-ray spectrum (E = 2 - 10 keV), where the Fe K lines are observed. We loaded the required pre-computed spectra as WINE tables[1] within XSPEC to model the spectrum.

WINE tables are implemented as multiplicative table models in XSPEC. For the absorption, this directly modifies the primary continuum. But for the emission, it

[1]The WINE table models are taken from this link. These table models are presented in Luminari et al. 2024 (submitted) with different Spectral Energy Distributions (SEDs) and volume filling factors C_v.

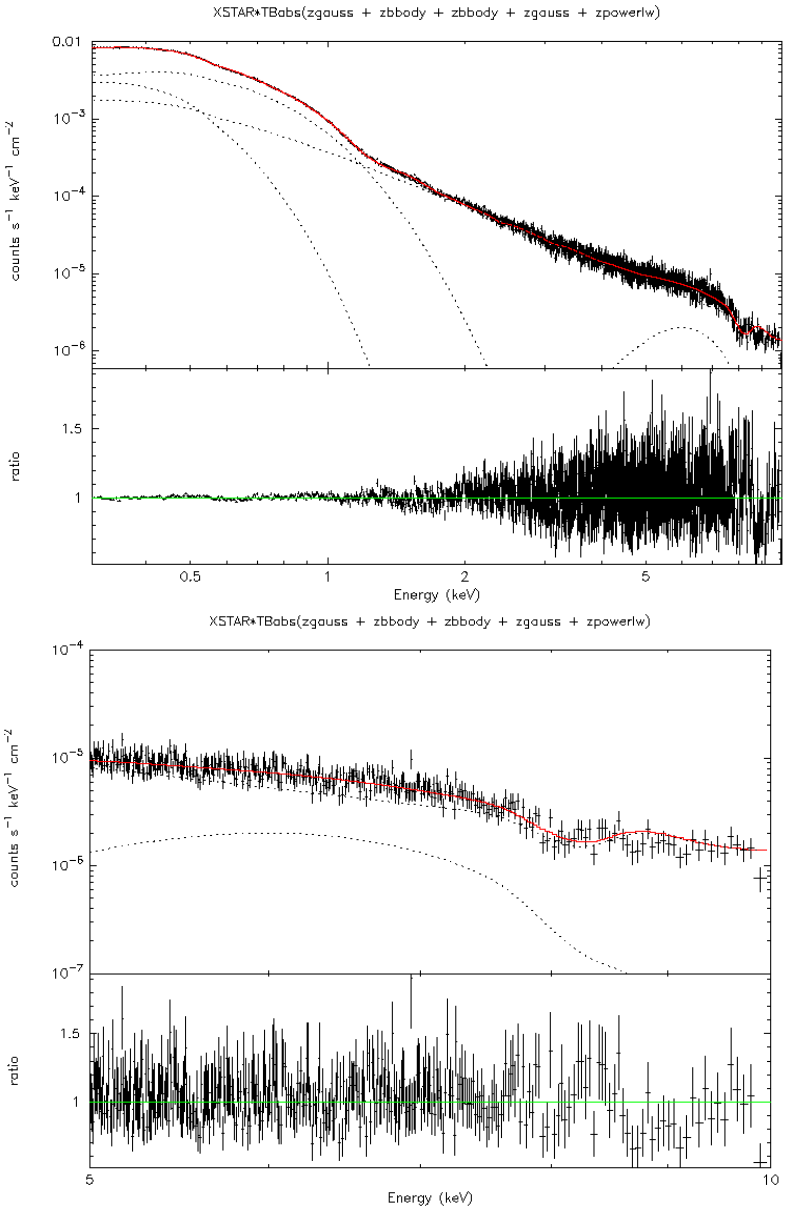

Figure 4.8: Best-fit with the model `TBabs*XSTAR*(zgauss + zbbody + zbbody + zgauss + zpowerlw)` in the energy range E = 0.3 - 10 keV (χ^2/d.o.f = 1548/1282). Bottom: zoomed in version of the plot showing the fit of the features above 8 keV.

Component	Parameter	Value	Description (Unit)
abs	rlogξ	$5.34^{+0.10}_{-0.53}$	Absorber ionization parameter (erg cm/s)
abs	column	$(8.08^{+3.18}_{-4.73}) \times 10^{23}$	Absorber column density (cm^{-2})
abs	z	$-0.153^{+0.006}_{-0.011}$	Absorber outflow velocity (c)
zbbody	kT	0.077 ± 0.001	Blackbody temperature (keV)
zbbody	norm	$(4.91 \pm 0.12) \times 10^{-5}$	Blackbody normalization
zbbody	kT	0.152 ± 0.001	Blackbody temperature (keV)
zbbody	norm	$(5.02 \pm 0.09) \times 10^{-5}$	Blackbody normalization
zgauss	LineE	1.227 ± 0.005	Gaussian line energy (keV)
zgauss	Sigma	0.154 ± 0.005	Gaussian line width (keV)
zgauss	norm	$(-6.3 \pm 0.4) \times 10^{-5}$	Gaussian normalization
zgauss	LineE	$6.40^{+0.08}_{-0.09}$	Gaussian line energy (keV)
zgauss	Sigma	1.19 ± 0.09	Gaussian line width (keV)
zgauss	norm	$(6.13^{+0.70}_{-0.64}) \times 10^{-6}$	Gaussian normalization
zpowerlw	PhoIndex	2.46 ± 0.02	Photon index
zpowerlw	norm	$(5.12 \pm 0.09) \times 10^{-4}$	Power law normalization

Table 4.3: Best-fit parameters for the `TBabs*XSTAR*(zgauss + zbbody + zbbody + zgauss + zpowerlw)` model tested on the averaged EPIC-pn data in the energy range E = 0.3 − 10.0 keV with fit statistic χ^2/d.o.f = 1548/1282. Errors are 1σ values.

employs a numerical strategy to ensure the normalisation.

We considered a simple powerlaw continuum which gets modified by the absorption and emission from the wind. We also take into account the cold distant galactic absorption. We create the absorption and emission models in XSPEC as $\texttt{WINE}_{\texttt{abs}}$ and $\texttt{WINE}_{\texttt{em}}$ respectively. We link all the powerlaw parameters between the two powerlaw components. This is done because the emission table is built as a set of ratios of emission-to-continuum spectra which simplifies the normalization and makes it easier to handle.

Narrow-Line Seyfert 1 SED Tables

We started the analysis by using the NLSy1 tables since the source is a NLSy1. We downloaded the absorption component with intrinsic turbulent velocity 3000 km/s and the emission component for volume filling factor C_v=0 and loaded the model in XSPEC as:

$$\texttt{TBabs} * (\texttt{WINE}_{\texttt{abs}} * \texttt{zpowerlw} + \texttt{WINE}_{\texttt{em}} * \texttt{zpowerlw})$$

.

The parameter space for the free parameters are defined as follows:

- Ionisation parameter $\log(\xi/\text{erg cm s}^{-1}) \epsilon$ [3.0,6.0] in steps of 0.25
- Outflow velocity $v_{out} \epsilon$ [0.0,0.4]c in steps of 0.025c
- Column density $N_H \epsilon$ [0,2×10^{24}] cm^{-2} in steps of 2×10^{23} cm^{-2}
- Opening angle of the cone $\theta_{out} \epsilon$ [0,90] deg in steps of 10 deg
- Line-of-sight inclination inc ϵ [0,90] deg in steps of 30 deg

In principle, the emission and absorption parameters of WINE can be independently adjusted. But, here we linked the column densities for the absorption and emission components of the wind. While the outflow velocity for the absorption component ranges between 0 to 0.4, the range of this parameter for the emission

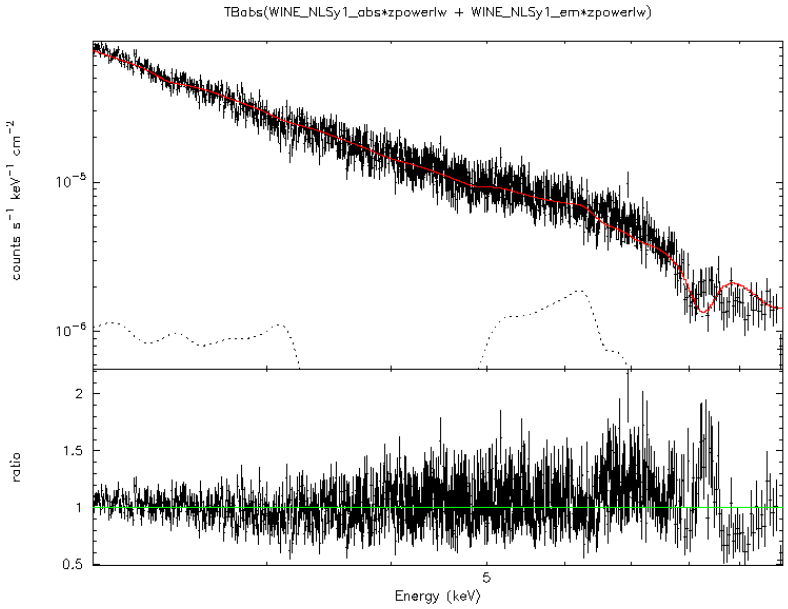

Figure 4.9: Best-fit with the model $\texttt{TBabs} * (\texttt{WINE}_{\texttt{abs}} * \texttt{zpowerlw} + \texttt{WINE}_{\texttt{em}} * \texttt{zpowerlw})$ with NLSy1 SED tables having intrinsic turbulent velocity 3000km/s (χ^2/d.o.f = 1083/945).

component is currently constrained between 0 and 0.15. Additionally, as can be seen from the fit parameters (Table 4.4), the hydrogen column density (N_H) reaches saturation at the maximum value of 2, and the value of θ_{out} is also saturated at 90 degree.

We also tried to fit the data using the SED table for intrinsic turbulent velocity 15000 km/s. This improves the fit statistic by $\Delta\chi^2 = 28$ but the same problem persisted (Fig. 4.10). We, therefore, tried modelling the data using the pre-computed WINE powerlaw SED tables.

Powerlaw SED Tables

Due to the limitations faced with the NLSy1 SED tables, we shifted to WINE powerlaw SED tables with photon index $\Gamma = 1.8$ to perform the analysis. As before, we downloaded the absorption and emission component for volume filling factor C_v=0 and intrinsic turbulent velocity 3000 km/s and loaded the model in XSPEC as before. The parameter space for the free parameters are defined as follows:

- Ionisation parameter $\log(\xi/\text{erg cm s}^{-1})$ ϵ [3.0,5.0] in steps of 0.25

Component	Parameter	Value	Description (Unit)
zpowerlw	PhoIndex	$2.42^{+0.01}_{-0.02}$	Photon index
zpowerlw	norm	$(5.04^{+0.06}_{-0.12}) \times 10^{-4}$	Power law normalization
abs	logξ	5.40 ± 0.05	Ionization parameter (erg cm/s)
abs	N_H	2.00 (saturated)*	Absorber column density (10^{24} cm^{-2})
abs	v_{out}	$0.261^{+0.003}_{-0.005}$	Absorber outflow velocity (c)
em	logξ	$3.25^{+0.02}_{-0.03}$	Ionization parameter (erg cm/s)
em	N_H	2.00 (saturated)*	Emission column density (10^{24} cm^{-2})
em	v_{out}	$0.141^{+0.007}_{-0.005}$	Emission outflow velocity (c)
em	inc	$58.54^{+8.86}_{-8.72}$	LOS inclination angle (deg)
em	θ_{out}	90 (saturated)	Opening angle of emitting region (deg)

Table 4.4: Best-fit parameters for the TBabs $*$ (WINE$_{abs}$ $*$ zpowerlw + WINE$_{em}$ $*$ zpowerlw) model with NLSy1 SED tables having intrinsic turbulent velocity 3000km/s when tested on the averaged EPIC-pn data in the energy range E = 2.0 − 10.0 keV gives the fit statistic as χ^2/d.o.f = 1083/945. Errors are 1σ values. $*$ parameters are linked together.

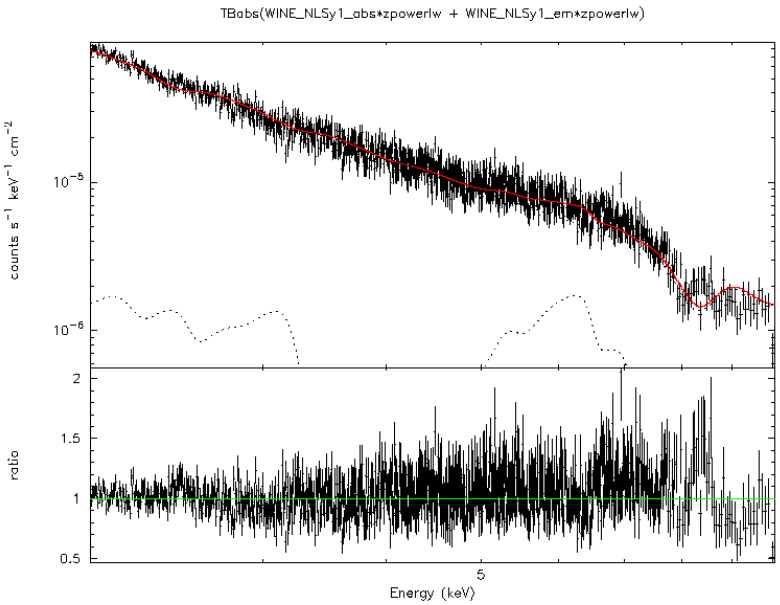

Figure 4.10: Best-fit with the model $\texttt{TBabs} * (\texttt{WINE}_{\texttt{abs}} * \texttt{zpowerlw} + \texttt{WINE}_{\texttt{em}} * \texttt{zpowerlw})$ with NLSy1 SED tables having intrinsic turbulent velocity 15000km/s (χ^2/d.o.f = 1055/945).

- Outflow velocity v_{out} ϵ [0.00,0.40]c in steps of 0.025c
- Column density N_H ϵ [0,2×10^{24}] cm^{-2} in steps of 2×10^{23} cm^{-2}
- Opening angle of the cone θ_{out} ϵ [0,90] deg in steps of 10 deg
- Line-of-sight inclination inc ϵ [0,90] deg in steps of 30 deg

Here, we linked the column density, outflow velocity and the ionization parameter between the absorption and emission component of the wind. The value for θ_{out} is kept constant at 90 degrees to consider the maximum opening angle of the outflow. Here too, the hydrogen column density (N_H) reaches saturation at its upper limit of 2. It is evident that the model is inadequate in fitting the data, particularly in the spectral range of 7-9 keV, as indicated by the plot (Fig. 4.11) and statistical analysis (Table 4.5).

To improve the fit we added a second layer of wind absorption and emission component in the model. This is loaded in XSPEC as:

$$\texttt{TBabs} * (\texttt{WINE}_{\texttt{abs}} * \texttt{WINE}_{\texttt{abs}} * \texttt{zpowerlw} + \texttt{WINE}_{\texttt{em}} * \texttt{WINE}_{\texttt{em}} * \texttt{zpowerlw}).$$

Component	Parameter	Value	Description (Unit)
zpowerlw	PhoIndex	2.40 ± 0.01	Photon index
zpowerlw	norm	$(4.94^{+0.06}_{-0.08}) \times 10^{-4}$	Power law normalization
abs	logξ	3.25 ± 0.01^{a}	Ionization parameter (erg cm/s)
abs	N_H	2.00 (saturated)^{b}	Absorber column density (10^{24} cm^{-2})
abs	v_{out}	0.221 ± 0.002^{c}	Absorber outflow velocity (c)
em	logξ	3.25 ± 0.01^{a}	Ionization parameter (erg cm/s)
em	N_H	2.00 (saturated)^{b}	Emission column density (10^{24} cm^{-2})
em	v_{out}	0.221 ± 0.002^{c}	Emission outflow velocity (c)
em	inc	$22.13^{+10.61}_{-12.08}$	LOS inclination angle (deg)
em	θ_{out}	90 (frozen)	Opening angle of emitting region (deg)

Table 4.5: Best-fit parameters for the TBabs $*$ (WINE$_{abs}$ $*$ zpowerlw + WINE$_{em}$ $*$ zpowerlw) model with powerlaw SED tables having intrinsic turbulent velocity 3000km/s when tested on the averaged EPIC-pn data in the energy range E = 2.0 − 10.0 keV gives the fit statistic as χ^2/d.o.f = 1098/948. Errors are 1σ values. Parameters marked 'a' are linked together, same for parameters marked with 'b' and 'c'.

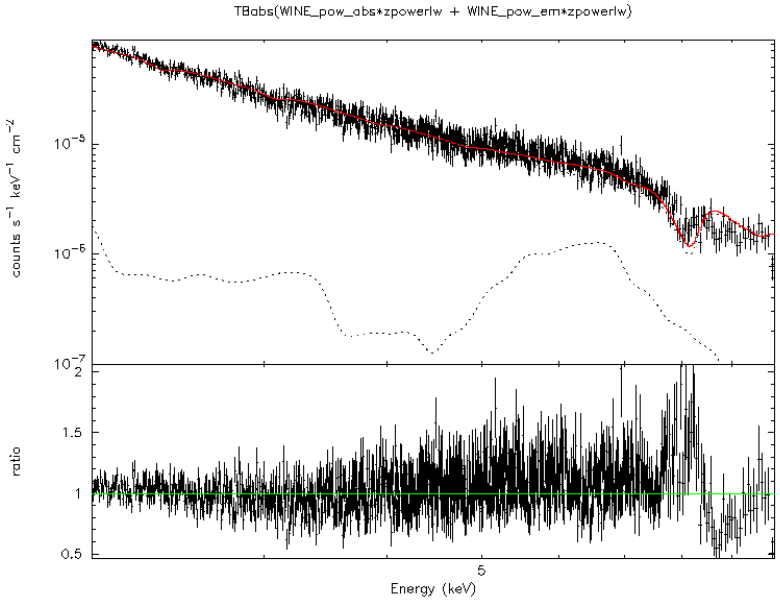

Figure 4.11: Best-fit with the model $\texttt{TBabs} * (\texttt{WINE}_{\texttt{abs}} * \texttt{zpowerlw} + \texttt{WINE}_{\texttt{em}} * \texttt{zpowerlw})$ with powerlaw SED tables having intrinsic turbulent velocity 3000km/s (χ^2/d.o.f = 1098/948).

The column density, outflow velocity and the ionization parameter of the first absorption component is linked to the first emission component, and similarly for the second layer of wind. In addition to this, the inclination angle of the first emission component is linked to the second emission component. The value for $\theta_{\rm out}$ remains constant at 90 degrees for both the emission components. Even though the hydrogen column density (N_H) saturates at the maximum value of 2, this model fits the data well with χ^2/d.o.f = 962.51/945 $\sim$ 1.02. The best-fit parameters are listed in table 4.6. From the plot (Fig. 4.12) it is evident that the spectral features between 7-9 keV have been well modelled.

To check if this extra layer of wind is statistically required, we perform the partial F-test (see Appendix A.2) with the two powerlaw SED WINE models considered here: the first one with only one layer of wind absorption and emission and the second model considering two layers of the wind. This test is used to evaluate if there is a statistically significant difference between a regression model and a nested version of that model. If the F-test probability is low then it is reasonable to add the extra model component. The F-test can be performed in XSPEC using the

Component	Parameter	Value	Description (Unit)
zpowerlw	PhoIndex	2.40 ± 0.02	Photon index
zpowerlw	norm	$(5.04^{+0.08}_{-0.09}) \times 10^{-4}$	Power law normalization
abs comp 1	logξ	3.24 ± 0.02^{a}	Ionization parameter (erg cm/s)
abs comp 1	N_H	2.00 (saturated)^{b}	Absorber column density (10^{24} cm^{-2})
abs comp 1	v_{out}	0.219 ± 0.002^{c}	Absorber outflow velocity (c)
em comp 1	logξ	3.24 ± 0.02^{a}	Ionization parameter (erg cm/s)
em comp 1	N_H	2.00 (saturated)^{b}	Emission column density (10^{24} cm^{-2})
em comp 1	v_{out}	0.219 ± 0.002^{c}	Emission outflow velocity (c)
abs comp 2	logξ	$3.26^{+0.04^{d}}_{-0.03}$	Ionization parameter (erg cm/s)
abs comp 2	N_H	2.00 (saturated)^{e}	Absorber column density (10^{24} cm^{-2})
abs comp 2	v_{out}	$0.309^{+0.004^{f}}_{-0.005}$	Absorber outflow velocity (c)
em comp 2	logξ	$3.26^{+0.04^{d}}_{-0.03}$	Ionization parameter (erg cm/s)
em comp 2	N_H	2.00 (saturated)^{e}	Emission column density (10^{24} cm^{-2})
em comp 2	v_{out}	$0.309^{+0.004^{f}}_{-0.005}$	Emission outflow velocity (c)
em	inc	$49.63^{+7.24}_{-9.78}$	LOS inclination angle (deg)
em	θ_{out}	90 (frozen)	Opening angle of emitting region (deg)

Table 4.6: Best-fit parameters for the TBabs $*$ ($\text{WINE}_{abs} * \text{WINE}_{abs} *$ zpowerlw + $\text{WINE}_{em} * \text{WINE}_{em} *$ zpowerlw) model with powerlaw SED tables having intrinsic turbulent velocity 3000km/s when tested on the averaged EPIC-pn data in the energy range $E = 2.0 - 10.0$ keV gives the fit statistic as χ^2/d.o.f $= 963/945$. Errors are 1σ values. Parameters marked 'a' are linked together, same for parameters marked with 'b', 'c', 'd', 'e' and 'f'.

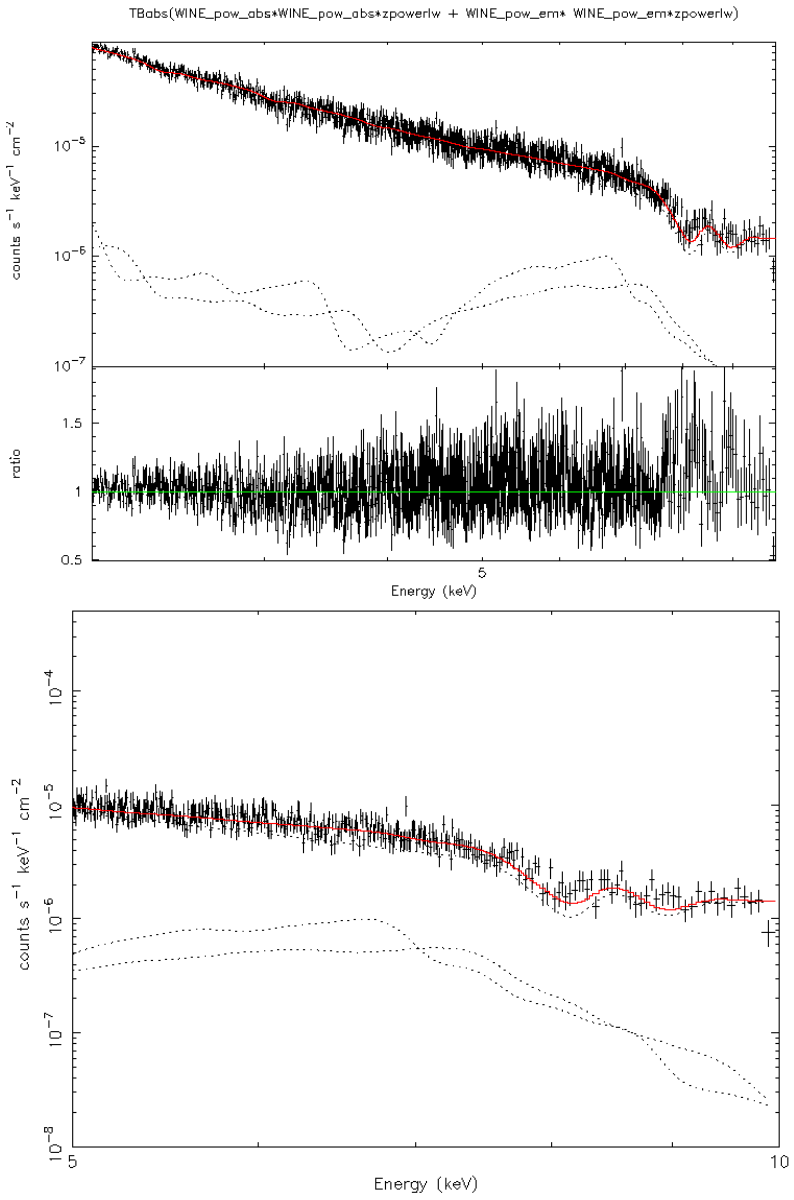

Figure 4.12: Best-fit with the model $\texttt{TBabs} * (\texttt{WINE}_{\texttt{abs}} * \texttt{WINE}_{\texttt{abs}} * \texttt{zpowerlw} + \texttt{WINE}_{\texttt{em}} * \texttt{WINE}_{\texttt{em}} * \texttt{zpowerlw})$ with powerlaw SED tables having intrinsic turbulent velocity 3000km/s (χ^2/d.o.f = 963/945). Bottom: zoomed in version of the plot showing the fit of the features above 8 keV.

`ftest` command. Using these two models we get an F-test value of 44.25 and the probability that the extra wind layer is random is 9.26 $\times 19^{-27}$, i.e., almost equal to zero. The confidence interval within which we have a probability (1 - P) that the extra component is not random can be expressed in terms of standard deviations as $\sigma \rightarrow \infty$.

Chapter 5

Discussion and Conclusions

5.1 WINE Modelling

The modelling of the hard X-ray spectrum (E = 2 - 10 keV) using the WINE powerlaw SED tables (see Sec. 4.4.3 and Table 4.6) provided us with an estimate of some of the properties of the AGN outflow in IRAS 13224-3809 galaxy. They are discussed below.

5.1.1 Ionization parameter

From our time-averaged analysis using the EPIC-pn data, we saw that the best fit to the above model was obtained by considering two layers of the wind. The ionization parameter, linked between the absorption and emission component for the first layer of the wind, is estimated to be:

$$\log \xi = 3.24 \pm 0.02 \text{ erg cm/s} \quad .$$

Similarly, the ionization parameter for the second layer of the wind is:

$$\log \xi = 3.26^{+0.04}_{-0.03} \text{ erg cm/s} \quad .$$

Because of this high ionization parameter, we predominantly expect Fe XXV/Fe XXVI absorption lines to be present. Previous studies using relativistic reflection model estimated the ionization parameter to be around $\xi \sim 4 - 5$ erg cm/s (e.g., Parker et al. (2017), Chartas and Canas (2018), Pinto et al. (2018)). In comparison, the ionization parameter value obtained with WINE modelling is notably low. Such

a low value would typically be accompanied by strong soft features that needs to be deeply investigated in the future.

5.1.2 Column density

Similar to the previous case, the absorber and emission column density were linked to each other for both layers of the wind. But, we were not able to obtain a proper estimate of the column density because it was saturated at the maximum possible value of the parameter space allowed for the SED table, i.e., $N_H \sim 2 \times 10^{24}$ cm^{-2}. Other studies have estimated the column density to be $\sim 8 \times 10^{22}$ cm^{-2} (Parker et al. (2017)) for the stacked EPIC-pn spectrum using reflection models.

5.1.3 Outflow velocity

The outflow velocity, linked between the absorption and emission component for the first layer of the wind, is estimated to be:

$$v_{out} = 0.219 \pm 0.002 \text{ c} \quad .$$

Similarly, for the second layer of the wind:

$$v_{out} = 0.309^{+0.004}_{-0.005} \text{ c} \quad .$$

Parker et al. (2017) reported an outflow velocity of ~ 0.2c for Fe XXV/XXVI lines using reflection models. Jiang et al. (2018) also reported the outflow velocity to be around 20-30% the speed of light from the blueshifted absorption lines of Ne X, S XVI, Mg XII, and Si XIV.

5.1.4 Inclination angle

The inclination of the line of sight (LOS) with respect to the symmetry axis of the cone (referring to the shape of the wind) is given by `inc`. This parameter is linked between the emission components of the two layers of the wind, giving a best fit value of:

$$\text{inc} = 49.63^{+7.24}_{-9.78} \text{ deg} \quad .$$

This inclination is in accordance with the classification of IRAS 13224-3809 as a Type 1 object. At this angle, the dusty torus is unlikely to absorb a significant fraction of the X-ray emission. Ponti et al. (2010) derived a similar value of the inclination

angle using disk relativistic reflection models. Other works found a slightly higher value of around inc ~ 60 deg (Parker et al. (2017) and Chiang et al. (2015)).

5.2 UFO Energetics

From the wind ionization level ξ, the column density N_H, and the projected velocity along the line-of-sight v_{out} values obtained by spectral fitting, we can obtain an estimate about the physical properties of the wind or outflows. In Sec. 2.6 we have discussed the equations that can be used to derive the location and energetics of the outflows. To do so, we will use the best-fit values mentioned in Table 4.6 for the above mentioned parameters. They are:

- For the first layer of the wind: $\log\xi_1 \sim 3.24$ erg cm/s, $N_{H,1} \sim 2 \times 10^{24}$ cm^{-2}, $v_{out,1} \sim 0.219$ c
- For the second layer of the wind: $\log\xi_2 \sim 3.26$ erg cm/s, $N_{H,2} \sim 2 \times 10^{24}$ cm^{-2}, $v_{out,2} \sim 0.309$ c

where 1 and 2 in the subscript denotes the first and second layer of the wind respectively. This notation will be followed from now on everywhere in this text.

We also consider $M_{BH} \approx 6 \times 10^6 M_\odot$ Alston et al. (2019), and so the gravitational radius is $R_g \approx 10^{12}$ cm[1].

$$R_g = \frac{GM_{BH}}{c^2} \approx 10^{12}\text{cm} \tag{5.1}$$

From eq. 2.30 we can obtain an estimate for the minimum radius from the source from which the outflow may have been launched:

$$r_{min,1} = \frac{2GM_{BH}}{v_{out,1}^2} \approx 35R_g \tag{5.2}$$

$$r_{min,2} = \frac{2GM_{BH}}{v_{out,2}^2} \approx 18R_g \tag{5.3}$$

[1]It corresponds to about 0.06 au which is the 15% of the Sun-Mercury distance.

The maximum ejection radius for the outflow can be calculated by using eq. 2.31. We use the value of ionizing luminosity as $L_{ion} \approx 1.3 \times 10^{44}$ erg/s:

$$r_{max,1} = \frac{L_{ion}}{\xi_1 N_{H,1}} \approx 37403 R_g \tag{5.4}$$

$$r_{max,2} = \frac{L_{ion}}{\xi_2 N_{H,2}} \approx 35720 R_g \tag{5.5}$$

From the values of r_{max} in eq. 5.4 and 5.5, we can see that the maximum ejection radius for the outflow is very large. This is because the ionization parameter $\log\xi \sim 3.2$ is relatively low for producing an inner disk outflow. This value is more suitable for producing larger scale outflows.

The average launching radius of the wind can also be calculated from its variability. According to Parker et al. (2017), the wind is variable on timescales $\lesssim 5$ ks, which corresponds to $\Delta t\ c \approx 170\ R_g$. So we can consider an average distance for the wind to be $r \approx 100\ R_g$. Then, using the first order formula in Eq. 2.33 we can estimate the mass-outflow rate expelled by the wind:

$$\dot{M}_{out,1} = 4\pi\mu r m_p N_{H,1} C_F v_{out,1} \approx 3.2 \times 10^{25} C_F \text{ g/s} \sim 0.5 C_F \ M_\odot \text{yr}^{-1} \tag{5.6}$$

$$\dot{M}_{out,2} = 4\pi\mu r m_p N_{H,2} C_F v_{out,2} \approx 4.5 \times 10^{25} C_F \text{ g/s} \sim 0.7 C_F \ M_\odot \text{yr}^{-1} \tag{5.7}$$

$$\dot{M}_{out,tot} = \dot{M}_{out,1} + \dot{M}_{out,2} \approx 1.2 C_F \ M_\odot \text{yr}^{-1} \tag{5.8}$$

where $\mu \approx 1.2$ (Gofford et al. (2015)) for fully ionized gas and solar abundances. To accurately calculate the mass outflow rate, we need an estimate of the covering fraction (C_F) of the wind. Parker et al. (2017) observed the absorption line in stacked archival data from 2011 which indicated a persistent and relatively consistent outflow feature for over five years. This hints at a significantly large covering fraction, otherwise, any clump along the line of sight might have drifted away over time. C_F can also be estimated from the opening angle of the emitting region, θ_{out}, but since it is frozen at 90 degree in our analysis, we can assume $C_F \sim 1$.

To compare, we can calculate the Eddington accretion rate for this source using eq. 1.4:

$$\dot{M}_{Edd} = \frac{L_{Edd}}{\eta c^2} \approx 0.4\ M_{\odot}\mathrm{yr}^{-1} \tag{5.9}$$

where L_{Edd} can be calculated using eq. 1.1 ($L_{Edd} \sim 8 \times 10^{44}$ erg/s) and efficiency η is assumed to be 0.3 for near-maximal spin (Parker et al. (2017)). We can see that the mass outflow rate is huge when compared to Eddington accretion rate. One reason for such high mass outflow rates is the value of the column density which is saturated at a very high value. This kind of wind could potentially remove about half of the matter intended for accretion, propelling it into the surrounding environment. This could possibly imply super-Eddington accretion at large radii (beyond r).

Parker et al. (2017) also estimated a high mass outflow rate of around 0.4 times Eddington accretion rate using disk reflection model. This case of IRAS 13224-3809 is analogous to the wind found in NGC 1313 X-1 which is an ultraluminous X-ray source (Pinto et al. (2016), Walton et al. (2016)). It also responds to changes in the continuum (Middleton et al. (2015)). This implies that super-Eddington relativistic winds might be a common phenomenon in high accretion rate black holes.

The kinetic power of the outflow can be calculated using eq. 2.34 as:

$$\dot{E}_{out,1} = \frac{1}{2}\dot{M}_{out,1}v^2_{out,1} \approx 6.9 \times 10^{44}\ \mathrm{erg/s} \approx 86\%\ L_{Edd} \tag{5.10}$$

$$\dot{E}_{out,2} = \frac{1}{2}\dot{M}_{out,2}v^2_{out,2} \approx 1.9 \times 10^{45}\ \mathrm{erg/s} \approx 237\%\ L_{Edd} \tag{5.11}$$

$$\dot{E}_{out,tot} = \dot{E}_{out,1} + \dot{E}_{out,2} \approx 2.6 \times 10^{45}\ \mathrm{erg/s} \tag{5.12}$$

Comparing the kinetic power of the outflow to the Eddington luminosity gives an understanding of the outflow's impact on the host galaxy and the efficiency of feedback processes in the AGN. If the kinetic power of the outflow is a significant fraction of the Eddington luminosity, it indicates that the outflow exerts considerable influence on its surroundings. This can be done by potentially driving out gas from the galaxy and quenching star formation. Therefore, this comparison provides infor-

mation about the effectiveness of AGN feedback in regulating galaxy evolution. A high ratio indicates that the outflow is fairly significant and can lead to powerful feedback effects, thereby being influential in shaping the galaxy's evolution.

We can also calculate the outflow momentum rate (or force) using eq. 2.35:

$$\dot{P}_{out,1} = \dot{M}_{out,1} v_{out,1} \approx 2.1 \times 10^{35} \text{ dyn} \tag{5.13}$$

$$\dot{P}_{out,2} = \dot{M}_{out,2} v_{out,2} \approx 4.2 \times 10^{35} \text{ dyn} \tag{5.14}$$

$$\dot{P}_{out,tot} = \dot{P}_{out,1} + \dot{P}_{out,2} \approx 6.3 \times 10^{35} \text{ dyn} \tag{5.15}$$

and compare it with the AGN momentum rate or radiation force using eq. 2.36:

$$\dot{P}_{rad} = \frac{L_{bol}}{c} \approx 1.3 \times 10^{34} \text{ dyn} \tag{5.16}$$

where $L_{bol} \sim 4 \times 10^{44}$ erg/s from Buisson et al. (2018). Since $\dot{P}_{rad} < \dot{P}_{out}$, the AGN radiation alone is not powerful enough to drive the observed outflow. Some other driving mechanism is also involved here which needs to be investigated. The high power of the wind obtained in our work suggests a possible magnetohydrodynamic (MHD) driving or at least a contribution of magnetic fields to radiative driving (e.g., see Tombesi et al. (2013), Fukumura et al. (2018b), Kraemer et al. (2018), Luminari et al. (2021)).

5.3 Future Prospects

In our analysis using the WINE table models, we have seen that some parameters (N_H) get saturated at their upper limits. So, our next step will be to re-analyze the data using NLSy1 SED WINE tables with the parameter range of N_H extended to higher values. We can also try to unfreeze the θ_{out} parameter to obtain the value for the opening angle and hence, the covering fraction C_F of the wind. This will provide a more clearer picture of the wind geometry.

In this work we performed a time averaged spectral analysis of the source. A time averaged spectrum provides a more stable and clearer view of the overall spectral characteristics of the AGN, leaving out the complexities associated with short-term variability. Also, it enhances the signal-to-noise ratio, thereby, revealing subtle features that might be lost in shorter time segments. Furthermore, it helps in identifying long-term trends and features in the absorption and emission from AGN, offering insights into its overall energy output and structure. But, there are certain disadvantages of averaging. The short-term variability, such as rapid flares or dips in luminosity, gets lost, and we can miss out on crucial details about the AGN's behavior. Averaging can also introduce bias and blending of different components if the AGN undergoes significant changes during the observation period, leading to inaccuracy in the spectral representation and misinterpretation of the physical processes at play.

On the other hand, even though time resolved spectra are complex and has lower signal-to-noise ratio, analysing them allows for the detection of rapid changes in the spectral properties of the AGN. This reveals important information about the dynamics and physical processes at play and helps in identifying distinct spectral states or transitions between states. It also enables to study correlations between spectral changes and other observable properties. Therefore, our future goal is to perform a time resolved and flux resolved analysis of this source using WINE to see how its geometry changes with time.

If a time-dependent photoionization is incorporated into WINE (Fig. 5.1), it will enable a precise correlation between the evolution of the outflow's ionization state and the variations of continuum luminosity Luminari (2024). A time-evolving study will allow us to perform a detailed examination of the outflow structure and track the evolving observational appearance of the UFO, which will be very useful for a highly variable source like IRAS 13224-3809.

The current X-ray spectrometers provide a good characterization of the outflow,

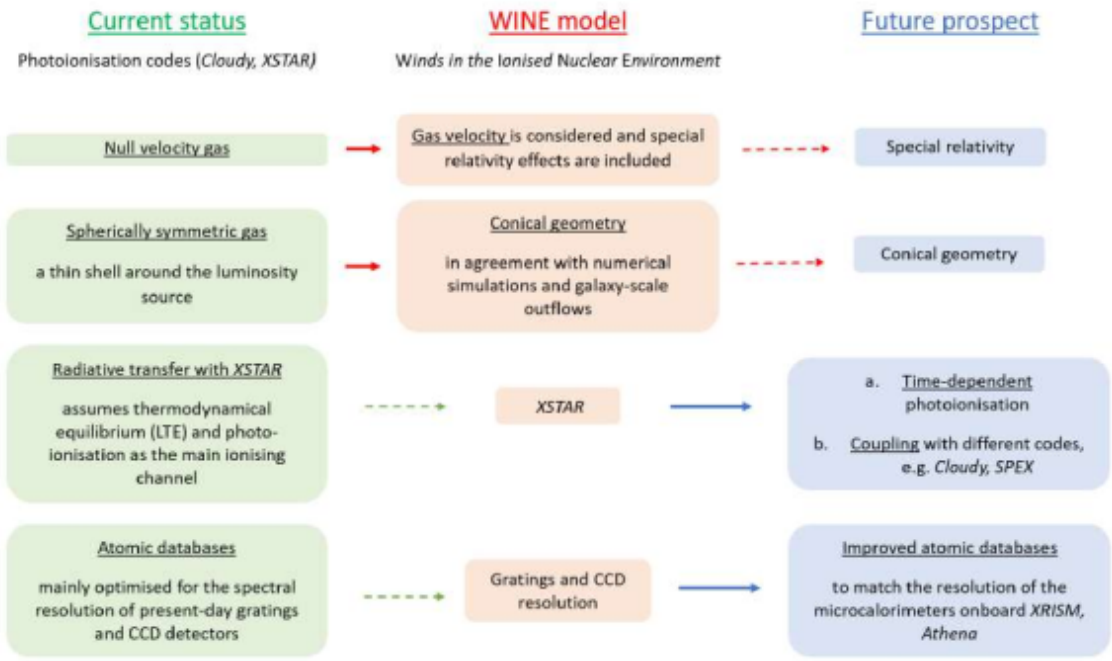

Figure 5.1: Main features of the current photoionization codes (left) and of the WINE model, in its actual version (center) and after future developments (right). Taken from Luminari (2024).

but with large uncertainties. They do not have enough energy resolution to resolve line profiles and different wind components or measure small line shifts. Accurate characterisation of the optically thick regions often becomes impossible because of line saturation. Due to this limitation, the key diagnostic for the origin of winds - the density-velocity profile is still not measured (Gandhi et al. (2022)). But, all these things can be reliably measured with use of calorimeters. They will be able to resolve lines in crowded regions of the spectrum which will allow multiple components of the wind to be easily disentangled.

The launch of the X-ray Imaging and Spectroscopy Mission (XRISM,Team et al. (2020)) in 2023 and Athena (Nandra et al. (2013)) in 2030s, optimised for energies $E \sim 0.5 - 10$ keV and spectral resolution of $\frac{E}{\Delta E} \geq 1000$, are something to look forward to. The Resolve microcalorimeter on XRISM has a spectral resolution of $\frac{E}{\Delta E} \approx 1200$ at the fluorescence Fe line energy of 6.4 keV. Its low background is expected to allow for the detection of significantly fainter outflows than currently achievable (Guainazzi and Tashiro (2018)). On the other hand, Athena's X-IFU

instrument (Barret et al. (2018)) aims for a high spatial resolution of approximately 5–10 arcseconds and a spectral resolution of $\frac{E}{\Delta E} \gtrsim 2600$. This will improve upon XRISM's best spectral resolution by a factor of $\approx$ 2–4 in the Fe band that will allow investigation of additional physical conditions, such as the abundance of the material outflowing from the torus. It will also enhance studies of X-ray reflecting clouds in nearby galactic bulges and the complex interplay between star formation and AGN activity (Nandra et al. (2013), García-Burillo et al. (2021), Kawamuro et al. (2019)). Fig. 5.2 shows a comparison of joint physical constraints on a mildly ionized outflow with a microcalorimeter (XRISM Resolve) and a CCD (XMM-Newton EPIC) done by Gandhi et al. (2022). It can be seen in the upper panel that the simulated CCD emission line is considerably broader than the corresponding line as seen by the microcalorimeter. The lower panel shows that degeneracy between two parameters limits the constraints that can be achieved with the CCD, but this will not be an issue with XRISM. In conclusion, with the use of microcalorimeters we expect advances in understanding the structures of accretion environments, in solving issues on the origins of energy and matter feedback and testing mass-scaled unification of accretion and feedback.

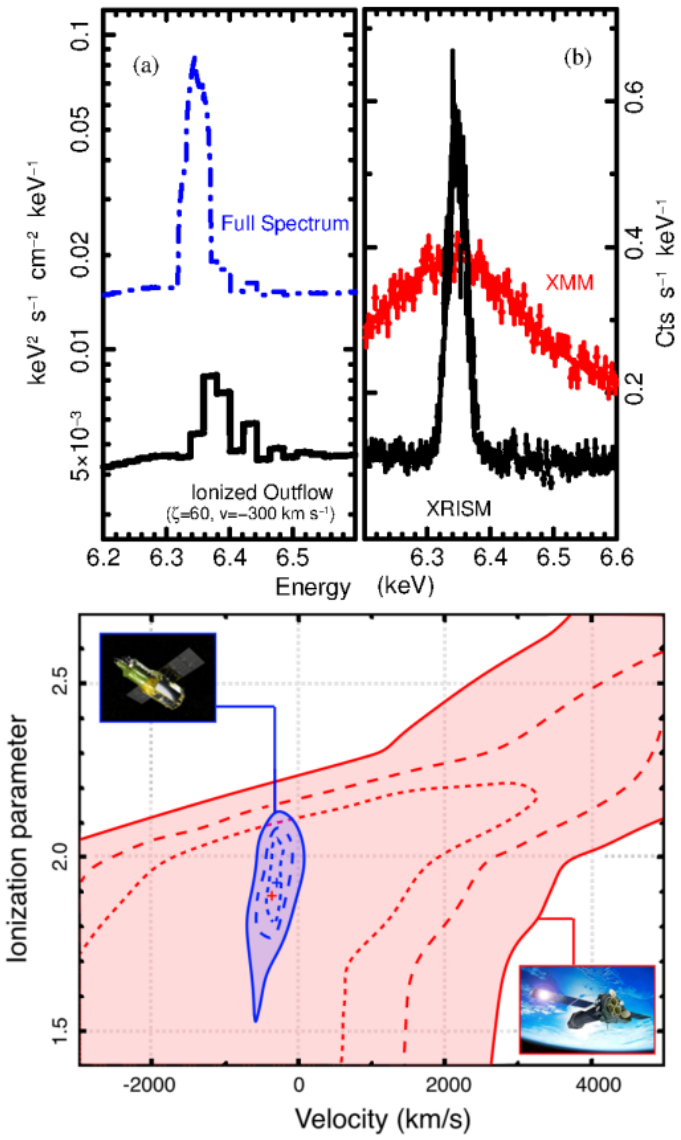

Figure 5.2: Comparison of joint physical constraints on a mild ionised outflow with a microcalorimeter vs. a CCD. (a): X-ray spectral model of the nearby Seyfert NGC 4388, including an additional ionised outflow in the Fe band. The ionised outflow contributes only a small fraction of the full spectrum line flux. (b): 300 ksec XMM-Newton (CCD; red) and XRISM (microcalorimeter; black) simulated counts spectra. A zoom-in around the Fe lines is shown, while the fit itself has been computed over a wider energy range. Lower panel: Fit contours at 68%, 90%, and 99% confidence levels between the ionization parameter log ξ and the outflow velocity. The red and blue contours are for XMM-Newton and XRISM, respectively. Negative velocities indicate blueshifts. The Resolve microcalorimeter on XRISM will be sensitive enough to decouple the degeneracy apparent with the CCD, and to pick out fine velocity shifts that are physically relevant in the outer ramparts of the accretion regime. Taken from Gandhi et al. (2022).

Bibliography

Abramowicz, M., Czerny, B., Lasota, J., and Szuszkiewicz, E. (1988). Slim accretion disks. *Astrophysical Journal, Part 1 (ISSN 0004-637X), vol. 332, Sept. 15, 1988, p. 646-658. Research supported by Observatoire de Paris and NASA.*, 332:646–658.

Allen, D. A., Norris, R., Meadows, V., and Roche, P. (1991). A large sample of southern iras galaxies: spectral classes and superclustering. *Monthly Notices of the Royal Astronomical Society*, 248(3):528–543.

Alston, W., Fabian, A., Buisson, D., Kara, E., Parker, M., Lohfink, A., Uttley, P., Wilkins, D., Pinto, C., De Marco, B., et al. (2019). The remarkable x-ray variability of iras 13224–3809–i. the variability process. *Monthly Notices of the Royal Astronomical Society*, 482(2):2088–2106.

Antonucci, R. (1993). Unified models for active galactic nuclei and quasars. *In: Annual review of astronomy and astrophysics. Vol. 31 (A94-12726 02-90), p. 473-521.*, 31:473–521.

Arav, N., Chamberlain, C., Kriss, G., Kaastra, J., Cappi, M., Mehdipour, M., Petrucci, P.-O., Steenbrugge, K., Behar, E., Bianchi, S., et al. (2015). Anatomy of the agn in ngc 5548-ii. the spatial, temporal, and physical nature of the outflow from hst/cos observations. *Astronomy & Astrophysics*, 577:A37.

Balbus, S. A. and Hawley, J. F. (1991). A powerful local shear instability in weakly magnetized disks. i-linear analysis. ii-nonlinear evolution. *Astrophysical Journal, Part 1 (ISSN 0004-637X), vol. 376, July 20, 1991, p. 214-233.*, 376:214–233.

Balbus, S. A. and Hawley, J. F. (1998). Instability, turbulence, and enhanced transport in accretion disks. *Reviews of modern physics*, 70(1):1.

Barret, D., Thien Lam Trong, den Herder, J.-W., Piro, L., Cappi, M., Huovelin, J., Kelley, R., Mas-Hesse, J., Mitsuda, K., Paltani, S., Rauw, G., Rozanska, A., Wilms, J., Bandler, S., Barbera, M., Barcons, X., Bozzo, E., Ceballos, M., Charles, I., Costantini, E., Decourchelle, A., den Hartog, R., Duband, L., Duval, J.-M., Fiore, F., Gatti, F., Goldwurm, A., Jackson, B., Jonker, P., Kilbourne, C., Macculi, C., Mendez, M., Molendi, S., Orleanski, P., Pajot, F., Pointecouteau, E., Porter, F., Pratt, G., Prele, D., Ravera, L., Sato, K., Schaye, J., Shinozaki, K., Thibert, T., Valenziano, L., Valette, V., Vink, J., Webb, N., Wise, M., Yamasaki, N., Delcelier-Douchin, F., Mesnager, J.-M., Pontet, B., Pradines, A., Branduardi-Raymont, G., Bulbul, E., Dadina, M., Ettori, S., Finoguenov, A., Fukazawa, Y., Janiuk, A., Kaastra, J., Mazzotta, P., Miller, J., Miniutti, G., Naze, Y., Nicastro, F., Sciortino, S., Simionescu, A., Torrejon, J., Geoffray, H., Peille, P., Aicardi, C., Andre, J., Garrido, G., Clenet, A., Daniel, C., Etcheverry, C., Frezouls, B., Gloaguen, E., Hervet, G., Jolly, A., Ledot, A., Maussang, I., Paillet, A., Schmisser, R., Travert, J.-M., Vella, B., Damery, J.-C., Boyce, K., DiPirro, M., Lotti, S., Schwander, D., Smith, S., van Leeuwen, B.-J., van Weers, H., Clerc, N., Cobo, B., Dauser, T., de Plaa, J., Kirsch, C., Cucchetti, E., Eckart, M., Ferrando, P., and Natalucci, L. (2018). The athena x-ray integral field unit (x-ifu). In Den-Herder, J., Nikzad, S., and Nakazawa, K., editors, *SPACE TELESCOPES AND INSTRUMENTATION 2018: ULTRAVIOLET TO GAMMA RAY*, Proceedings of SPIE, United States. SPIE - the international society for optics and photonics. Conference on Space Telescopes and Instrumentation - Ultraviolet to Gamma Ray ; Conference date: 10-06-2018 Through 15-06-2018.

Bautista, M. and Kallman, T. (2001). The xstar atomic database. *The Astrophysical Journal Supplement Series*, 134(1):139.

Beckmann, V. and Shrader, C. (2012). *Active galactic nuclei*. John Wiley & Sons.

Begelman, M. C., McKee, C. F., and Shields, G. A. (1983). Compton heated winds and coronae above accretion disks. i dynamics. *Astrophysical Journal, Part 1 (ISSN 0004-637X), vol. 271, Aug. 1, 1983, p. 70-88. Research supported by the Science Research Council of England.*, 271:70–88.

Behar, E. (2009). Density profiles in seyfert outflows. *The Astrophysical Journal*, 703(2):1346.

Behar, E., Rasmussen, A. P., Blustin, A. J., Sako, M., Kahn, S. M., Kaastra, J. S., Branduardi-Raymont, G., and Steenbrugge, K. C. (2003). A long look at ngc 3783 with the xmm-newton reflection grating spectrometer. *The Astrophysical Journal*, 598(1):232.

Blandford, R. D. and Payne, D. (1982). Hydromagnetic flows from accretion discs and the production of radio jets. *Monthly Notices of the Royal Astronomical Society*, 199(4):883–903.

Blustin, A., Page, M., Fuerst, S., Branduardi-Raymont, G., and Ashton, C. (2005). The nature and origin of seyfert warm absorbers. *Astronomy & Astrophysics*, 431(1):111–125.

Boiler, T., Brandt, W., Fabian, A., and Fink, H. (1997). Rosat monitoring of persistent giant and rapid variability in the narrow-line seyfert 1 galaxy iras 13224-3809. *Monthly Notices of the Royal Astronomical Society*, 289(2):393–405.

Bondi, H. (1952). On spherically symmetrical accretion. *Monthly Notices of the Royal Astronomical Society*, 112(2):195–204.

Brandt, W. and Alexander, D. (2015). Cosmic x-ray surveys of distant active galaxies: The demographics, physics, and ecology of growing supermassive black holes. *The Astronomy and Astrophysics Review*, 23(1):1.

Brinkman, A. C., Aarts, H. J., den Boggende, A. J., Bootsma, T., Dubbeldam, L., den Herder, J.-W., Kaastra, J. S., de Korte, P. A., van Leeuwen, B., Mewe, R., et al. (1996). Reflection grating spectrometer on board xmm. In *EUV, X-Ray, and Gamma-Ray Instrumentation for Astronomy VII*, volume 2808, pages 463–480. SPIE.

Bruni, G., Piconcelli, E., Misawa, T., Zappacosta, L., Saturni, F., Vietri, G., Vignali, C., Bongiorno, A., Duras, F., Feruglio, C., et al. (2019). The wissh quasars

project-vi. fraction and properties of bal quasars in the hyper-luminosity regime. *Astronomy & Astrophysics*, 630:A111.

Buisson, D., Lohfink, A., Alston, W., Cackett, E., Chiang, C., Dauser, T., De Marco, B., Fabian, A., Gallo, L., García, J., et al. (2018). Is there a uv/x-ray connection in iras 13224- 3809? *Monthly Notices of the Royal Astronomical Society*, 475(2):2306–2313.

Castor, J. I., Abbott, D. C., and Klein, R. I. (1975). Radiation-driven winds in of stars. *Astrophysical Journal, vol. 195, Jan. 1, 1975, pt. 1, p. 157-174.*, 195:157–174.

Chartas, G. and Canas, M. H. (2018). The variable relativistic outflow of iras 13224–3809. *The Astrophysical Journal*, 867(2):103.

Chelouche, D. and Netzer, H. (2005). Dynamical and spectral modeling of the ionized gas and nuclear environment in ngc 3783. *The Astrophysical Journal*, 625(1):95.

Chiang, C.-Y., Walton, D., Fabian, A., Wilkins, D., and Gallo, L. C. (2015). Modelling the extreme x-ray spectrum of iras 13224- 3809. *Monthly Notices of the Royal Astronomical Society*, 446(1):759–769.

Cicone, C., Brusa, M., Ramos Almeida, C., Cresci, G., Husemann, B., and Mainieri, V. (2018). The largely unconstrained multiphase nature of outflows in agn host galaxies. *Nature Astronomy*, 2(3):176–178.

Cicone, C., Maiolino, R., Sturm, E., Graciá-Carpio, J., Feruglio, C., Neri, R., Aalto, S., Davies, R., Fiore, F., Fischer, J., et al. (2014). Massive molecular outflows and evidence for agn feedback from co observations. *Astronomy & Astrophysics*, 562:A21.

Collin, S. and Kawagachi, T. (2004). Accretion rates in narrow line seyfert 1 galaxies and the growth of massive black holes. *SF2A-2004: Semaine de l'Astrophysique Francaise*, page 335.

Crenshaw, D. M. and Kraemer, S. B. (2012). Feedback from mass outflows in nearby active galactic nuclei. i. ultraviolet and x-ray absorbers. *The Astrophysical Journal*, 753(1):75.

Crenshaw, D. M., Kraemer, S. B., and George, I. M. (2003). Mass loss from the nuclei of active galaxies. *Annual Review of Astronomy and Astrophysics*, 41(1):117–167.

Cresci, G., Mainieri, V., Brusa, M., Marconi, A., Perna, M., Mannucci, F., Piconcelli, E., Maiolino, R., Feruglio, C., Fiore, F., et al. (2015). Blowin'in the wind: both "negative" and "positive" feedback in an obscured high-z quasar. *The Astrophysical Journal*, 799(1):82.

Crummy, J., Fabian, A., Gallo, L., and Ross, R. (2006). An explanation for the soft x-ray excess in active galactic nuclei. *Monthly Notices of the Royal Astronomical Society*, 365(4):1067–1081.

Danehkar, A., Nowak, M. A., Lee, J. C., Kriss, G. A., Young, A. J., Hardcastle, M. J., Chakravorty, S., Fang, T., Neilsen, J., Rahoui, F., et al. (2018). The ultrafast outflow of the quasar pg 1211+ 143 as viewed by time-averaged chandra grating spectroscopy. *The Astrophysical Journal*, 853(2):165.

Den Herder, J., Brinkman, A., Kahn, S., Branduardi-Raymont, G., Thomsen, K., Aarts, H., Audard, M., Bixler, J., den Boggende, A., Cottam, J., et al. (2001). The reflection grating spectrometer on board xmm-newton. *Astronomy & Astrophysics*, 365(1):L7–L17.

Dewangan, G., Griffiths, R., Dasgupta, S., and Rao, A. (2007). An investigation of the origin of soft x-ray excess emission from ark 564 and mrk 1044. *The Astrophysical Journal*, 671(2):1284.

Done, C., Tomaru, R., and Takahashi, T. (2018). Thermal winds in stellar mass black hole and neutron star binary systems. *Monthly Notices of the Royal Astronomical Society*, 473(1):838–848.

Dorodnitsyn, A. and Kallman, T. (2012). Agn obscuration from winds: from dusty infrared-driven to warm and x-ray photoionized. *arXiv preprint arXiv:1211.6402*.

Dunlop, J., McLure, R., Kukula, M., Baum, S., O'Dea, C., and Hughes, D. (2003). Quasars, their host galaxies and their central black holes. *Monthly Notices of the Royal Astronomical Society*, 340(4):1095–1135.

Elitzur, M. and Shlosman, I. (2006). The agn-obscuring torus: the end of the "doughnut" paradigm? *The Astrophysical Journal*, 648(2):L101.

Faber, S. and Jackson, R. E. (1976). Velocity dispersions and mass-to-light ratios for elliptical galaxies. *Astrophysical Journal, vol. 204, Mar. 15, 1976, pt. 1, p. 668-683.*, 204:668–683.

Fabian, A., Kara, E., Walton, D., Wilkins, D., Ross, R., Lozanov, K., Uttley, P., Gallo, L., Zoghbi, A., Miniutti, G., et al. (2013). Long xmm observation of the narrow-line seyfert 1 galaxy iras 13224- 3809: rapid variability, high spin and a soft lag. *Monthly Notices of the Royal Astronomical Society*, 429(4):2917–2923.

Fabian, A., Rees, M., Stella, L., and White, N. E. (1989). X-ray fluorescence from the inner disc in cygnus x-1. *Monthly Notices of the Royal Astronomical Society*, 238(3):729–736.

Fabian, A., Vaughan, S., Nandra, K., Iwasawa, K., Ballantyne, D., Lee, J., De Rosa, A., Turner, A., and Young, A. (2002). A long hard look at mcg–6-30-15 with xmm-newton. *Monthly Notices of the Royal Astronomical Society*, 335(1):L1–L5.

Fanaroff, B. L. and Riley, J. M. (1974). The morphology of extragalactic radio sources of high and low luminosity. *Monthly Notices of the Royal Astronomical Society*, 167(1):31P–36P.

Faucher-Giguère, C.-A. and Quataert, E. (2012). The physics of galactic winds driven by active galactic nuclei. *Monthly Notices of the Royal Astronomical Society*, 425(1):605–622.

Ferland, G., Chatzikos, M., Guzmán, F., Lykins, M., Van Hoof, P., Williams, R., Abel, N., Badnell, N., Keenan, F., Porter, R., et al. (2017). The 2017 release of cloudy. *Revista mexicana de astronomía y astrofísica*, 53(2).

Ferland, G., Korista, K., Verner, D., Ferguson, J., Kingdon, J., and Verner, E. (1998). Cloudy 90: numerical simulation of plasmas and their spectra. *Publications of the Astronomical Society of the Pacific*, 110(749):761.

Ferrarese, L. and Merritt, D. (2000). A fundamental relation between supermassive black holes and their host galaxies. *The Astrophysical Journal*, 539(1):L9.

Feruglio, C., Fiore, F., Carniani, S., Piconcelli, E., Zappacosta, L., Bongiorno, A., Cicone, C., Maiolino, R., Marconi, A., Menci, N., et al. (2015). The multi-phase winds of markarian 231: from the hot, nuclear, ultra-fast wind to the galaxy-scale, molecular outflow. *Astronomy & Astrophysics*, 583:A99.

Fiore, F., Feruglio, C., Shankar, F., Bischetti, M., Bongiorno, A., Brusa, M., Carniani, S., Cicone, C., Duras, F., Lamastra, A., et al. (2017). Agn wind scaling relations and the co-evolution of black holes and galaxies. *Astronomy & Astrophysics*, 601:A143.

Foschini, L. (2011). Evidence of powerful relativistic jets in narrow-line seyfert 1 galaxies. *arXiv preprint arXiv:1105.0772*.

Fukumura, K., Dadina, M., Matzeu, G., Tombesi, F., Shrader, C., and Kazanas, D. (2022). Tell-tale spectral signatures of mhd-driven ultrafast outflows in agns. *The Astrophysical Journal*, 940(1):6.

Fukumura, K., Kazanas, D., Contopoulos, I., and Behar, E. (2010). Modeling high-velocity qso absorbers with photoionized magnetohydrodynamic disk winds. *The Astrophysical Journal Letters*, 723(2):L228.

Fukumura, K., Kazanas, D., Shrader, C., Behar, E., Tombesi, F., and Contopoulos, I. (2017). Magnetic origin of black hole winds across the mass scale. *Nature Astronomy*, 1(4):0062.

Fukumura, K., Kazanas, D., Shrader, C., Behar, E., Tombesi, F., and Contopoulos, I. (2018a). Magnetized disk winds in ngc 3783. *The Astrophysical Journal*, 853(1):40.

Fukumura, K., Kazanas, D., Shrader, C., Behar, E., Tombesi, F., and Contopoulos, I. (2018b). Variable nature of magnetically driven ultra-fast outflows. *The Astrophysical Journal Letters*, 864(2):L27.

Fukumura, K., Tombesi, F., Kazanas, D., Shrader, C., Behar, E., and Contopoulos, I. (2013). Stratified magnetically driven accretion-disk winds and their relations to jets. *The Astrophysical Journal*, 780(2):120.

Fukumura, K., Tombesi, F., Kazanas, D., Shrader, C., Behar, E., and Contopoulos, I. (2015). Magnetically driven accretion disk winds and ultra-fast outflows in pg 1211+ 143. *The Astrophysical Journal*, 805(1):17.

Galeev, A., Rosner, R., and Vaiana, G. (1979). Structured coronae of accretion disks. *Astrophysical Journal, Part 1, vol. 229, Apr. 1, 1979, p. 318-326. Research supported by the Smithsonian Institution, Consiglio Nazionale delle Ricerche, and CRRN.*, 229:318–326.

Gallo, L. C., Boller, T., Tanaka, Y., Fabian, A., Brandt, W., Welsh, W., Anabuki, N., and Haba, Y. (2004). The x-ray variability of the narrow-line type 1 seyfert galaxy iras 13224-3809 from an xmm-newton observation. *Monthly Notices of the Royal Astronomical Society*, 347(1):269–276.

Gandhi, P., Kawamuro, T., Trigo, M. D., Paice, J., Boorman, P., Cappi, M., Done, C., Fabian, A., Fukumura, K., Garcia, J., et al. (2022). Accretion physics at high x-ray spectral resolution: New frontiers and game-changing science. *arXiv preprint arXiv:2209.10576*.

García-Burillo, S., Alonso-Herrero, A., Almeida, C. R., González-Martín, O., Combes, F., Usero, A., Hönig, S., Querejeta, M., Hicks, E., Hunt, L. K., et al. (2021). The galaxy activity, torus, and outflow survey (gatos)-i. alma images of dusty molecular tori in seyfert galaxies. *Astronomy & Astrophysics*, 652:A98.

Gebhardt, K., Bender, R., Bower, G., Dressler, A., Faber, S., Filippenko, A. V., Green, R., Grillmair, C., Ho, L. C., Kormendy, J., et al. (2000). A relationship

between nuclear black hole mass and galaxy velocity dispersion. *The Astrophysical Journal*, 539(1):L13.

Ghisellini, G., Haardt, F., and Matt, G. (1994). The contribution of the obscuring torus to the x-ray spectrum of seyfert galaxies: a test for the unification model. *Monthly Notices of the Royal Astronomical Society*, 267(3):743–754.

Gianolli, V., Kim, D., Bianchi, S., Agís-González, B., Madejski, G., Marin, F., Marinucci, A., Matt, G., Middei, R., Petrucci, P., et al. (2023). Uncovering the geometry of the hot x-ray corona in the seyfert galaxy ngc 4151 with ixpe. *Monthly Notices of the Royal Astronomical Society*, 523(3):4468–4476.

Gierliński, M. and Done, C. (2004). Is the soft excess in active galactic nuclei real? *Monthly Notices of the Royal Astronomical Society*, 349(1):L7–L11.

Giustini, M. and Proga, D. (2019). The role of failed accretion disk winds in active galactic nuclei. *Proceedings of the International Astronomical Union*, 15(S356):82–86.

Gofford, J., Reeves, J., McLaughlin, D., Braito, V., Turner, T., Tombesi, F., and Cappi, M. (2015). The suzaku view of highly ionized outflows in agn–ii. location, energetics and scalings with bolometric luminosity. *Monthly Notices of the Royal Astronomical Society*, 451(4):4169–4182.

Greene, J. E. and Ho, L. C. (2007). The mass function of active black holes in the local universe. *The Astrophysical Journal*, 667(1):131.

Guainazzi, M. and Tashiro, M. S. (2018). The hot universe with xrism and athena. *Proceedings of the International Astronomical Union*, 14(S342):29–36.

Gupta, A., Mathur, S., Krongold, Y., and Nicastro, F. (2013). Discovery of relativistic outflow in the seyfert galaxy ark 564. *The Astrophysical Journal*, 772(1):66.

Haardt, F. and Maraschi, L. (1991). A two-phase model for the x-ray emission from seyfert galaxies. *Astrophysical Journal, Part 2-Letters (ISSN 0004-637X), vol. 380, Oct. 20, 1991, p. L51-L54.*, 380:L51–L54.

Haardt, F. and Maraschi, L. (1993). X-ray spectra from two-phase accretion disks. *Astrophysical Journal, Part 1 (ISSN 0004-637X), vol. 413, no. 2, p. 507-517.*, 413:507–517.

Hamann, F., Chartas, G., Reeves, J., and Nardini, E. (2018). Does the x-ray outflow quasar pds 456 have a uv outflow at 0.3 c? *Monthly Notices of the Royal Astronomical Society*, 476(1):943–953.

Harrison, C., Alexander, D., Mullaney, J., and Swinbank, A. (2014). Kiloparsec-scale outflows are prevalent among luminous agn: outflows and feedback in the context of the overall agn population. *Monthly Notices of the Royal Astronomical Society*, 441(4):3306–3347.

HI4PI Collaboration:, Ben Bekhti, N., Flöer, L., Keller, R., Kerp, J., Lenz, D., Winkel, B., Bailin, J., Calabretta, M. R., Dedes, L., Ford, H. A., Gibson, B. K., Haud, U., Janowiecki, S., Kalberla, P. M. W., Lockman, F. J., McClure-Griffiths, N. M., Murphy, T., Nakanishi, H., Pisano, D. J., and Staveley-Smith, L. (2016). Hi4pi: a full-sky h-i survey based on ebhis and gass. *AA*, 594:A116.

Higginbottom, N., Proga, D., Knigge, C., Long, K. S., Matthews, J. H., and Sim, S. A. (2014). Line-driven disk winds in active galactic nuclei: the critical importance of ionization and radiative transfer. *The Astrophysical Journal*, 789(1):19.

Ho, L. C. and Wang, J.-W. (2007). The central engine of active galactic nuclei. *The Central Engine of Active Galactic Nuclei*, 373.

Holczer, T., Behar, E., and Kaspi, S. (2007). Absorption measure distribution of the outflow in iras 13349+ 2438: direct observation of thermal instability? *The Astrophysical Journal*, 663(2):799.

Ji, H., Burin, M., Schartman, E., and Goodman, J. (2006). Hydrodynamic turbulence cannot transport angular momentum effectively in astrophysical disks. *Nature*, 444(7117):343–346.

Jiang, J., Dauser, T., Fabian, A. C., Alston, W. N., Gallo, L. C., Parker, M. L., and Reynolds, C. S. (2022). Xmm–newton observations of the narrow-line seyfert 1

galaxy iras 13224- 3809: X-ray spectral analysis ii. *Monthly Notices of the Royal Astronomical Society*, 514(1):1107–1121.

Jiang, J., Parker, M., Fabian, A., Alston, W., Buisson, D., Cackett, E., Chiang, C., Dauser, T., Gallo, L., García, J., et al. (2018). The 1.5 ms observing campaign on iras 13224- 3809–i. x-ray spectral analysis. *Monthly Notices of the Royal Astronomical Society*, 477(3):3711–3726.

Kaastra, J., Mewe, R., Nieuwenhuijzen, H., Yamashita, K., Watanabe, T., et al. (1996). Uv and x-ray spectroscopy of astrophysical and laboratory plasmas.

Kallman, T. and Bautista, M. (2001). Photoionization and high-density gas. *The Astrophysical Journal Supplement Series*, 133(1):221.

Kato, Y., Mineshige, S., and Shibata, K. (2004). Magnetohydrodynamic accretion flows: Formation of magnetic tower jet and subsequent quasi-steady state. *The Astrophysical Journal*, 605(1):307.

Kawamuro, T., Izumi, T., and Imanishi, M. (2019). A chandra and alma study of x-ray-irradiated gas in the central 100 pc of the circinus galaxy. *Publications of the Astronomical Society of Japan*, 71(4):68.

Kazanas, D., Fukumura, K., Behar, E., Contopoulos, I., and Shrader, C. (2012). Toward a unified agn structure. *arXiv preprint arXiv:1206.5022*.

Khachikian, E. Y. and Weedman, D. W. (1974). An atlas of seyfert galaxies. *Astrophysical Journal, vol. 192, Sept. 15, 1974, pt. 1, p. 581-589.*, 192:581–589.

King, A. and Pounds, K. (2015). Powerful outflows and feedback from active galactic nuclei. *Annual Review of Astronomy and Astrophysics*, 53(1):115–154.

King, A. R. (2010). Black hole outflows. , 402(3):1516–1522.

King, A. R. and Pounds, K. A. (2003). Black hole winds. *Monthly Notices of the Royal Astronomical Society*, 345(2):657–659.

Kormendy, J. and Ho, L. C. (2013). Coevolution (or not) of supermassive black holes and host galaxies. *Annual Review of Astronomy and Astrophysics*, 51(1):511–653.

Kraemer, S., Tombesi, F., and Bottorff, M. (2018). Physical conditions in ultra-fast outflows in agn. *The Astrophysical Journal*, 852(1):35.

Kriss, G. A., Lee, J. C., and Danehkar, A. (2018). A search for h i lyα counterparts to ultrafast x-ray outflows. *The Astrophysical Journal*, 859(2):94.

Krongold, Y., Nicastro, F., Elvis, M., Brickhouse, N., Binette, L., Mathur, S., and Jiménez-Bailón, E. (2007). The compact, conical, accretion-disk warm absorber of the seyfert 1 galaxy ngc 4051 and its implications for igm-galaxy feedback processes. *The Astrophysical Journal*, 659(2):1022.

Laha, S., Reynolds, C. S., Reeves, J., Kriss, G., Guainazzi, M., Smith, R., Veilleux, S., and Proga, D. (2021). Ionized outflows from active galactic nuclei as the essential elements of feedback. *Nature Astronomy*, 5(1):13–24.

LaMassa, S. M., Cales, S., Moran, E. C., Myers, A. D., Richards, G. T., Eracleous, M., Heckman, T. M., Gallo, L., and Urry, C. (2014). The discovery of the first" changing look" quasar: New insights into the physics & phenomenology of agn. *arXiv preprint arXiv:1412.2136*.

Lumb, D. H., Schartel, N., and Jansen, F. A. (2012). Xmm-newton (x-ray mulit-mirror mission) observatory. *arXiv preprint arXiv:1202.1651*.

Luminari, A. (2024). Modelling of Black Hole Winds from the Horizon Up to Galaxy Scales.

Luminari, A., Nicastro, F., Elvis, M., Piconcelli, E., Tombesi, F., Zappacosta, L., and Fiore, F. (2021). Speed limits for radiation-driven smbh winds. *Astronomy & Astrophysics*, 646:A111.

Luminari, A., Piconcelli, E., Tombesi, F., Zappacosta, L., Fiore, F., Piro, L., and Vagnetti, F. (2018). Constraining the geometry of the nuclear wind in pds 456 using a novel emission model. *Astronomy & Astrophysics*, 619:A149.

Luminari, A., Tombesi, F., Piconcelli, E., Nicastro, F., Fukumura, K., Kazanas, D., Fiore, F., and Zappacosta, L. (2020). The importance of special relativistic effects in modelling ultra-fast outflows. *Astronomy & Astrophysics*, 633:A55.

Magorrian, J., Tremaine, S., Richstone, D., Bender, R., Bower, G., Dressler, A., Faber, S., Gebhardt, K., Green, R., Grillmair, C., et al. (1998). The demography of massive dark objects in galaxy centers. *The Astronomical Journal*, 115(6):2285.

Maraschi, L. and Haardt, F. (1997). Disk-corona models and x-ray emission from seyfert galaxies. In *International Astronomical Union Colloquium*, volume 163, pages 101–112. Cambridge University Press.

Marinucci, A., Bianchi, S., Braito, V., Matt, G., Nardini, E., and Reeves, J. (2018). Tracking the iron k α line and the ultra fast outflow in ngc 2992 at different accretion states. *Monthly Notices of the Royal Astronomical Society*, 478(4):5638–5649.

Marzi, M., Tombesi, F., Luminari, A., Fukumura, K., and Kazanas, D. (2023). Poynting-robertson effect on black-hole-driven winds. *Astronomy & Astrophysics*, 670:A122.

Mason, K., Breeveld, A., Much, R., Carter, M., Cordova, F., Cropper, M., Fordham, J., Huckle, H., Ho, C., Kawakami, H., et al. (2001). The xmm-newton optical/uv monitor telescope. *Astronomy & Astrophysics*, 365(1):L36–L44.

Mastichiadis, A. and Kirk, J. (1997). Variability in the synchrotron self-compton model of blazar emission. *Astronomy and Astrophysics, v. 320, p. 19-25*, 320:19–25.

Mathur, S., Fields, D., Peterson, B. M., and Grupe, D. (2012). Supermassive black holes, pseudobulges, and the narrow-line seyfert 1 galaxies. *The Astrophysical Journal*, 754(2):146.

Matt, G., Guainazzi, M., and Maiolino, R. (2003). Changing look: from compton-thick to compton-thin, or the rebirth of fossil active galactic nuclei. *Monthly Notices of the Royal Astronomical Society*, 342(2):422–426.

Menci, N., Cavaliere, A., Fontana, A., Giallongo, E., Poli, F., and Vittorini, V. (2003). Quasar evolution driven by galaxy encounters in hierarchical structures. *The Astrophysical Journal*, 587(2):L63.

Menci, N., Fiore, F., Feruglio, C., Lamastra, A., Shankar, F., Piconcelli, E., Giallongo, E., and Grazian, A. (2019). Outflows in the disks of active galaxies. *The Astrophysical Journal*, 877(2):74.

Mendoza, C., Bautista, M. A., Deprince, J., García, J. A., Gatuzz, E., Gorczyca, T. W., Kallman, T. R., Palmeri, P., Quinet, P., and Witthoeft, M. C. (2021). The xstar atomic database. *Atoms*, 9(1):12.

Merloni, A. and Fabian, A. (2001). Accretion disc coronae as magnetic reservoirs. *Monthly Notices of the Royal Astronomical Society*, 321(3):549–552.

Middleton, M. J., Walton, D. J., Fabian, A., Roberts, T. P., Heil, L., Pinto, C., Anderson, G., and Sutton, A. (2015). Diagnosing the accretion flow in ultraluminous x-ray sources using soft x-ray atomic features. *Monthly Notices of the Royal Astronomical Society*, 454(3):3134–3142.

Midooka, T., Mizumoto, M., and Ebisawa, K. (2023). Radiatively driven clumpy x-ray absorbers in the nls1 galaxy iras 13224-3809. *The Astrophysical Journal*, 954(1):47.

Miniutti, G. and Fabian, A. C. (2004). A light bending model for the x-ray temporal and spectral properties of accreting black holes. *Monthly Notices of the Royal Astronomical Society*, 349(4):1435–1448.

Mücke, A. and Protheroe, R. (2001). A proton synchrotron blazar model for flaring in markarian 501. *Astroparticle Physics*, 15(1):121–136.

Müller, A. (2004). *Black hole astrophysics: Magnetohydrodynamics on the Kerr geometry*. PhD thesis.

Murray, N., Quataert, E., and Thompson, T. A. (2005). On the maximum luminosity of galaxies and their central black holes: feedback from momentum-driven winds. *The Astrophysical Journal*, 618(2):569.

Nandra, K., Barret, D., Barcons, X., Fabian, A., Herder, J.-W. d., Piro, L., Watson, M., Adami, C., Aird, J., Afonso, J. M., et al. (2013). The hot and energetic

universe: A white paper presenting the science theme motivating the athena+ mission. *arXiv preprint arXiv:1306.2307*.

Narayan, R. and Yi, I. (1994). Advection-dominated accretion: A self-similar solution. *arXiv preprint astro-ph/9403052*.

Nardini, E., Reeves, J., Gofford, J., Harrison, F., Risaliti, G., Braito, V., Costa, M., Matzeu, G., Walton, D., Behar, E., et al. (2015). Black hole feedback in the luminous quasar pds 456. *Science*, 347(6224):860–863.

Nomura, M., Ohsuga, K., Takahashi, H. R., Wada, K., and Yoshida, T. (2016). Radiation hydrodynamic simulations of line-driven disk winds for ultra-fast outflows. *Publications of the Astronomical Society of Japan*, 68(1):16.

Ohsuga, K. and Mineshige, S. (2015). Outflow launching mechanisms. *The Physics of Accretion onto Black Holes*, pages 353–369.

Ohsuga, K., Mineshige, S., Mori, M., and Kato, Y. (2009). Global radiation-magnetohydrodynamic simulations of black-hole accretion flow and outflow: unified model of three states. *Publications of the Astronomical Society of Japan*, 61(3):L7–L11.

Osterbrock, D. E. and Pogge, R. W. (1985). The spectra of narrow-line seyfert 1 galaxies. *Astrophysical Journal, Part 1 (ISSN 0004-637X), vol. 297, Oct. 1, 1985, p. 166-176.*, 297:166–176.

Ostriker, E. C., McKee, C. F., and Klein, R. I. (1991). Isothermal, compton-heated coronae above accretion disks. *Astrophysical Journal, Part 1 (ISSN 0004-637X), vol. 377, Aug. 20, 1991, p. 593-611. Research supported by NASA.*, 377:593–611.

Parker, M., Matzeu, G., Matthews, J., Middleton, M., Dauser, T., Jiang, J., and Joyce, A. (2022). The x-ray disc/wind degeneracy in agn. *Monthly Notices of the Royal Astronomical Society*, 513(1):551–572.

Parker, M. L., Pinto, C., Fabian, A. C., Lohfink, A., Buisson, D. J., Alston, W. N., Kara, E., Cackett, E. M., Chiang, C.-Y., Dauser, T., et al. (2017). The response

of relativistic outflowing gas to the inner accretion disk of a black hole. *Nature*, 543(7643):83–86.

Peterson, B. M. (1997). *An introduction to active galactic nuclei*. Cambridge University Press.

Peterson, B. M. (2011). Masses of black holes in active galactic nuclei: Implications for nls1s. *arXiv preprint arXiv:1109.4181*.

Pezzulli, E., Valiante, R., and Schneider, R. (2016). Super-eddington growth of the first black holes. *Monthly Notices of the Royal Astronomical Society*, 458(3):3047–3059.

Pinto, C., Alston, W., Parker, M. L., Fabian, A. C., Gallo, L. C., Buisson, D. J., Walton, D. J., Kara, E., Jiang, J., Lohfink, A., et al. (2018). Ultrafast outflows disappear in high-radiation fields. *Monthly Notices of the Royal Astronomical Society*, 476(1):1021–1035.

Pinto, C., Mehdipour, M., Walton, D. J., Middleton, M. J., Roberts, T. P., Fabian, A. C., Guainazzi, M., Soria, R., Kosec, P., and Ness, J.-U. (2020). Thermal stability of winds driven by radiation pressure in super-eddington accretion discs. *Monthly Notices of the Royal Astronomical Society*, 491(4):5702–5716.

Pinto, C., Middleton, M. J., and Fabian, A. C. (2016). Resolved atomic lines reveal outflows in two ultraluminous x-ray sources. *Nature*, 533(7601):64–67.

Ponti, G., Gallo, L., Fabian, A. C., Miniutti, G., Zoghbi, A., Uttley, P., Ross, R., Vasudevan, R., Tanaka, Y., and Brandt, W. (2010). Relativistic disc reflection in the extreme nls1 iras13224- 3809. *Monthly Notices of the Royal Astronomical Society*, 406(4):2591–2604.

Ponti, G., Papadakis, I., Bianchi, S., Guainazzi, M., Matt, G., Uttley, P., and Bonilla, N. (2012). Caixa: a catalogue of agn in the xmm-newton archive-iii. excess variance analysis. *Astronomy & Astrophysics*, 542:A83.

Proga, D. and Kallman, T. R. (2002). On the role of the ultraviolet and x-ray radiation in driving a disk wind in x-ray binaries. *The Astrophysical Journal*, 565(1):455.

Proga, D. and Kallman, T. R. (2004). Dynamics of line-driven disk winds in active galactic nuclei. ii. effects of disk radiation. *The Astrophysical Journal*, 616(2):688.

Proga, D., Stone, J. M., and Kallman, T. R. (2000). Dynamics of line-driven disk winds in active galactic nuclei. *The Astrophysical Journal*, 543(2):686.

Reeves, J., Braito, V., Chartas, G., Hamann, F., Laha, S., and Nardini, E. (2020). Resolving the soft x-ray ultrafast outflow in pds 456. *The Astrophysical Journal*, 895(1):37.

Reynolds, C. (1997). An x-ray spectral study of 24 type 1 active galactic nuclei. *Monthly Notices of the Royal Astronomical Society*, 286(3):513–537.

Risaliti, G. and Elvis, M. (2004). A panchromatic view of agn. In *Supermassive Black Holes in the Distant Universe*, pages 187–224. Springer.

Rodriguez-Pascual, P. M., Mas-Hesse, J. M., and Santos-Lleo, M. (1997). The broad line region of narrow-line seyfert 1 galaxies. *arXiv preprint astro-ph/9706127*.

Ross, R. and Fabian, A. (2005). A comprehensive range of x-ray ionized-reflection models. *Monthly Notices of the Royal Astronomical Society*, 358(1):211–216.

Sanders, D. and Mirabel, I. (1996). Luminous infrared galaxies. *Annual Review of Astronomy and Astrophysics*, 34(1):749–792.

Schartel, N., González-Riestra, R., Kretschmar, P., Kirsch, M., Rodríguez-Pascual, P., Rosen, S., Santos-Lleó, M., Smith, M., Stuhlinger, M., and Verdugo-Rodrigo, E. (2024). Xmm-newton. In *Handbook of X-ray and Gamma-ray Astrophysics*, pages 1501–1538. Springer.

Schmidt, M. and Green, R. F. (1983). Quasar evolution derived from the palomar bright quasar survey and other complete quasar surveys. *Astrophysical Journal, Part 1 (ISSN 0004-637X), vol. 269, June 15, 1983, p. 352-374.*, 269:352–374.

Schmitt, H., Antonucci, R., Ulvestad, J., Kinney, A., Clarke, C., and Pringle, J. (2001). Testing the unified model with an infrared-selected sample of seyfert galaxies. *The Astrophysical Journal*, 555(2):663.

Schneider, P. (2006). *Extragalactic astronomy and cosmology: an introduction*, volume 146. Springer.

Shakura, N. and Sunyaev, R. (1973). Black holes in binary systems: Observational appearances. In *Symposium-International Astronomical Union*, volume 55, pages 155–164. Cambridge University Press.

Shu, X., Yaqoob, T., and Wang, J. (2010). The cores of the fe kα lines in active galactic nuclei: an extended chandra high energy grating sample. *The Astrophysical Journal Supplement Series*, 187(2):581.

Sikora, M., Stawarz, Ł., Moderski, R., Nalewajko, K., and Madejski, G. M. (2009). Constraining emission models of luminous blazar sources. *The Astrophysical Journal*, 704(1):38.

Silk, J. and Rees, M. J. (1998). Quasars and galaxy formation. *arXiv preprint astro-ph/9801013*.

Soldi, S., Türler, M., Paltani, S., Aller, H., Aller, M., Burki, G., Chernyakova, M., Lähteenmäki, A., McHardy, I., Robson, E., et al. (2008). The multiwavelength variability of 3c 273. *Astronomy & Astrophysics*, 486(2):411–425.

Soltan, A. (1982). Masses of quasars. , 200:115–122.

Strüder, L., Briel, U., Dennerl, K., Hartmann, R., Kendziorra, E., Meidinger, N., Pfeffermann, E., Reppin, C., Aschenbach, B., Bornemann, W., et al. (2001). The european photon imaging camera on xmm-newton: the pn-ccd camera. *Astronomy & Astrophysics*, 365(1):L18–L26.

Tadhunter, C. (2008). An introduction to active galactic nuclei: Classification and unification. *New Astronomy Reviews*, 52(6):227–239.

Tadhunter, C., Morganti, R., Robinson, A., Dickson, R., Villar-Martin, M., and Fosbury, R. (1998). The nature of the optical-radio correlations for powerful radio galaxies. *Monthly Notices of the Royal Astronomical Society*, 298(4):1035–1047.

Tanaka, Y., Nandra, K., Fabian, A., Inoue, H., Otani, C., Dotani, T., Hayashida, K., Iwasawa, K., Kii, T., Kunieda, H., et al. (1995). Gravitationally redshifted emission implying an accretion disk and massive black hole in the active galaxy mcg–6–30–15. *Nature*, 375(6533):659–661.

Tarter, C. B., Tucker, W. H., and Salpeter, E. E. (1969). The interaction of x-ray sources with optically thin environments. *Astrophysical Journal, vol. 156, p. 943*, 156:943.

Team, X. S. et al. (2020). Science with the x-ray imaging and spectroscopy mission (xrism). *arXiv preprint arXiv:2003.04962*.

Toba, Y., Oyabu, S., Matsuhara, H., Malkan, M. A., Gandhi, P., Nakagawa, T., Isobe, N., Shirahata, M., Oi, N., Ohyama, Y., et al. (2014). Luminosity and redshift dependence of the covering factor of agns viewed with wise and sdss. *arXiv preprint arXiv:1404.4937*.

Tomaru, R., Done, C., Odaka, H., Watanabe, S., and Takahashi, T. (2018). Monte carlo simulations of the detailed iron absorption line profiles from thermal winds in x-ray binaries. *Monthly Notices of the Royal Astronomical Society*, 476(2):1776–1784.

Tombesi, F., Cappi, M., Reeves, J., Nemmen, R. S., Braito, V., Gaspari, M., and Reynolds, C. S. (2013). Unification of x-ray winds in seyfert galaxies: from ultra-fast outflows to warm absorbers. *Monthly Notices of the Royal Astronomical Society*, 430(2):1102–1117.

Tombesi, F., Cappi, M., Reeves, J., Palumbo, G., Braito, V., and Dadina, M. (2011). Evidence for ultra-fast outflows in radio-quiet active galactic nuclei. ii. detailed photoionization modeling of fe k-shell absorption lines. *The Astrophysical Journal*, 742(1):44.

Tombesi, F., Cappi, M., Reeves, J., Palumbo, G., Yaqoob, T., Braito, V., and Dadina, M. (2010). Evidence for ultra-fast outflows in radio-quiet agns-i. detection and statistical incidence of fe k-shell absorption lines. *Astronomy & Astrophysics*, 521:A57.

Tombesi, F., Meléndez, M., Veilleux, S., Reeves, J., González-Alfonso, E., and Reynolds, C. (2015). Wind from the black-hole accretion disk driving a molecular outflow in an active galaxy. *Nature*, 519(7544):436–438.

Turner, M. J., Abbey, A., Arnaud, M., Balasini, M., Barbera, M., Belsole, E., Bennie, P., Bernard, J., Bignami, G., Boer, M., et al. (2001). The european photon imaging camera on xmm-newton: the mos cameras. *Astronomy & Astrophysics*, 365(1):L27–L35.

Uchida, Y. and Shibata, K. (1985). Magnetodynamical acceleration of co and optical bipolar flows from the region of star formation. *Astronomical Society of Japan, Publications (ISSN 0004-6264), vol. 37, no. 3, 1985, p. 515-535. Sponsorship: Ministry of Education, Science, and Culture of Japan.*, 37:515–535.

Urry, C. M. and Padovani, P. (1995). Unified schemes for radio-loud active galactic nuclei. *Publications of the Astronomical Society of the Pacific*, 107(715):803.

Vietri, G., Mainieri, V., Kakkad, D., Netzer, H., Perna, M., Circosta, C., Harrison, C., Zappacosta, L., Husemann, B., Padovani, P., et al. (2020). Super-iii. broad line region properties of agns at z 2. *Astronomy & Astrophysics*, 644:A175.

Vietri, G., Piconcelli, E., Bischetti, M., Duras, F., Martocchia, S., Bongiorno, A., Marconi, A., Zappacosta, L., Bisogni, S., Bruni, G., et al. (2018). The wissh quasars project iv. blr versus kpc-scale winds. *arXiv preprint arXiv:1802.03423*.

Walton, D., Middleton, M., Pinto, C., Fabian, A., Bachetti, M., Barret, D., Brightman, M., Fuerst, F., Harrison, F., Miller, J., et al. (2016). An iron k component to the ultrafast outflow in ngc 1313 x-1. *The Astrophysical Journal Letters*, 826(2):L26.

Wilkins, D., Cackett, E., Fabian, A., and Reynolds, C. (2016). Towards modelling x-ray reverberation in agn: piecing together the extended corona. *Monthly Notices of the Royal Astronomical Society*, 458(1):200–225.

Wilkins, D. and Fabian, A. (2012). Understanding x-ray reflection emissivity profiles in agn: locating the x-ray source. *Monthly Notices of the Royal Astronomical Society*, 424(2):1284–1296.

Woods, D. T., Klein, R. I., Castor, J. I., McKee, C. F., and Bell, J. B. (1996). X-ray–heated coronae and winds from accretion disks: Time-dependent two-dimensional hydrodynamics with adaptive mesh refinement. *Astrophysical Journal v. 461, p. 767*, 461:767.

Yamasaki, H., Mizumoto, M., Ebisawa, K., and Sameshima, H. (2016). Origin of the characteristic x-ray spectral variations of iras 13224- 3809. *Publications of the Astronomical Society of Japan*, 68(5):80.

Young, A., Crawford, C., Fabian, A., Brandt, W., and O'Brien, P. (1999). The optical variability of the narrow-line seyfert 1 galaxy iras 13224—3809. *Monthly Notices of the Royal Astronomical Society*, 304(4):L46–L52.

Zhou, X.-L. and Wang, J.-M. (2004). Narrow iron kα lines in active galactic nuclei: Evolving populations? *The Astrophysical Journal*, 618(2):L83.

Zubovas, K. and King, A. (2012). Agn winds and the black-hole-galaxy connection. *arXiv preprint arXiv:1201.3540*.

Appendix A

Statistics Supplements

A.1 Chi-Square Test

XSPEC[1] performs two operations: best-fit parameter estimation and testing if the model and these parameters match the data. Statistics is therefore required to measure the goodness-of-fit. There are different types of statistical tests. It depends on the probability distribution of the underlying data to determine which type of statistical tests should be used. Users can specify the statistic of their choice by using the `statistic` command.

Most of the astronomical data are drawn from one of the two distributions: Gaussian (or normal) and Poisson. The Poisson distribution is commonly used in counting statistics when the only source of experimental noise is due to the number of events arriving at the detector, making it a good approximation for modern CCD instruments. However, if other types of noise dominate, like uncertainties in background modelling, then it is usually described by the Gaussian distribution. In such a case, the background noise requires to be modeled in some way, instead of being directly measured. The associated uncertainty is then assumed to follow a Gaussian distribution.

When dealing with large numbers of counts, the Poisson distribution can be well

[1]This section has been adapted from XSPEC Manual.

approximated by a Gaussian. Therefore, Gaussian distribution is often used for detectors with high counting rates. In most cases this does not introduce any errors and also simplifies the handling of background uncertainties. However, care should be taken to ensure that no systematic offsets are introduced.

A.1.1 Parameter Estimation

The method of maximum likelihood is commonly used in parameter estimation. It is based on the idea that the best values of the parameters are those that maximize the probability of the observed data given the model. The likelihood function represents the total probability of the observed data given the model, and the current model parameters. In practice, the statistic employed is twice the negative logarithm of the likelihood.

The likelihood for Gaussian data is:

$$L = \prod_{i=1}^{N} \frac{1}{\sigma_i \sqrt{2\pi}} \; exp\left[\frac{-(y_i - m_i)^2}{2\sigma_i^2}\right] \tag{A.1}$$

where y_i are the observed data rates, σ_i their errors, and m_i the values of the predicted data rates based on the model (with current parameters) and instrumental response. Taking twice the negative natural log of L and ignoring terms which depend only on the data gives the statistic:

$$S^2 = \sum_{i=1}^{N} \frac{(y_i - m_i)^2}{\sigma_i^2} \tag{A.2}$$

which is commonly referred to as chi-squared χ^2 statistic. The probability density function (PDF) of the chi-squared distribution (Fig. A.1) is given by:

$$f(x;k) = \begin{cases} \frac{x^{\frac{k}{2}-1} e^{-\frac{x}{2}}}{2^{\frac{k}{2}} \Gamma\left(\frac{k}{2}\right)}, & \text{if } x > 0; \\ 0, & \text{otherwise.} \end{cases} \tag{A.3}$$

where k is the degrees of freedom and $\Gamma(k/2)$ denotes the gamma function. It is

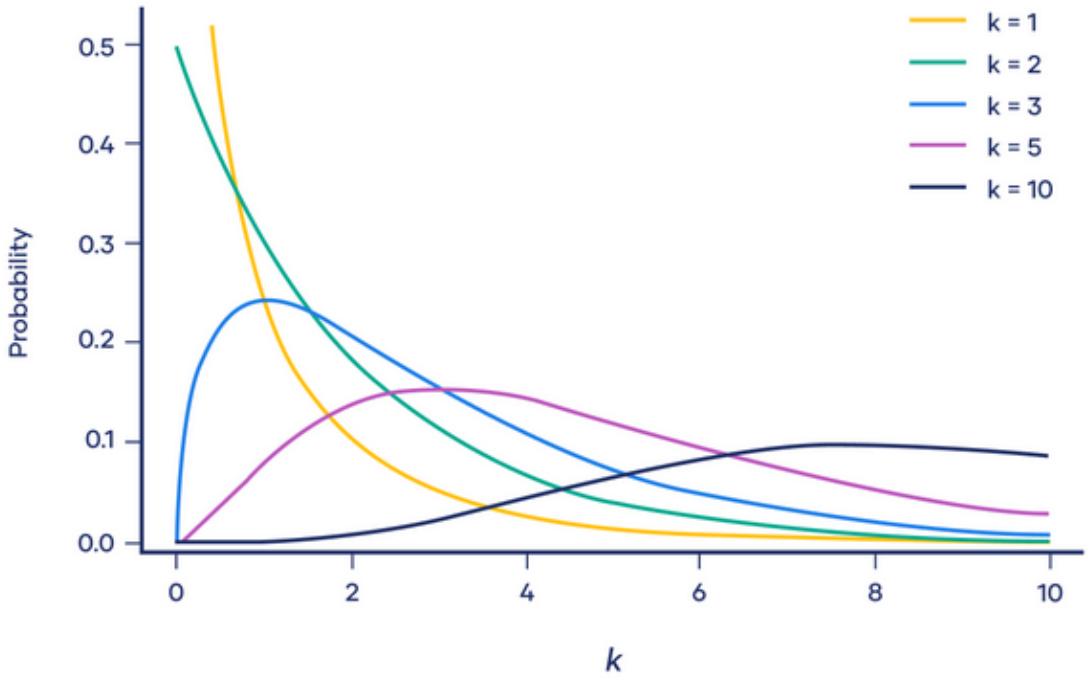

Figure A.1: Plot of the chi-square distribution for different values of k.

widely used in hypothesis testing, construction of confidence intervals and the common chi-squared tests for goodness of fit of an observed distribution to a theoretical one.

A.1.2 Parameter confidence regions

XSPEC offers several methods to estimate the precision of parameter determination. One of the most reliable method for deriving parameter confidence regions is identifying surfaces of constant delta statistic from the best-fit value, i.e. where :

$$\text{Statistic} = \text{Statistic}_{\text{best-fit}} + \Delta \tag{A.4}$$

where Δ is from the Table A.1. This is the approach used by the `error` command. It searches for the parameter value where the statistic deviates from the best fit by the Δ value specified in the command. The other free parameters are allowed to vary when each value of a particular parameter is being tested. Simultaneous confidence regions of multiple parameters can also be found using `steppar` command. The

Significance	Number of parameters		
α	1	2	3
0.68	1.00	2.30	3.50
0.90	2.71	4.61	6.25
0.99	6.63	9.21	11.30

Table A.1: Chi-square differences Δ above minimum.

specific values of Δ corresponding to particular confidence regions are calculated by assuming a chi-squared distribution with the number of degrees of freedom being equal to the number of parameters that are tested. This assumption holds for the χ^2 statistic and is asymptotically correct for other statistics.

A.1.3 Goodness-of-fit

The standard way of checking if the model actually fits the data involves performing a test to reject the null hypothesis that the observed data are drawn from the model. A test statistic T is calculated, and if the observed statistic T_{obs} exceeds a critical threshold $T_{critical}$, the model is rejected at the confidence level corresponding to $T_{critical}$. For chi squared, the value of $T_{critical}$ is independent of the model and therefore widely used. For other test statistics, the distribution of T needs be estimated for the model in use and then compared with the observed value. If T_{obs} exceeds 90% of these simulated T values, the model can be rejected at 90% confidence. The goodness-of-fit test only rejects a model with a certain level of confidence, it does not give the probability for the correctness of the model.

Chi-squared is the standard goodness-of-fit test for Gaussian data. The significance of the chi-squared values depend on the number of degrees of freedom (dof), which is calculated as the number of data bins minus the number of free param-

eters. Xspec reports the null hypothesis probability, which is the probability that the observed data is drawn from the model given the value of chi-squared and the dof. A rule of thumb is that $\chi^2 \approx$ dof. $\chi^2 >>$ dof means the observed data are not likely drawn from the model and $\chi^2 <<$ dof means the Gaussian sigma associated with the data are most likely over-estimated.

A.2 F-Test

The F-test is a statistical tool that is used to compare the variances of two samples or the ratio of variances between multiple samples to determine if they differ significantly. It uses the F-distribution (also known as the Fisher–Snedecor distribution) to test a hypothesis. The method involves calculating a test statistic, denoted as F, which is used to determine whether the tested data follows an F-distribution under the null hypothesis. This test is widely used in comparing statistical models fitted to a data set and identifying the model that best fits the population from which the data were sampled. The test follows three assumptions:

- each datum is considered to be independent from another,
- data are Gaussian, i.e., uncertainties on data are normally distributed,
- homogeneity of variance, i.e., all data have same finite variance.

The F-test statistic is calculated as the ratio of two scaled sums of squares representing different sources of variability. These sums of squares are designed to increase the test statistic when the null hypothesis is not true. A statistic will follow the F-distribution under the null hypothesis when the sums of squares are statistically independent, and each follows a scaled χ^2-distribution. Given two variables, χ_1^2 and χ_2^2, that follow the χ^2-distribution with ν_1 and ν_2 degrees of freedom respectively, we can define the F-test statistic as:

$$f = \frac{\chi_1^2/\nu_1}{\chi_2^2/\nu_2} \tag{A.5}$$

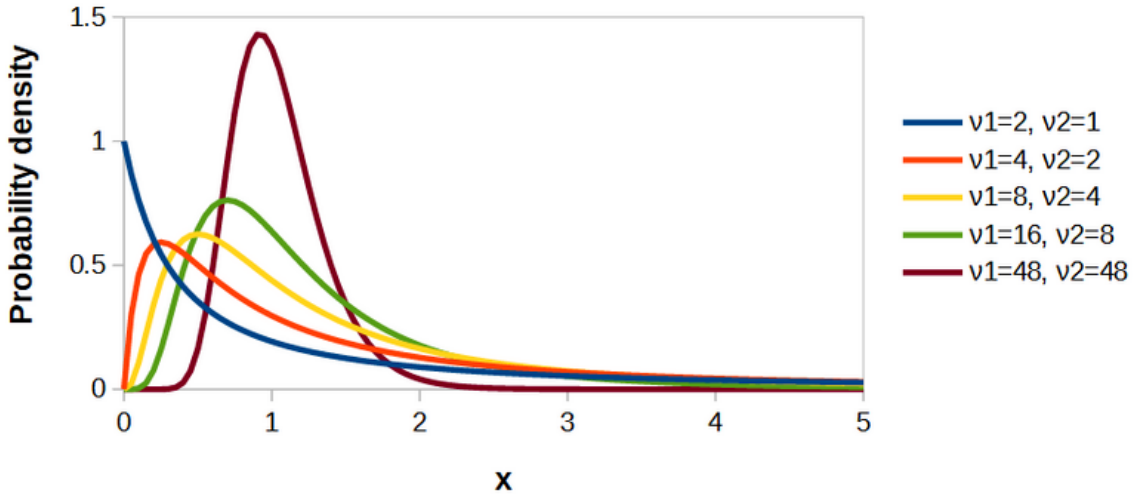

Figure A.2: Probability density function plots for five sample F-distributions where x is the value of F-test statistic.

which follows the F-distribution whose PDF (Fig. A.2) is given as:

$$p(f;\nu_1,\nu_2) = \frac{1}{B\left(\frac{\nu_1}{2},\frac{\nu_2}{2}\right)}\left(\frac{\nu_1}{\nu_2}\right)^{\frac{\nu_1}{2}} f^{\frac{\nu_1}{2}-1}\left(1+\frac{\nu_1}{\nu_2}f\right)^{-\frac{\nu_1+\nu_2}{2}} \tag{A.6}$$

where f, ν_1, $\nu_2 > 0$ and $B\left(\frac{\nu_1}{2},\frac{\nu_2}{2}\right)$ is the Beta function.

To check if two models significantly differ in fitting the same dataset, we can compute the probability by integrating the PDF.

$$P_f(f^0;\nu_1,\nu_2) = \int_{f_0}^{\infty} p(f;\nu_1,\nu_2)\, df \tag{A.7}$$

where f_0 is the particular value obtained for f and χ_1^2 and χ_2^2 are the statistical values for the two models. If this value of P_f is below the chosen confidence level, then the goodness of the two fits are significantly different.

If we have to decide whether a secondary nested model is statistically significant than the initial model, the Partial F-test is used. It is a modified version of the Fischer test and is used to evaluate if there is a statistically significant difference between a regression model and the nested version of the same model. A nested model is one that contains a subset of the predictor variables in the overall regres-

sion model. To determine the significant contribution of the excluded variables to the model, the difference in the sum of squares between the full and reduced models is calculated. This difference corresponds to the sum of squares attributed to the excluded variables. Next, this extra sum of squares is compared to the residual sum of squares of the reduced model to obtain an F-statistic. The degrees of freedom of this statistic is equal to the difference in the number of parameters between the full and reduced models.

In practice, we use the theory developed for two models:

$$\chi^2_1, \text{ d.o.f.}_1 \rightarrow (\chi^2_1 - \chi^2_2), \text{ (d.o.f.}_1 \text{ - d.o.f.}_2) \ .$$

The F-test statistic is calculated as:

$$f = \frac{\chi^2_{nest} - \chi^2_{full}}{\Delta\nu} \Big/ \frac{\chi^2_{full}}{N - p} \ \equiv \ \frac{\chi^2_{nest} - \chi^2_{full}}{d.o.f._{nest} - d.o.f._{full}} \Big/ \frac{\chi^2_{full}}{d.o.f._{full}} \tag{A.8}$$

where, χ^2_{nest} is the statistics of the nested model, χ^2_{full} is the statistics of the full model, $\Delta\nu = (\text{d.o.f.}_1 \text{ - d.o.f.}_2)$, N is the sample size and p is the number of parameters of the full model. The corresponding P-value is calculated as:

$$P = 1 - p(f; \Delta\nu, d.o.f._2) \tag{A.9}$$

This gives the probability that the extra component is random and (1 - P) gives the significance of the extra component. To transform the P-value into a sigma confidence interval, we use the quantile function of the normal distribution.

Acknowledgements

A thesis is not only the result of an individual's efforts but also involves invaluable support, guidance, and encouragement from people who are a part of the academic journey.

First and foremost, I would like to thank both my supervisors, Prof. Francesco Tombesi from University of Rome Tor Vergata and Prof. Luka Č. Popović from University of Belgrade, whose guidance, suggestions, insightful feedback, and unwavering support have been instrumental in shaping my challenging yet fulfilling journey. Their mentorship has shaped my understanding of astrophysics and their encouragement has fueled my perseverance. I also owe immense thanks to Dr. Marco Laurenti and Pierpaolo Condò, who patiently guided and encouraged me throughout my work. They always answered all my doubts and curiosities. Their critique and advice helped me to improve my thesis. I would also like to thank Dr. Alfredo Luminari for providing us with the WINE table models that we used in our analysis.

I would like to thank the people from all four consortium universities, both academic and non-academic, who worked hard to provide us with this wonderful opportunity and make this program a successful one. Their invaluable assistance ensured that the transitions between universities were smooth and manageable. Apart from the educational enrichment, I am also grateful towards this program and people for providing me with a taste of the cultural diversities across Europe. These experiences have helped me to evolve as a person and be more considerate towards other people. I sincerely thank the MASS Project Office, specially Dr. Adalia Caroli and Dr. Giovanna Temporin from University of Rome Tor Vergata, for helping us in

dealing with all the administrative works and making our lives easier.

To all my friends from the first edition of MASS, I am deeply grateful for the friendships we made here. From sharing jokes to academic ideas, your collaborative spirit has made this journey more memorable. I thank Sagarika, whose friendship has been the most valuable thing in these two years away from home. Your patience and understanding has kept me sane during the most stressful times. Our study sessions and random discussions on different aspects of Astrophysics has enhanced my curiosity and helped me to get a better grasp on the subject. Thank you for always being there when I needed it the most.

To my beautiful family, no words can truly express the depth of my gratitude. My parents, who are my pillars of strength and support, I thank you for always believing in my dreams. Your constant faith in me has encouraged me to bring out the best version of myself. You sacrificed your dreams so that I could live mine. None of these would have been possible without your unconditional love. To my sister, who has been equal parts annoying and loving, thank you for always encouraging me while I ventured on this journey. Your humor and love made me feel alive even in the bleakest of days.

To all those who walked beside me on this journey, thank you.

Sreeparna Ganguly acknowledges support through an "Erasmus Mundus Joint Master (EMJM)" Fee Waiver funded by the European Union in the framework of the Erasmus+, Erasmus Mundus Joint Master in Astrophysics and Space Science – MASS. Views and opinions expressed are however those of the author(s) only and do not necessarily reflect those of the European Union or the granting authority European Education and Culture Executive Agency (EACEA). Neither the European Union nor the granting authority can be held responsible for them.